Thermal Stretching of GEM Foils and Characterization of Triple-GEM Detectors for Uses in Astronomy

by

Bryant Joseph Benson

Bachelors Degree in Space Sciences
Florida Institute of Technology, 2008

A thesis
submitted to
Florida Institute of Technology
in partial fulfillment of the requirements
for the degree of

Master of Science
In Space Sciences

Melbourne, Florida
May, 2011

We the undersigned committee hereby recommend
that the attached document be accepted as fulfilling in
part the requirements for the degree of
Master of Science in Space Sciences.

"Thermal Stretching of GEM Foils and Characterization of Triple-GEM Detectors for Uses in Astronomy," a thesis by Bryant Joseph Benson

Marcus Hohlmann, Ph.D. Associate Professor Physics and Space Sciences	Debasis Mitra, Ph.D. Professor Computer Sciences
Joseph Dwyer, Ph.D. Professor Physics and Space Sciences	Terry D. Oswalt, Ph.D. Professor and Head Physics and Space Sciences

Abstract

Title: Thermal Stretching of GEM Foils and Characterization of Triple-GEM Detectors for Uses in Astronomy.

Author: Bryant Joseph Benson

Advisor: Dr. Marcus Hohlmann

A new technique for the thermal stretching of GEM foils using an infrared light rack and acrylic stretching frames is presented and discussed. Stretching of GEM foils is currently one of the cost and size limiting factor in the production of GEM detectors. This new stretching technique aims to severely reduce both of these factors by using inexpensive and easily available materials to construct a compact stretching apparatus which can be easily disassembled for storage to save space when not in use. We also discuss the feasibility in adapting GEM detectors to be used in astronomical observations. The uses of GEM detectors in the High Energy Physics field have been proven, but they have yet to be utilized in Astronomy, especially for the detection of X-rays. We constructed and heavily tested two 30 cm 30 cm GEM triple GEM detectors for their Gain uniformity and energy sensitivities. Coded aperture mask techniques for X-ray imaging in particular are well suited for use with the position-sensitive GEM detectors. Computer simulations for a number of sources were run to analyze the capabilities of a GEM detector used with a coded aperture mask. The high position resolution, as well as the specific energy range to which the GEM detector is sensitive (1 keV to ~15 keV) make it a promising position-sensitive detector to be used in this form of astronomical observation.

Table of Contents

List of Figures and Tables

Acknowledgments

I would first like to thank Dr. Hohlmann for all the advice and guidance he has given me in this research project. I am very grateful that he gave me a position on his research team and provided me with a very educational research opportunity by introducing me to the hardware side of physics research. I have learned a great deal under his guidance and he has been an excellent advisor. I wish I could have gotten involved in this project earlier.

Next I would like to thank Michael Staib, my fellow graduate student, with whom I have worked on the many challenges in this research project. Together we were able to develop, fabricate, and solve the issues of the infrared stretching process, as well as construct the two triple-GEM detectors we have used in our characterization measurements.

Amilkar Quintero was a fellow graduate student who graduated in the summer of 2010 and was a big help in teaching me and Mike how to construct the GEM detectors after we stretched the foils. In the summer, while we were working in the lab together he taught me everything he used in his research on the construction and use of GEM detectors.

Thank you to all of the members of the HEP lab A who assisted in the work done on the GEM detector project. To post doc Kondo-Gnavo for his input and expertise from his previous research experience on GEM detectors. To undergraduates Alfred, Greg, and especially Mike for their assistance in the measurements we took and in analyzing the data in our characterization tests.

Lastly I would like to thank the Department of Homeland Security for the funding they provided to the Muon Tomography research, which is what the GEM detectors we built and are working with are going to be used for.

I want to dedicate my thesis work to my family and friends, especially to my girlfriend Helen. They have been very supportive of me in my education and endeavors.

Chapter 1 Introduction

1.1 Charged Particle Interaction With a Gas

There are several ways for a charged particle moving at a high velocity to interact with the medium through which it is passing. In the case of gaseous detectors, only one of these is really of any concern. The electromagnetic interaction through Coulomb forces between a fast moving charged particle and a gaseous medium is much more likely to occur than any of the other interactions. Strong and weak force interactions can be entirely ignored, as they are extremely unlikely to occur in the detector or produce a measureable signal from the charged particle's passage. Other electromagnetic forces such as Bremsstrahlung, Cherenkov and transition radiation can also be ignored as they are also extremely unlikely to produce any measureable signal [1].

The signal produced through the Coulomb interaction between a fast moving charged particle and the gaseous medium through which it is travelling is in the form of ionized atoms and electrons. When the charged particle passes through the medium its electromagnetic field interacts with the electromagnetic fields of the gas molecules. This interaction transfers enough energy from the charged particle to the atoms in the gas to excite and ionize some of the atoms

Because the interaction is on the atomic scale, there is no precise way to quantify the exact amount of energy transferred between an individual charged particle and the medium through which it is travelling. As with most interaction on the quantum scale, the most effective treatment is to approximate the average

energy imparted over a finite distance. To do this we use the Bethe-Bloch equation [2].

Where:- — is the amount of energy imparted from the charged particle to the medium over a differential distance.

- K is a constant given by the combination of other constants in the equation
- is Avogadro's number
- e is the charge of an electron
- is the permittivity of free space
- is the mass of an electron
- c is the speed of light
- z is the charge of the particle travelling through the medium
- β is the velocity of the charged particle as a fraction of the speed of light (v/c)
- Z is the atomic number of the medium
- A is the atomic mass of the medium
- γ is the Lorentz factor of the charged particle
- is the maximum amount of kinetic energy than can be imparted from the charged particle to a free electron per collision
- I is the ionization potential of the medium

- $\delta(\beta\gamma)$ is the density effect correction for the medium

The Bethe-Bloch formula only has two variables dependent upon the charged particle. Those are the charge of the particle, z, and its velocity as a fraction of the speed of light, β. The charge of the particle is much less important than the particle velocity, as it will almost always simply be a small integer multiple of the charge of an electron. With this in mind it becomes apparent that the Bethe-Bloch equation is dominated by the term, starting with a very fast decrease as the velocity increases. At around $\beta = 0.97$, the energy loss reaches a nearly constant value before beginning a slow increase as β approaches one, which can be seen for multiple charged particles in figure 1.1. The slight rise in energy loss per unit length is due to relativistic effects as the charged particle approaches the speed of light. This region is referred to as the minimum ionization region, and it corresponds to the minimum energy a particle loses in its interactions to the medium it is passing through regardless of how much faster it may be moving [3].

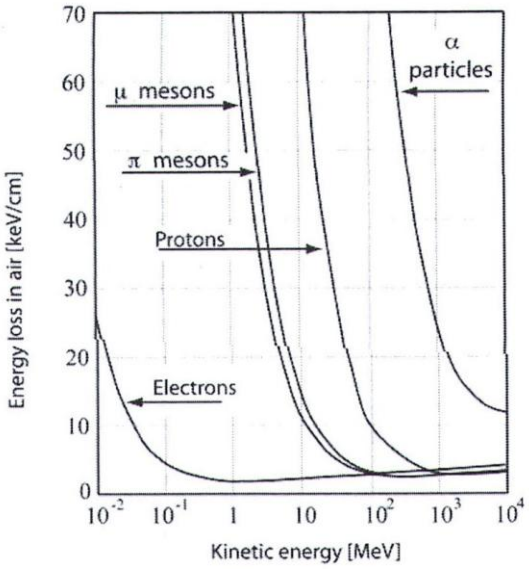

Figure 1.1: Plot of Energy Loss per unit Length vs. Initial Kinetic Energy for different high energy charged particles in air [3].

The energy loss mechanism between a fast moving charged particle and the medium it is travelling through is statistical in nature, meaning the amount of energy deposited by particles with equal amounts of initial kinetic energy will not always be the same. They will instead fit to a statistical distribution. This particular mechanism can be fit to an asymmetric curve referred to as a Landau distribution, which can be expressed as follows [4].

Where:- f(λ) is the energy loss as a function of λ

- is the most probable energy loss per interaction
- is the actual energy loss in an interaction
- ξ is the average energy loss given by the first term in the Bethe-Bloch equation
- λ is the normalized deviation from the most probable energy loss
- K, Z, A, and β are the same variables as used in the Bethe-Bloch equation

For more information on the origin of the Landau distribution please see Appendix A.

Following the laws of conservation, any amount of energy gained by the medium in the ionization of its atoms must be taken from the charged particle. Because the particle in question is not losing any of its charge, this energy must come from the charged particles kinetic energy. Due to its interactions with the medium it is travelling through, a fast moving charged particle slows down and

would eventually come to a stop given enough distance. It has already been stated that a slower moving particle loses more energy per distance travelled than a fast moving particle, telling us that a plot of the energy lost versus the distance travelled must be exponential up to the point where the charged particle has lost all of its kinetic energy, referred to as the Bragg peak, after which its kinetic energy will suddenly drop off to zero [3]. This process can be clearly seen in figure 1.2, starting with the slow rise in energy loss per distance, then ending in the sharp Bragg peak.

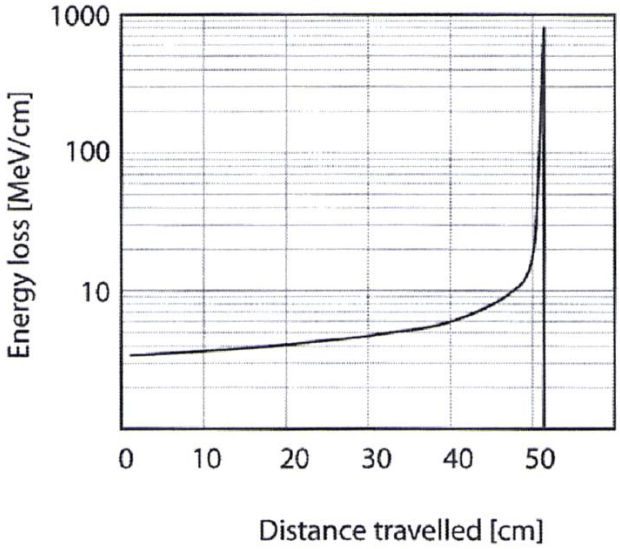

Figure 1.2: Energy loss per unit length vs. distance travelled for a proton travelling through water, showing the characteristic Bragg peak where the charged particle loses the last of its kinetic energy [3].

The distance a charged particle travels through a medium before it has lost all of its kinetic energy is called its range. Because the energy loss procedure is statistical in nature there exists what is referred to as range straggling. Range

straggling is the amount of fluctuation allowed in the range for particles carrying the same amount of kinetic energy [3].

In the development of a GEM detector the range of the particles you wish to measure must be taken into account. In the case of the GEM detectors we are working with, which are primarily designed to track the path muons, the thickness of the detector is kept to a relatively minimum size. This minimum size, combined with a stack of multiple GEM detectors, allows for the muons to pass through with a small loss of energy. This is important because too much energy loss may also alter the path of the muon. If we had been more interested in the energy of the particles measured rather than the path they travel, a thicker GEM detector would be a better option. Larger distances in the ionization zone and between the GEM foils would allow for more energy from the particles to be deposited. This would correspond to a higher sensitivity to the energy of the charged particle while leaving us with lower position sensitivity.

1.2 Photon Absorption in a Medium

The detection of photons is similar to the detection of charged particles in that it takes a form of electromagnetic interaction inside the chamber to ionize electrons. This is the only similarity between the two types of detection however. In the case of detecting photons the interaction takes place in the form of a single absorption event rather than multiple electromagnetic interactions along the path. The probability of absorption can be expressed via a function of the cross section of interaction, the mass attenuation coefficient, or the mean free path of the photon. These three different characteristics can each be used for our probability function because they can each be written as a function of the others. Starting with the cross section of interaction, the photon intensity takes the form [3]:

Where: - is the intensity of the photon beam at x

- σ is the cross section of interaction
- N is the number of molecules per unit volume
- X is the thickness of the medium traversed by the photon beam

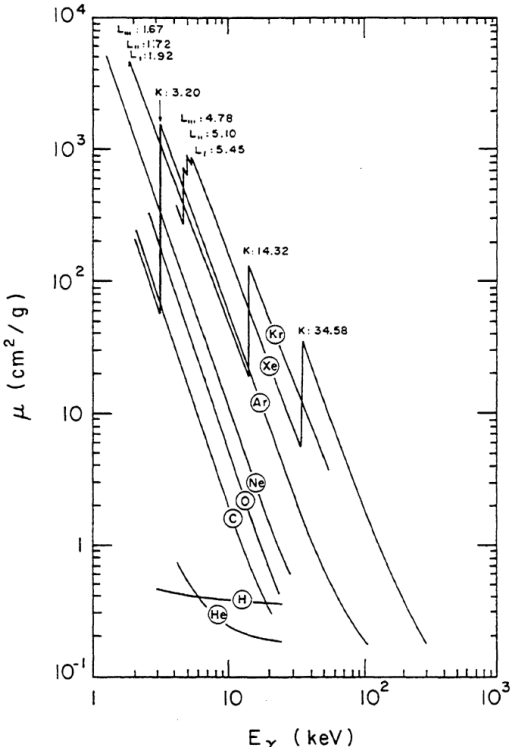

Figure 1.3: Mass attenuation vs. photon energy for several gasses typically used in gaseous detectors [1].

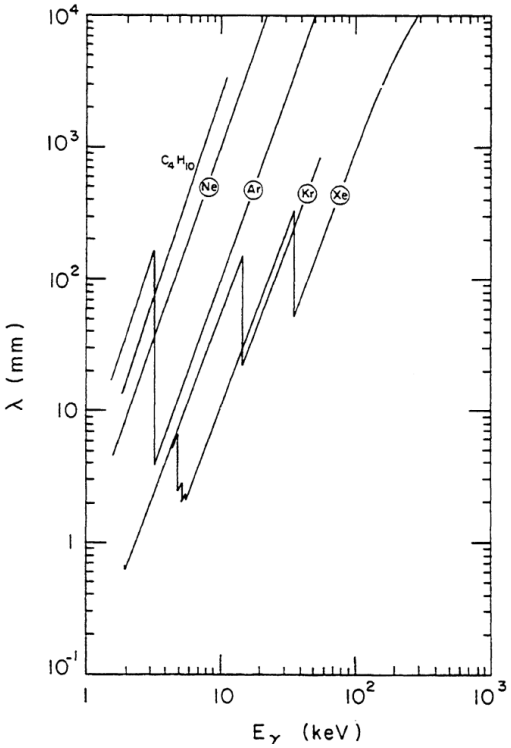

Figure 1.4: Mean free path vs. photon energy for several gasses typically used in gaseous detectors [1].

Converting this into a function of the mass attenuation coefficient (μ) is simply a matter of rearranging the units in the exponential. While the cross section only has units of area (, the mass attenuation coefficient has an added unit of

one over mass (. To counteract this difference in units we have to take the mass density (ρ) of the medium rather than the number density into the exponential, giving us a function of the form [1]:

The second form of the function using the mass attenuation coefficient includes the reduced thickness of the medium traversed ($x = \rho X$). The last form for this equation is also the one that gives the most useful information for the design of a detector meant to detect photons. The mean free path (λ) of a photon is the average distance a photon of specific energy will travel through a medium until it interacts via absorption. Because this absorption interaction is how we obtain the ionized electrons in the GEM detector, this mean free path gives us the minimum thickness we want for our ionization zone. If the ionization zone of the detector is less than the mean free path of the photons we wish to detect, then the efficiency of the detector will be less than optimum for the job. Plots of the mass attenuation coefficient and the mean free path of photons versus the photon energy for several gasses typically used in GEM detectors are shown in figures 1.3 and 1.4 respectively. The mean free path is defined as a function of the mass attenuation coefficient and the medium density (, which changes the form of our function to [1]:

There are several different types of interactions that can occur between photons and the medium in the ionization zone of the GEM detector and the type of interaction that occurs is primarily dependent upon the photon energy. For lower energies, in the range of keV, photoelectric conversion dominates. As this energy

increases we start to see more Compton scattering inside the detector. At still higher energies the interaction changes to electron-positron pair production [3]. For X-ray astronomy we are much more interested in the lower energy range of these interactions via the photoelectric conversion because we can obtain much more information with a GEM detector.

X-Rays are important to consider for GEM detectors not only because of the possible uses as a new detector in X-Ray astronomy, but also because many labs will use an X-Ray source with a known energy in the low keV range to test the gain and uniformity of their detectors in production. Photoelectric conversion works essentially in the way it sounds. The incident photon of energy is absorbed by the atom it interacts with, which converts the energy of the photon to kinetic energy. If is greater than the binding energy of an electron in the atom, that electron is removed from its parent atom, resulting in a primary electron. This primary electron usually originates from the inner K-shell of atom, as it has the highest binding energy.

The now ionized atom must return to its ground state through one of two processes. The first process is through the emission of new, lower energy photon from the transition of an electron in a higher shell into the now vacant state. The photon can have a very long mean free path and can escape the detector, and thus detection. This leads to a less accurate measurement of the energy of the incident photon which becomes evident as a secondary peak, referred to as the escape peak, when the mean energies detected are binned plotted in a histogram [1]. The new photon can still be reabsorbed by another atom and result in the ionization of a lower energy secondary electron, as shown in figure 1.5, which will not result in any energy loss in the detection.

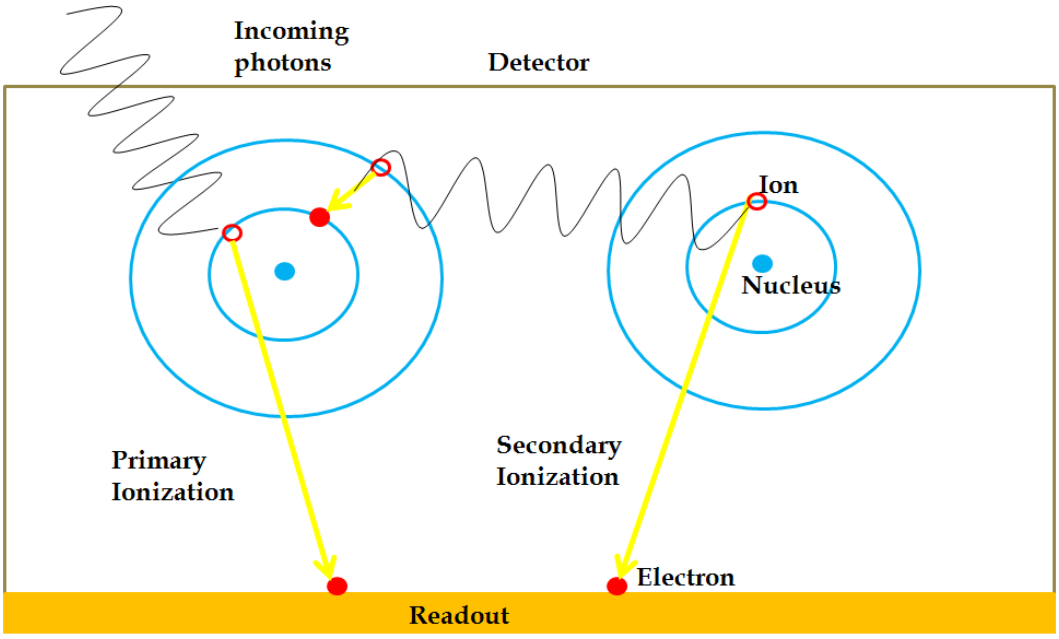

Figure 1.5: Example of a primary electron and new photon resulting from an incident photon interaction. The new photon is then reabsorbed by a nearby atom, ionizing a secondary electron in a higher energy shell [5].

The second process for an ionized atom to return to its ground state involves the release of a secondary electron through the rearrangement of several electrons in the lower energy shell. This avoids the energy loss due to a secondary photon escaping the detector entirely. Average numbers for these two mechanisms are different for each gas that could be used in a GEM detector. For argon, which is the primary ionizing gas in our chambers, approximately 15% of interactions produce a primary electron and secondary photon, while 85% produce the primary and secondary electrons [1].

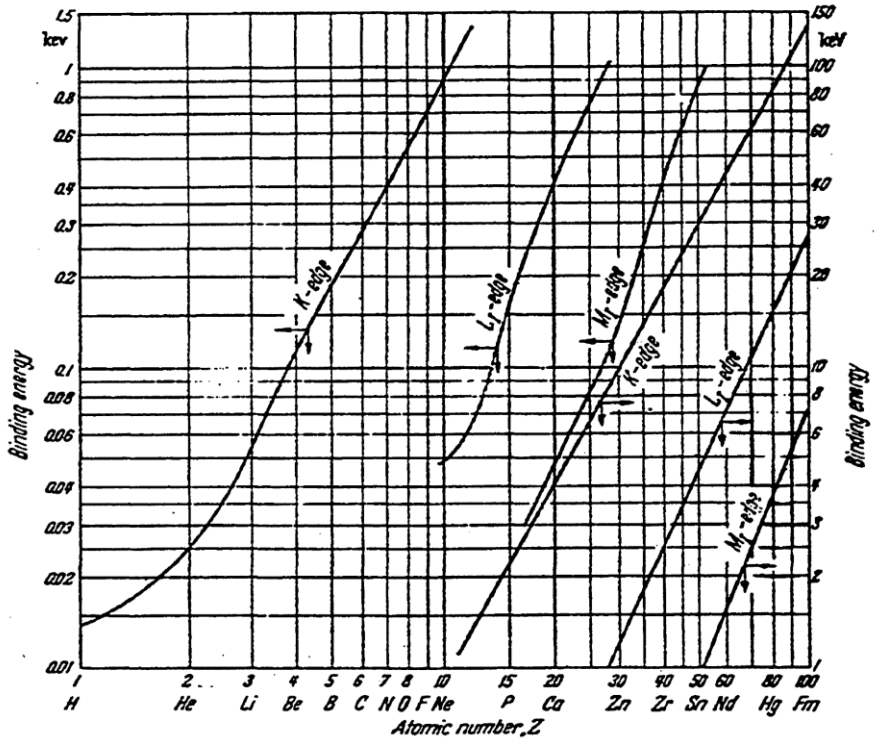

Figure 1.6: Binding energy in keV vs. atomic number of elements with curves for each of the energy shells [1].

As mentioned before, the energy of the incident photon must be at least the binding energy of the outer shell electrons of the gas used in the GEM detector in order to be detected. This binding energy quickly increases with the atomic number of the element, as seen in fig. 1.6. With a higher atomic number there are more positive charges in the nucleus, which then produce a stronger hold on the electrons bound to it. In order to measure the energy of a photon it is important that the photon has transferred all of its energy to electrons in the gas via ionization. Otherwise a reading equivalent to a photon of energy equal to the actual incident photon minus the escaped photon will be seen. For this reason it is important to consider the energy range of the X-Rays you wish to detect when choosing a gas for the GEM detectors [6].

1.3 Photoluminescence of Metals

Photoluminescence of metals is a process through which a metal absorbs the photons incident upon it and then re-emits photons of its own. This process is almost as important to understand as the ionization processes in a gaseous medium when working with a GEM detector because incident photons must first pass through the metalized layer of the Drift foil before entering into the Drift region where the ionizing interactions occur.

There are several processes through which photoluminescence can occur, but only two are relevant to GEM detector technology. The first of these forms is referred to as resonant radiation. As the name implies, the incident photons are at a resonant frequency of the metal in which they are absorbed. An equivalent photon is then very quickly re-emitted and very little energy is lost. This is because the energy of the incident photon corresponds to an absorptive energy level in the metal atoms, allowing for the quick excitation and de-excitation of electrons. This form of Photoluminescence does not interfere with the capabilities of a GEM detector because it is essentially the same photon being detected when it gets to the drift region of the detector. If the photon energy matches an ionization level, then the liberated electron becomes the first ionized electron in the GEM avalanche discussed later in section 1.4 once it reaches the drift region. This will only slightly change the energy measured due to the difference in the binding energy of the metal atom versus the gas atom [7].

The second method of interaction is referred to as fluorescence or continuous radiation. This form of interaction is a bit more complicated than resonant radiation because the energy of the incident photons does not correspond directly to the energy levels of the atoms in the metal. Instead these photons are

absorbed into the metal, causing multiple excitations. The excited atoms then produce a broad band of continuous X-ray radiation. In addition to these re-emitted X-rays, there will also be a continuum of electrons that are removed from different energy bands. When these atoms are ionized an electron from a higher energy band will settle into the now open space, which also releases an X-ray photon corresponding to the difference in the energy states. Together these two processes create a continuous spectrum of X-ray radiation referred to as "white radiation" [8].

If the energy of the incident photons is high enough, each metal will also produce one or more characteristic X-rays. These characteristic X-rays are generated by the ionization of an electron from the innermost energy band, followed by an electron in one of the outermost bands de-exciting to fill the now vacant spot. Figures 1.7 and 1.8 show the energy levels and production method for the three characteristic X-rays of copper, although copper is usually considered to only have two characteristic lines because the energy difference between the lines is so small [9]. The full spectrum for photoluminescence from copper can be seen in figure 1.9, including both characteristic peaks and the white radiation for two different energies exciting the metal.

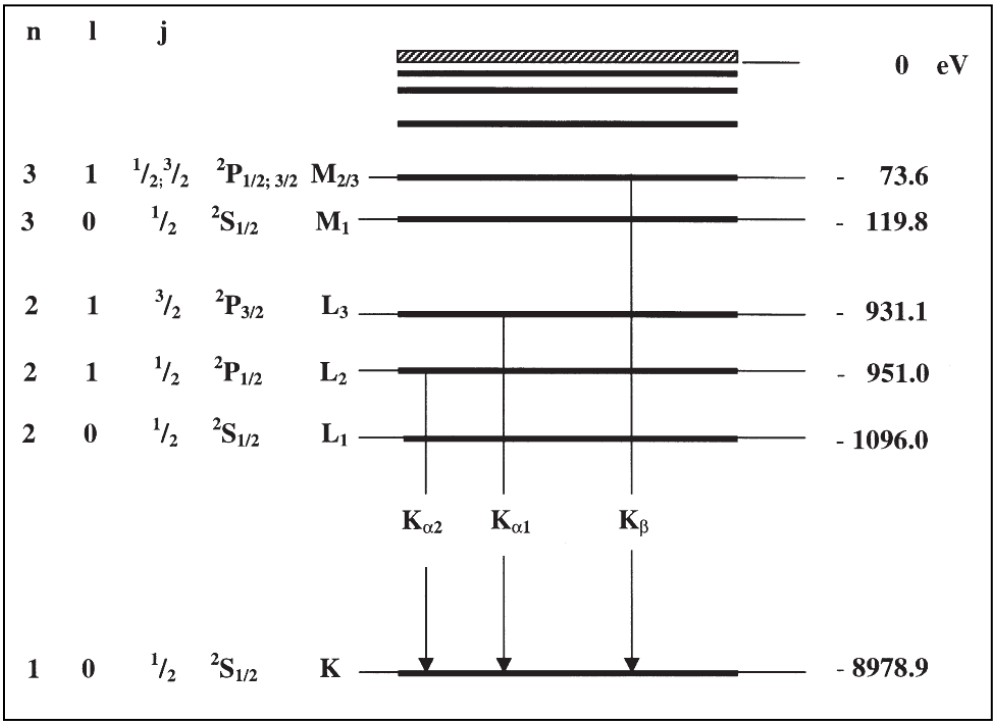

Figure 1.7: Different energy levels of electrons in copper [9].

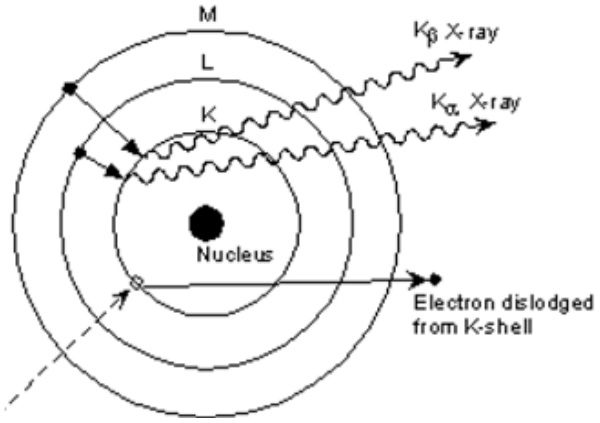

Figure 1.8: Generation of two different X-rays via de-excitation to the K shell after an initial electron is ionized from the K shell [8].

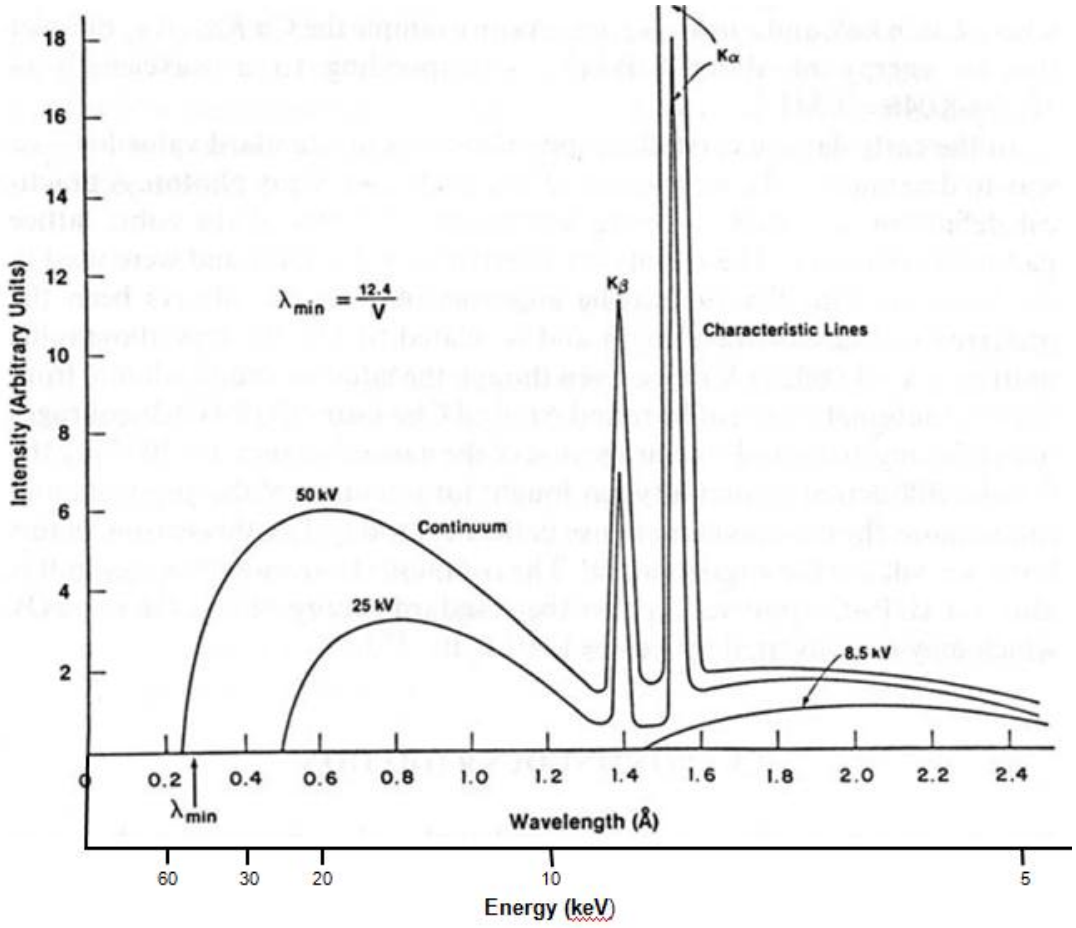

Figure 1.9: Intensity vs. wavelength and energy for both white noise and characteristic X-rays generated by fluorescence of copper. Each curve is for a different voltage applied to the metal in order to achieve these full spectra, but they are also attainable through photoluminescence [8].

1.4 Gas Electron Multiplication

We have discussed in detail the means by which electrons are removed from their parent atoms in the ionization, or drift, region of the detector. Now we shall look

into what happens to those electrons. In order to do this, we shall look at what makes a GEM detector a detector, rather than just a gas filled instrument in the lab.

Gaseous detectors have been in use and development for more than 50 years, but the development of GEM detectors is fairly new by comparison. Invented in 1997 [1], GEM detectors fall into a special category called Micro-Pattern Gas Detectors (MPGD's), which utilize a construction method unavailable in the past [10]. Some of the gas-filled detectors predating the GEM detector include multiwire detectors and Micro-Strip Gas Chambers. The need to pursue better detectors came from the inability of these past detectors to survive higher incident particle rates, as well as the need to improve the capabilities such as time, energy, and position resolution. In the end, GEM detectors have proven to have higher resistance to aging and better resolution, in addition to being faster and more cost effective to construct than their predecessors [11].

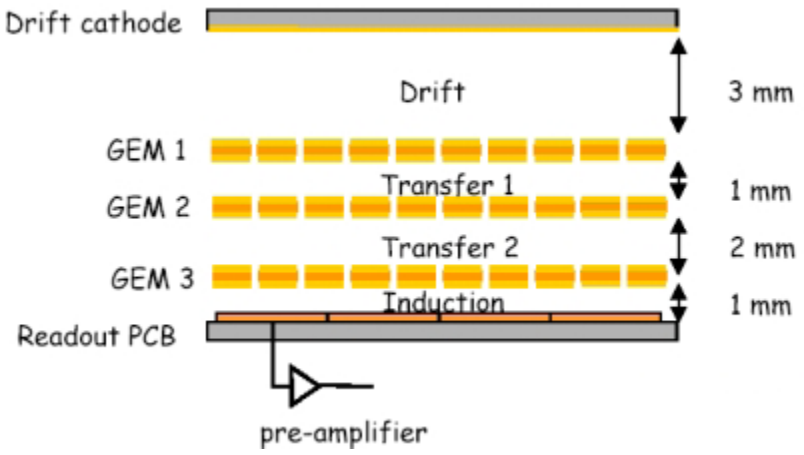

Figure 1.10: Cross section of a triple-GEM detector [12].

Figure 1.10 shows a triple-GEM detector broken down into its component parts. Starting from the top there is the honeycomb frame with the drift cathode firmly glued to the inside. A honeycomb frame is used to minimize the amount of

material above the active region while giving strong structural integrity to the detector. Minimizing material about the active region is important because it reduces absorption of particles in the frame. The drift cathode is made of a thin (usually 50 μm) insulating polymer foil called Kapton coated on one side with a very thin layer (usually 5 μm) of conductive metal. In most cases copper is used to coat the Kapton. The non-metalized side of the Kapton is glued to the honeycomb frame, leaving the metalized side open inside the detector. A negative electric potential is applied to this open, metalized side of the drift cathode, which attracts the positive ions created in the ionization processes already described. Attracting these positive ions to the drift foil is important because it keeps them from propagating down to the readout where we want to measure the electrons and reduces recombination with free electrons before they can be propagated downward [10].

Below the drift cathode there is the drift region. This is the largest open space inside the detector and is where the ionizations discussed above take place. Beneath the drift region comes the first GEM foil, followed by a transfer region. This is where the primary difference between GEM detectors is found. Early GEM detectors were constructed using a single GEM foil and no transfer region. However, this only provided a single stage of amplification for the signal created in the drift region, which was not enough to achieve the desired gas gain and energy resolution at easily managed operational voltages. Later prototypes for GEM detectors have had two and three layers of GEM foils and transfer regions, which provided a much higher gain inside the detector at lower operating voltages [12]. The function of the GEM foil and transfer regions remain unchanged regardless of how many there are inside a detector, but in terms of the detector capabilities it is important to know how many foils are inside. The detectors we constructed and

have been working with are all triple-GEM detectors, i.e. they have three layers of GEM foils and two transfer regions as shown in figure 1.10.

GEM foils are constructed of the same metalized Kapton foil as the drift foil, except it is coated on both sides rather than just on one. The metalized Kapton then has many small holes chemically etched through it using techniques and technology developed by the CERN Surface Treatment Service [10]. The etching process starts with coating both sides of the metalized Kapton with photoresist and exposing it to light through a mask for curing. After the curing is finished, acid is used to etch the hole pattern onto the metal. It is very important to properly align the etching on both sides of the foil in this stage because it is through these etchings that the final holes are completed. If the initial etchings are misaligned, then the holes will be malformed. Connecting the holes in the etching process also gives a conical shape to the finished hole that is very important and will be discussed later. When finished, the holes typically have a diameter of 70 μm and a pitch of 140 μm. The pitch is a measure of the separation between holes taken for example from center to center [10].

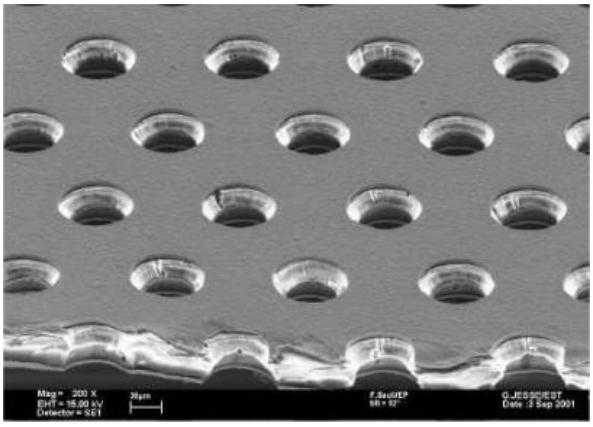

Figure 1.11: 200 times magified view with an electron microscope of a GEM foil after chemically etching the hole pattern with inner diameter of 50 μm, outter diameter of 70 μm, and pitch of 140 μm [10].

After manufacturing, GEM foils must then be stretched and framed. The foils are stretched before and during the framing process to maintain a uniformly flat surface area. It is very important for the foils to be uniformly flat with no wrinkles or folds to ensure the gain uniformity of the detector and to avoid arcing across the thin metalized layer. A GEM foil is operated with a high voltage (between 400 and 500 Volts) applied across the two metalized sides. At these voltages arcing, or "sparks", can be very damaging to the GEM foil. This is also why the conical shape of the holes etched through the GEM foils is so important. Kapton is a very good insulator, and having the extra amount between the two metalized layers at operational voltage helps in preventing any leakage current from connecting them. This shape also allows for a much smaller diameter to the hole with lower risk of sparking from one side to the other. This reduced diameter concentrates the electric field lines between the two layers (figure 1.12), increasing the gain achieved by the foil [12]

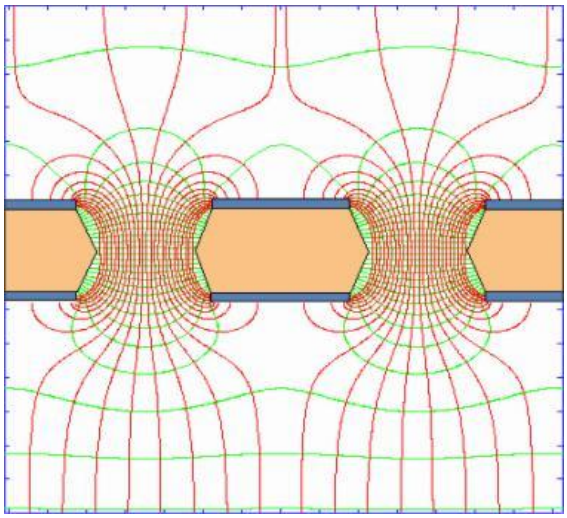

Figure 1.12: Cross section diagram of electric field lines (pink) and equipotential lines (green) for two holes in a GEM foil obtained through Garfield simulation [10].

The gain of a GEM detector is determined by the GEM foils inside it. When the ionized electrons reach the GEM foil they are caught in the strong electric field that connects the upper plate to the lower plate. They are then accelerated through the holes where the field lines have converged in much higher density. With this great increase in their kinetic energy they interact as a fast moving charged particle, causing more electrons in the gas of the chamber to be removed from their parent atoms. The ratio between the number of electrons excited after the multiplication and the number of electrons entering above the GEM foil holes (is referred to as the gain ( ) for this particular stage.

The total gain of the detector is determined by multiplying the gain of each of its stages together.

After passing through the last layer of GEM foil and transfer region, the now generated electron cloud reaches the readout board. Here the electrons induce a current, which is then read by the connected electronics to give the signal that an interaction has been detected.

Another strong consideration made when designing a GEM detector is the gas used. The ionization and electron "avalanching" will occur in just about any gas used inside the detector under the right conditions, but this does not mean that just any gas will do. Some very important attributes to look for in a gas are low working voltage, high gain capabilities, good proportionality, high rate capabilities, long lifetime inside the detector and fast recovery time from the electron avalanching [10]. It is also important to consider oxidation. Because the detectors are sealed after they are constructed, there is no opening to clean them out after

they have been commissioned. For this reason it is important to choose a gas that will not age or corrode the metal of the GEM foils.

It has been shown that the electron avalanching can be achieved in low electric fields when using a noble gas. This is due to the elemental nature of the noble gasses. Other elements form molecules, which have a much stronger hold on their electrons due to their ability to dissipate energy in non-ionizing modes such as rotation and vibration. Noble gasses are also non-reactive with metals, so there is no worry about oxidation or other forms of corroding occurring inside the detector. In the family of noble gasses it would make sense to use the heaviest element. In the case of detecting fast moving charged particles, a heavier element would extract more energy per interaction according to the Bethe-Bloch equation due to its higher atomic number and larger size, and thus give a higher energy resolution in the detector. Unfortunately Xenon and Krypton are very expensive, leaving argon as the best practical choice for normal applications [1].

The use of pure argon in the detector does have a large drawback. The emission of a photon is the only way for an argon atom to return to ground state if more energy is imparted to the argon atom than is necessary to ionize an electron. While the energy of this photon is not high enough to ionize another electron from the argon gas, it is high enough to cause secondary ionization on the metal inside the detector. This secondary ionization will cause a secondary avalanche, potentially far away from the primary ionization, which will reduce the position sensitivity and can possibly lead to sustained discharges [1].

While polyatomic molecules are not useful for the ionizing effect desired upon initial interaction, they can be very useful in preventing these secondary photons from causing a new ionization from occurring. Because of their complex

structure they can absorb these secondary emissions and enter into a non-radiative excited state. The excess energy can then be lost in random collisions, vibrations, oscillations, etc. There is a collection of molecular gasses whose non-radiative excitation levels include the energy range of photons emitted by argon. In our detectors we use a seventy percent argon, thirty percent CO_2 mix (Ar/CO_2 70:30). On top of being easily available and economically feasible for a smaller budget, this mix allows for lower operation voltages while still maintaining a high gain in the electron avalanching, as well as quenching most secondary avalanching caused by reemissions from the argon [1].

1.5 Advantages to Using GEM Detectors

There are several characteristics to GEM detectors that make them ideal detectors to be used in many different applications. Not only are they easily constructed compared to other detectors, but they are much cheaper and more cost effective than many of the alternatives. GEM detectors have proven to be very resistant to aging effects. This along with the GEM detectors ability to withstand harsh conditions such as high doses of radiation are why they have been proposed as an upgrade to the CMS detector at CERN [11].

Cost effectiveness, resistance to aging, and ease of construction wouldn't mean anything if the detector was unable to detect what we are looking for. Important qualities for this include high resolutions in time, position and energy, as well as high efficiency. GEM detectors have a time resolution on the order of 10 nanoseconds, making them capable of collection rates of 10^7 Hz [11]. Compared to some CCD cameras which only have a time resolution on the order of 10 milliseconds, the time resolution of GEM detectors is a giant step forward. Position resolution for GEM detectors varies depending on the readout used. Our

GEM detectors utilize X-Y readout strips with 400 μm pitch and analog readout, which can reach a position resolution of 50-80 micrometers. The high time and position resolution of GEM detectors along with their high efficiency, typically 96%, make them especially useful in tracking and triggering for high energy particles [11].

Energy resolution for GEM detectors is much harder to excpress because they are not sensitive to all levels of energy. This is not an issue for charged particles because they are almost always high enough energy to pass completely through a detector. Cosmic ray muons are prime examples of such particles that are of interest to be detected. Photons however are a different matter. GEM detectors are not sensitive to energy levels too much below 1 keV due to their structure. Fortunately, the energy region above 1 keV is of great interest to X-ray astronomers. In this energy range much of the material in space becomes transparent to X-ray photons, making them ideal for long range observations and measurements [13].

Another important quality for detectors is their active area. Larger active area for a detector means a larger area to detect whatever you are looking for. To date GEM detectors have been built in a variety of sizes. Our detectors are 30 cm 30 cm, giving an active area of 900 cm^2. The proposed upgrade for CMS has a trapezoidal shape of 99 cm (22 cm – 45.5 cm), yielding approximately triple the active area [14], and nearly the same active area as a wide field telescope detector for X-ray astronomy (3000 cm^2) [15]. The capability for large active area, combined with the light weight and sturdy structure of GEM detectors also makes them a promising detector for space based X-ray astronomy.

Chapter 2 Thermal Stretching of the GEM Foils

2.1 Design

Stretching the foils is a very important step in the construction process for GEM detectors. By stretching the foils we ensure that there is no sagging or creasing, giving a uniform smooth surface to apply the voltage to, which in turn yields a uniform electric field between the GEM foils. It is very important to keep the electric field uniform because this affects the gain uniformity of the whole detector. It is also important to prevent sagging on any of the foils because if the foils were to get too close they could create an arcing current between them, which could burn and destroy them.

Use of an acrylic stretching frame and an oven has been the conventional means of stretching GEM foils. The outer edge of the foil is tightly pinned between two acrylic frames and then placed inside the oven. The frames then expand outward due to the coefficient of thermal expansion of the acrylic (.0075 mm/m/K), stretching the GEM foil inside [10]. The acrylic stretching frames used to stretch 30cm 30cm GEM foils are calculated to stretch almost 0.9 mm in each direction, providing the 1 kg/cm tension required to keep the foils uniformly stretched and from sagging [6].

This is a very effective means of uniformly stretching the foils, but there are a few drawbacks. A proper clean room oven large enough to stretch even the smaller GEM foils is a very expensive piece of equipment, and not readily available to smaller institutions. There is also the issue of scalability when using an oven. With an enclosed area to do the stretching inside of, you can only stretch a foil that will fit inside the oven and you must remove the foil and frame from the

oven in order to glue the fiberglass frame that will keep the foil stretched. If you want to stretch a foil larger than the oven can accommodate, then a larger oven must be purchased and installed. This brings in the issue of available space in the clean room to accommodate one or more ovens, as well as a workspace for preparing the foils and gluing the permanent frames.

In an attempt to solve the issues involved with the use of a clean room oven to stretch the GEM foils we developed a new thermal stretching technique. Our plan was to build a rack with multiple infrared lights to directly heat the acrylic stretching frame, and thus stretch our foils. This light rack would be fairly simple to construct and much cheaper than purchasing a clean room oven, and it would solve the scalability issue of the ovens. A new rack could be built for each size foil that needed to be stretched and multiple light racks could be stored in a relatively small space. The dimensions of the rack could also be made to give enough room to work on the foil beneath it, eliminating the need to remove the foil from the heated area and the clean room when gluing the permanent frame.

Mechanical stretching is another method currently in practice as an alternative to the use of a clean room oven. In this method the GEM foil is placed in a specially made frame and connected to a number of tensioning screws that will pull the foil tight between them [16]. This allows for the stretching of larger foils as well as provides the ability to work on the foil without removing it from the stretcher, but the scalability comes at a higher price. Also, the larger the foil, the more stretching screws need to be added and more time and care needs to be put into the stretching process. Thermal stretching processes are inherently simpler and more efficient than the mechanical method because the expansion of the acrylic frame stretches the foil uniformly in every direction as long as the frame is uniformly heated.

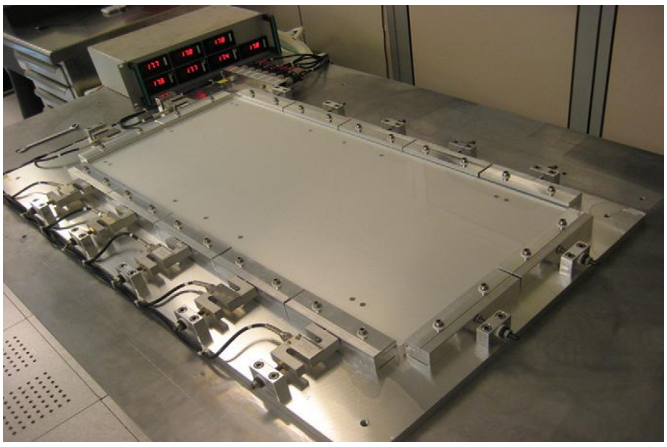

Figure 2.1: Mechanical tensioning tool for large area (1m 0.5 m) GEM foils used at the Laboratori Nazionali di Frascati [16].

There were a few different sketches for the light rack in the planning process. We looked into a wide variety of bulbs that could be used for our purpose. In the end it came down to two primary choices involved in designing the light rack. The first choice was between a hanging apparatus and a device standing on legs. Our second set of options was between conical light bulbs and long cylindrical light bulbs. If we used the conical light bulbs, their position on the rack would be dependent on whether we used legs or a hanging setup, whereas the cylindrical bulbs would have to be mounted on a down facing surface regardless.

There were several advantages to using the hanging rack rather than one with legs. The hanging rack allowed for an easily adjustable height and we didn't have to worry about creating an extra wide base in the legs to allow for the stretching frame. This also allowed more space in our stretching area so we could work with the frame and foil without removing them from the heated area.

While the long, cylindrical bulbs may have given us a more uniform heat pattern to work with, we decided to use an array of 250 Watt conical infrared bulbs.

This was decided because the conical bulbs were cheaper, more readily available, and delivered a much more focused heat than the cylindrical bulbs. In choosing this style of bulb for our heating array we also had to choose a filament type in the bulbs. For this we purchased one of each of the options, a straight filament and a "C" shaped filament. A temperature profile was then taken for each of the bulb types. As we suspected, the "C" shaped filament had a more diffuse heat pattern while the strait filament delivered a more focused heat along the axis of the filament but dropped off quickly away from that main axis.

The straight filament was found to be the better option with the axis of the filament aligned to the side of the stretching frame. In our final setup we placed two bulbs 8 cm in from each corner, leaving 24 cm between them. This allowed for equal coverage of the stretching frame after accounting for the overlap between each bulb's light patterns, as well as extra overlap in the corners.

2.2 Construction

Construction of the infrared light rack was made as simple and cheap as we could make it because one of the primary reasons for developing this new stretching method was for cost efficiency, as well as size scalability. To meet this requirement we decided to use 3/16 inch aluminum for the frame of the light rack. This is a cheap, light weight, and readily available material that would be easy to cut and drill, while also being strong enough to hold up the lights and durable enough to last. We used angle aluminum bar rather than flat because we could use the horizontal part of the bar to connect the pieces together with nuts and bolts, rather than taking them in to be welded. Figure 2.2 shows a diagram for the IR light rack that was decided upon and constructed.

For the 30 30 cm IR light rack frame we first cut two pieces of the aluminum angle bar to 120 cm and 40 cm lengths respectively. We then made a cut 40 cm in from each side in would be the horizontal part of the frame on the 120 cm piece. These cuts were made so we could bend the piece to a 90 degree angle later, forming a "U" shape. We then drilled two holes one inch apart at the appropriate locations in what would be the vertical side of the rack. These pairs of holes are what we later used to secure the light sockets to the frame. Holes were also drilled in the vertical side one inch in from the edges, as well as one inch on either side of the cut made in the horizontal side. These are the holes that would be used to hang the rack once it was completed. At this point we bent the 120 cm piece, horizontal side inward, where our earlier cuts were made to allow for this. The horizontal side of the angle bar was put on the inside both to strengthen the frame and to have overlapped material where the two frame pieces could be bolted together. This also left the flat back of the vertical side outward where our light sockets would be attached. With the bends made, we then put the ends of the two frame pieces together and drilled the two holes in the overlapped aluminum. Finally we bolted the two corners together, finishing our frame.

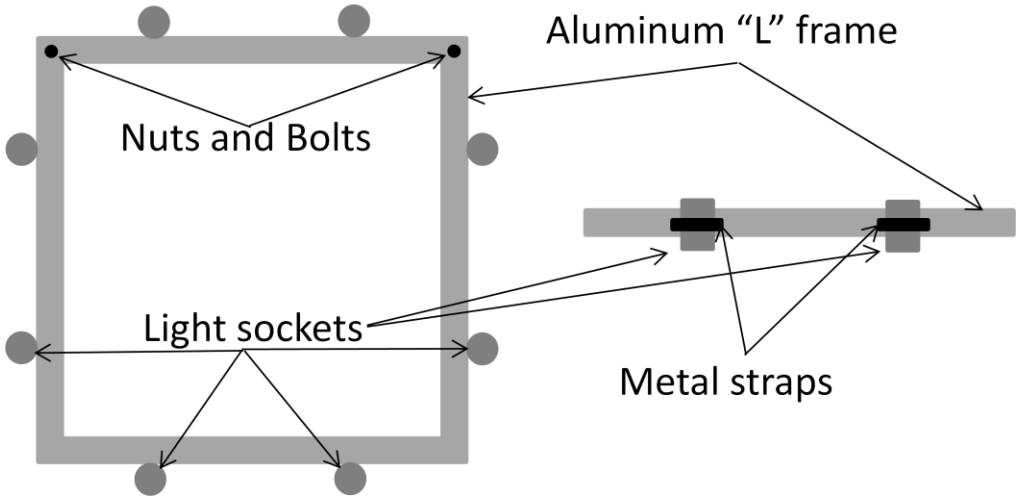

Figure 2.2: Top down (left) and side view (right) diagram of the 30 cm 30 cm IR light rack showing the aluminum L frame with horizontal side facing into the center, the nuts and bolts holding it together in the corners, and the light sockets held on by metals straps.

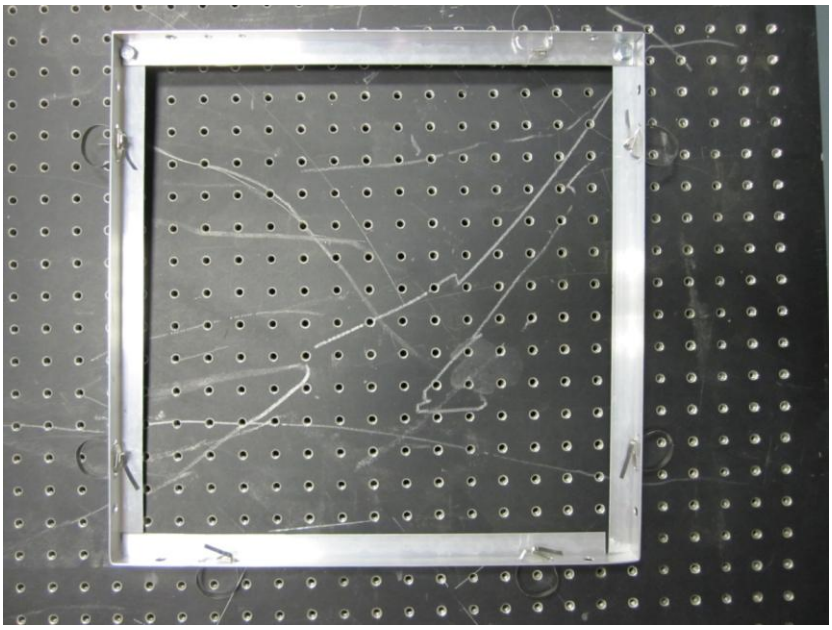

Figure 2.3: Completed frame for the 30 cm 30 cm IR light rack lying on the optical bench without the light sockets or bulbs in place.

We then wired the light sockets and attached them to their appropriate locations via metal straps. We considered using zip ties but decided metal would be better, as the lights were going to be left on for long periods of time and we did not want to risk melting any plastic parts. Four lengths of chain were then cut and looped through the two holes cut one inch from each of the edges. Two holes were used for each of the hanging chains so they could be looped through and connected outside, giving us better stability for hanging. The use of chains for hanging the light rack also gave us the ability to mark which link needed to be connected for the appropriate height. With the whole rack now completed it was hung inside of the optical bench in a clean room, as seen in figure 2.4.

Our first tests using a thermometer and an empty acrylic frame under the light rack showed temperatures of 90 degrees Celsius after one hour. This was far too hot for safe stretching of GEM foils, and would lead to over stretching, if not tearing of the foils. For this reason four dimmer switches were wired and connected to pairs of light sockets. These dimmer switches allowed us to regulate the wattage going to the bulbs, giving us sufficient control of the temperature in our stretching apparatus. Operating at the desired 45 degrees Celsius puts our dimmer switches almost to their minimum setting for the light bulbs to be turned on. However, if we wished to work at a lower temperature we can replace the 250 Watt bulbs with 125 Watt bulbs.

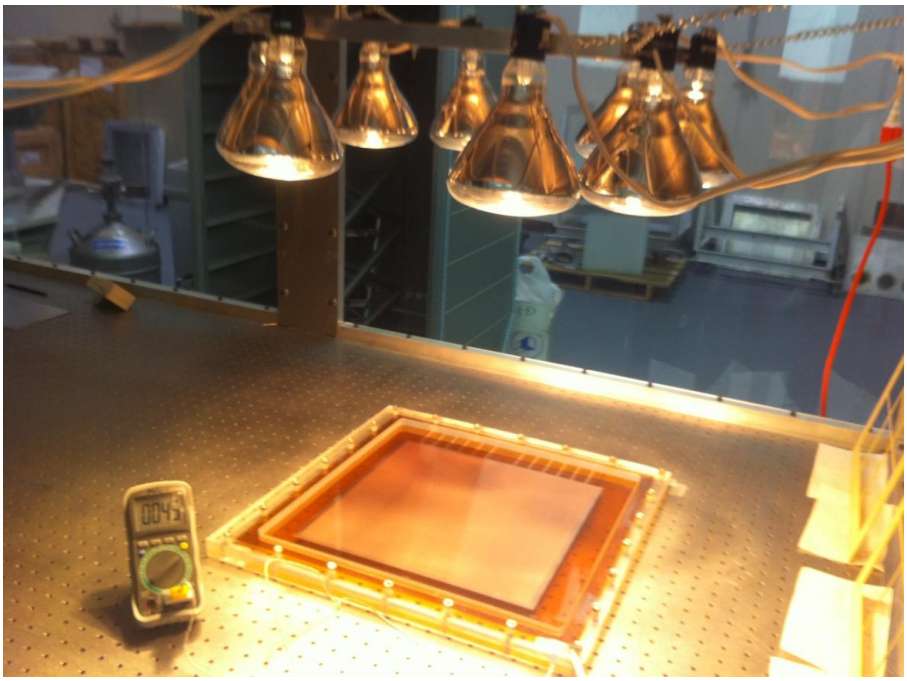

Figure 2.4: 30 cm 30 cm stretching rack turned on and stretching a GEM foil.

2.3 30 30 cm Foils

2.3.1 Temperature Uniformity Measurements

GEM foils need to be stretched uniformly in order to ensure proper gain uniformity of the detector. If one side of a foil is not stretched as tightly as the others the foil will not create a uniform electric field once the high voltage is applied to it. To achieve uniform stretching of the foils we needed to create a uniform heat pattern on the acrylic stretching frame. For the 30 30 cm foils we used the same stretching frames used in the clean room ovens at CERN, so we know they are capable of uniformly stretching the foils under proper conditions.

Our first step in testing the uniformity of the IR heat pattern was to measure the temperature along one side of the acrylic frame in set intervals as the lights in

the rack warmed up. These temperature measurements were taken with a thermocouple attached to a multi-meter. The first set of tests proved to take too long for each individual measurement because the temperature of the acrylic would change almost as quickly as the thermocouple could read. This was overcome by adding some thermal paste to the points we wished to measure, which greatly decreased the time required for each measurement. A few preliminary tests showed that two minute intervals in the beginning would yield the most information. These two minute intervals were lengthened to five minute intervals after the lights had been on for twenty minutes because the temperature beneath the frame started to change more slowly. This warm-up profile was taken for ninety minutes and can be seen plotted in figure 2.5. After that the temperature stopped changing on the five minute intervals. A much more detailed profile was taken after ninety-five minutes with the temperature checked every three centimeters and can be seen plotted in figure 2.6.

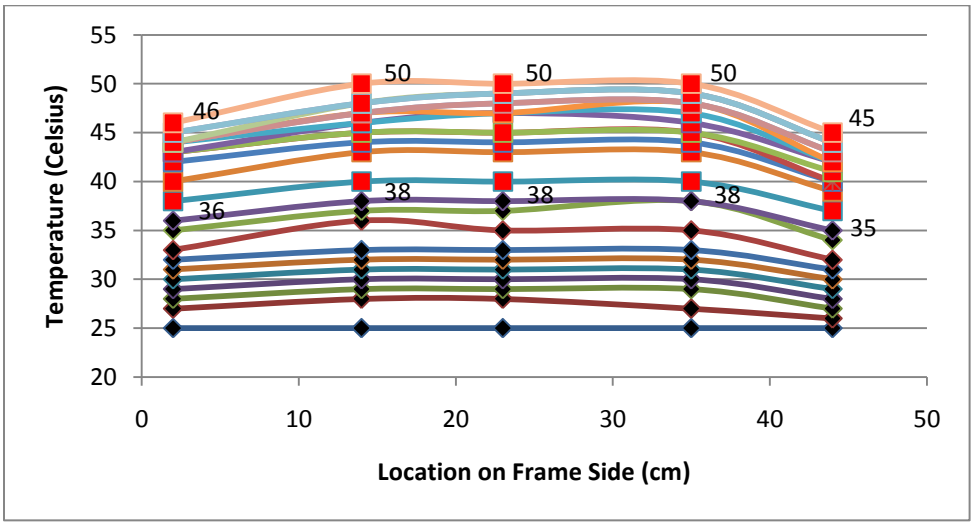

Figure 2.5: Warm-up temperature profile along one side of acrylic stretching frame under the hanging light rack. Black dots indicate data taken in a two minute interval up to twenty minutes while red squares indicate data taken in five minute intervals up to ninety minutes [17].

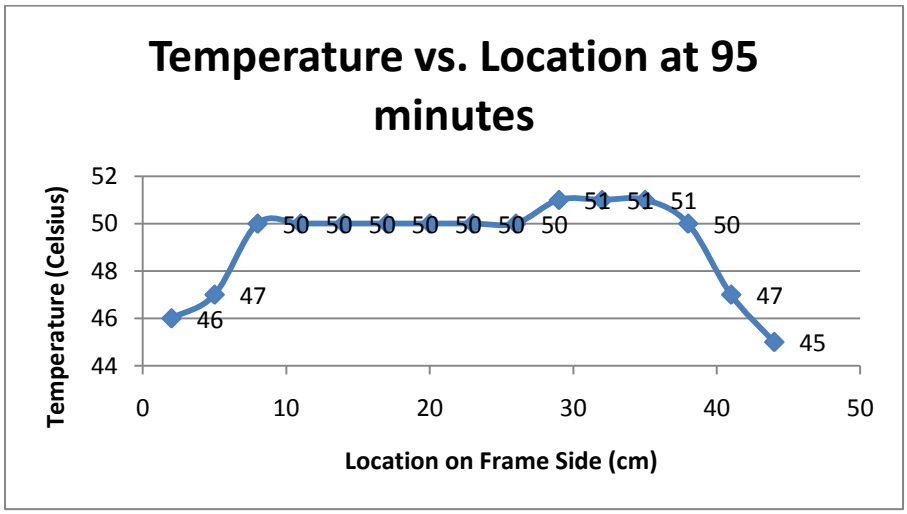

Figure 2.6: Temperature profile of one side of the acrylic frame under the hanging light rack after ninety minutes.

Although the center region of the acrylic frame proved to be very uniform, our warm-up profile showed that the corners were not getting as much heat as we had expected from the overlap of the lights at the edges. Using a watt meter and the dimmers installed on the pairs of lights we took several more profiles like this one, altering the wattage into the lights each time in an attempt to obtain a more uniform pattern. In the end, we were able to obtain a heat pattern with a three degree Celsius discrepancy between the edges and the center.

2.3.2 Stretching of GEM Foils

A total of six 30 cm 30 cm GEM foils were stretched with the infrared stretching rack and acrylic frame in our clean room. These six foils were tested for leakage currents both before and after the stretching process, and each of the foils passed this test both times. Leakage current refers to the amount of current that can

be measured from one side of the foil to the other under full operational voltage of 500 V, despite the two sides being insulated from each other. To pass this test the GEM foils must have a maximum of 5 nA leakage current in any of the 12 GEM foil sectors.

Foil	B-1		B-2		B-3		25		26		27	
Sector	Before	After	Before	After	Before	After	Before	After	Before	After	Before	After
1	1.2	1.4	0.6	1.5	4.0	0.3	1.0	1.1	1.0	1.3	1.3	1.4
2	1.2	2.6	0.8	2.0	0.3	0.2	0.8	1.1	1.2	1.0	1.0	1.1
3	1.5	1.3	0.85	3.6	0.3	0.3	1.8	2.3	1.1	1.1	1.1	1.4
4	0.4	1.1	0.1	1.4	0.6	1.2	1.4	1.0	1.0	1.0	1.6	1.0
5	0.6	2.2	0.0	1.2	0.2	0.3	1.4	1.3	1.0	1.4	1.3	0.8
6	0.6	1.1	2.0	3.0	0.2	0.7	1.3	0.9	1.4	1.3	1.5	0.8
7	0.5	2.0	0.9	2.3	0.2	0.3	1.3	1.3	0.9	1.2	1.6	1.2
8	0.4	0.9	0.2	1.3	0.1	0.1	1.0	0.9	1.0	0.9	2.3	0.9
9	2.2	1.1	0.3	1.4	0.2	0.4	1.2	1.0	0.9	1.2	1.0	1.2
10	0.6	1.5	0.0	2.5	0.0	0.2	1.2	1.5	11	1.3	0.9	1.0
11	0.5	1.2	0.3	1.0	0.6	0.1	1.2	0.9	1.0	1.7	1.1	1.1
12	0.8	0.8	0.0	2.2	0.0	1.2	1.5	1.5	1.1	1.1	1.3	1.0

Figure 2.7: Leakage currents (in nA) for the six 30 cm 30 cm GEM foils before and after the stretching and framing process.

This leakage current comes from electrons being able to move from the top side with the applied voltage to the bottom side either through the holes that have been etched in the foil or through the Kapton insulation between the two metalized surfaces. These six foils were put together into two fully constructed GEM detectors when they passed the leakage current test after being stretched and framed.

2.4 Scaling for Larger GEM Foils

Aside from the cost consideration stretching GEM foils, the ability to scale the infrared stretching method for larger foils was the next greatest incentive for

developing this new method. We were presented with an opportunity to test this aspect by building a larger IR light rack to accommodate a 99 cm (22 – 45.5) cm drift foil. This is the size being considered as a CMS upgrade at CERN where they are currently employing the thermal stretching technique using a larger, non-clean room quality oven for larger foils. We do not have a chamber large enough to properly perform leakage current testing on a foil of this size, but we did attempt an HV test in our clean room on a metal work surface. Unfortunately we were unaware that there was only 50 μm of Kapton in this drift foil, not the usual 200μm of a GEM foil, so when we attempted to apply 500 V to it a large spark burned a hole through the foil, making it impossible to perform further testing. We did, however, design and build both a new light rack and acrylic stretching frame with which to stretch this larger foil.

Construction of the larger light rack was very similar to the smaller version with only a few differences. For the larger light rack we cut each of the four sides to their proper lengths rather than cutting two larger pieces and bending them to a ninety degree angle to close the rectangle. The long sides of the light rack were cut to 105 cm and the short sides to 58 cm. These lengths were measured to place the bulbs directly over the sides of our stretching frame, just like with the smaller light rack. We did still bolt each of the ends together in the same fashion as the smaller light rack, and used the same method for attaching the hanging chains and light sockets. Light sockets were again placed 8 cm in from each corner to allow for enough light to overlap in the corners. The remaining distances were divided equally for light placement, putting five bulbs spaced 22.5 cm apart on the long side and three bulbs spaced 21 cm apart on the shorter ends. Figure 2.8 shows this larger IR stretching rack hanging inside the optical bench with all of its lights on for a temperature profile on the acrylic stretching frame.

Figure 2.8: Completed 1 m 50 cm light rack and empty stretching frame [17].

2.5 Stretching of 1 m 50 cm Foil

2.5.1 Temperature Uniformity Measurements

The number of bulbs in the light rack had to be increased in order to scale up the heat pattern for a larger stretching frame. With the increase in the number of bulbs came an increase in the possible non-uniformity to the heat pattern of the stretching rack, as well as add some issues to the power draw of our setup. An extensive amount of temperature uniformity testing was performed with the larger light rack and stretching frame before a test foil was placed inside in order to achieve the best possible heat pattern, addressing the first of these issues. The power draw issue was in blowing fuses at the sockets we plugged the dimmer switches into. The fuses we had were 20 Amp fast blow fuses. They were more than capable of handling the voltage and current drawn, but the fast blow was our

issue. Dimmer switches work by clipping the oscillation signal from the AC circuit. The fuses were being blown by the rapid changing in the current, thus our problem was solved by replacing these fuses with 20 Amp slow blow fuses.

Testing for the larger frame was done very similarly to the tests for the small frame at first. Warm up profiles and long term profiles were taken to determine uniformity, then adjustments were made to the power applied to the bulbs through the dimmer switches. We obtained a new IR thermometer to use in our testing, which allowed for much quicker and more accurate temperatures to be taken in more locations. As such we were able to measure a full temperature uniformity of the acrylic frame in a single run rather than testing one side at a time. The IR thermometer works by collecting blackbody radiation from the source it is pointed at and focusing it through lenses onto a thermopile. This thermopile converts the heat from the blackbody radiation into an electrical signal, which the thermometer reads and outputs the corresponding temperature on the digital screen.

Due to power restrictions from the fuses blowing, we had to plug two bulbs into each dimmer. We did our best to match bulbs that put out similar amounts of light and heat at the desired settings. This helped to eliminate some of the larger discrepancies in the temperature uniformity. The best temperature uniformity we could obtain for the larger stretching frame had a maximum variation of almost 6 degrees Celsius, as can be seen in the temperature uniformity map in figure 2.9. This was primarily due to the non-uniformity of the heat patterns among the light bulbs, even after adjusting the wattage applied to each bulb pair.

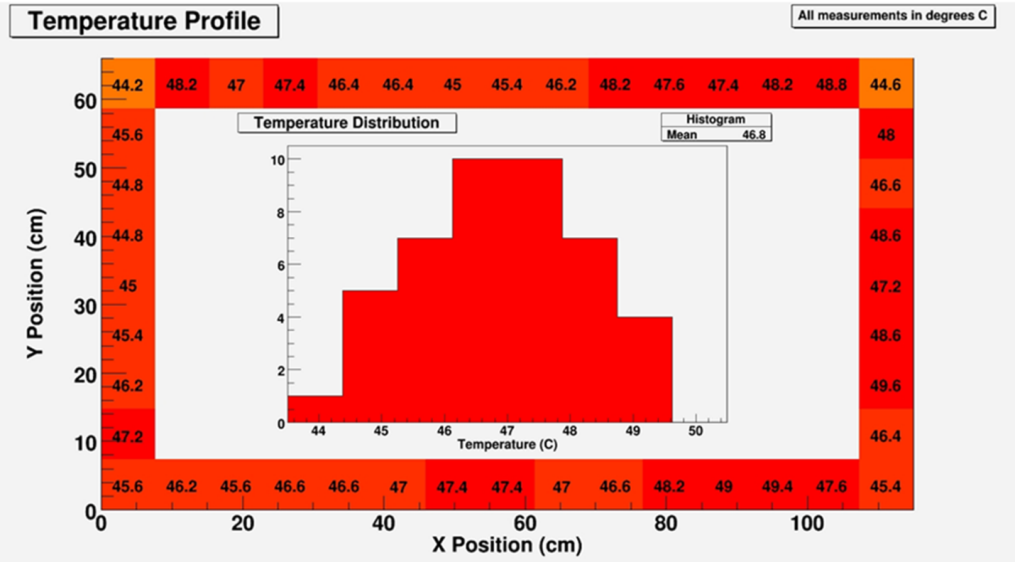

Figure 2.9: Temperature profile of the large acrylic stretching frame with temperatures (in degrees Celsius) along all four sides, as well as a histogram of all temperatures taken [17].

2.5.2 Stretching of Test Foil

We received a large 99 cm (22 – 45.5 cm) test drift foil from the CMS GEM upgrade group at CERN to test our large IR light rack. This is a drift foil made for a prototype GEM detector for a proposed CMS upgrade [14]. We did not plan to glue a frame on this foil both because we did not have a frame to glue it too and because it was only a drift foil, not a GEM foil. By the time we received a frame from the CERN lab we had already attempted our high voltage test and burned a hole through the foil, as mentioned earlier. We decided to save the frame in the event that we might receive a large GEM foil at a later date with which to perform proper high voltage testing before and after framing.

We were able to test the capability of our large IR light rack and frame. Figure 2.10 shows the drift foils successfully stretched to the appropriate tautness

that would be required for framing at 45 degrees Celsius. Upon visual inspection there were no folds or wrinkles in the Kapton or copper, nor was there any over-stretching or tearing. A new problem did arise in the first stretching of the large foil that had not been encountered in the smaller counterpart. The acrylic frame started to twist and bow on the two long sides when the foil had reached the appropriate tension. This would be a major problem for gluing a frame upon the foil because the foil would not be flat, but rather twisted on both sides. To counteract this problem we placed eight bolts along the outside of the frame to keep it from lifting from the table surface. This was an easy fix because our rack hangs above an optical bench, which has bolt holes evenly spaced across its surface. If our acrylic frame had been on a smooth surface we would have needed to find another way to hold the edges down, but the principles of the fix would have been the same.

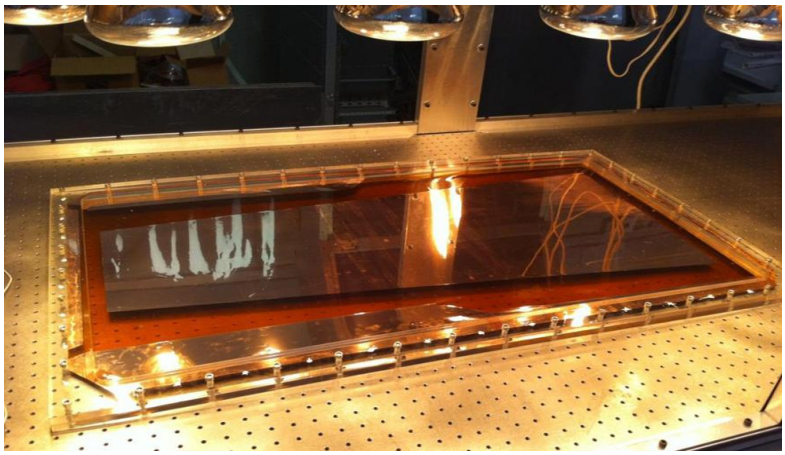

Figure 2.10: Photo of the large CMS drift foil stretched at 45 degrees Celsius under the large IR light rack.

Chapter 3 Characterizing the Detectors

3.1 Data Collection

The electronics used to readout our GEM detector include an ORTEC 124PC preamplifier, Tennelec BC202BLR linear amplifier, and LeCroy W WaveRunner 104Xi-A oscilloscope. The preamplifier is connected to the GEM detector readout via a green connector, which connects to the Panasonic AXK6SA3677YG connectors on the GEM detector. Figure 3.1 shows all of the readout electronics connected to one of the 10 cm 10 cm GEM detectors. The Panasonic AXK6SA3677YG connectors are each drag soldered using Kester #951 liquid flux, a fine, flat sided, soldering tip, and magnifying glasses, to 128 strips on the readout board. With 12 connectors, 6 in the x-plane and 6 in the y-plane, this yields 1536 possible channels to readout on a single GEM detector. Figure 3.2 shows the green connector and the Panasonic AXK6SA3677YG connector that it connects to the ORTEC 124PC preamplifier. This green connector does not have 128 channels. Instead it groups them in bundles of 8, condensing down to 16 pins. One end of an SHV cable is soldered to one of those pins, while the other end is plugged into the preamplifier. This is not the best or most efficient manner to collect data from a GEM detector, but it is the best we have to work with at the moment. The electronics capable of reading all 1536 channels of a GEM detector are currently being manufactured at CERN.

A signal from the GEM detector undergoes initial shaping and some amplification, as well as has its polarization flipped, when it is processed through the ORTEC 124PC preamplifier. That signal is amplified further depending on the gain settings chosen when it is processed in the Tennelec BC202BLR linear amplifier. From the Tennelec BC202BLR linear amplifier it then goes to the

LeCroy W WaveRunner 104Xi-A oscilloscope, where the signal is read, processed, displayed, and recorded.

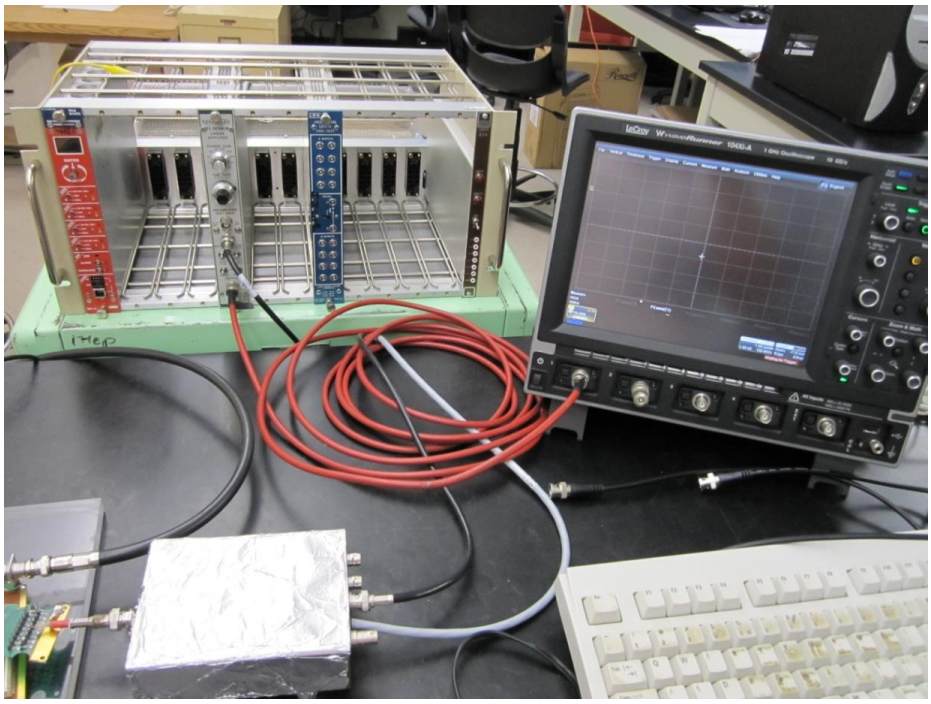

Figure 3.1: Photo of the ORTEC 124PC preamplifier wrapped in foil connected to the Tennelec BC202BLR linear amplifier in the NIM crate via a black BNC cable, which is also connected to the LeCroy W WaveRunner 104Xi-A oscilloscope via a red BNC cable.

There are two important characteristics to consider for the signal once it has reached the oscilloscope. The first of these characteristics is the minimal voltage of the signal. The minimum voltage is important because our signal is read from a current induced by electrons, which have a negative charge. This current is positive directly out of the GEM detector, but the polarity is flipped when it is processed through the ORTEC 124PC preamplifier. This makes the signal the oscilloscope receives a negative pulse, as shown in figure 3.3. In the oscilloscope settings we set a triggering level based on this minimum voltage in order to

minimize the amount of noise collected and maximize the real data for later analysis.

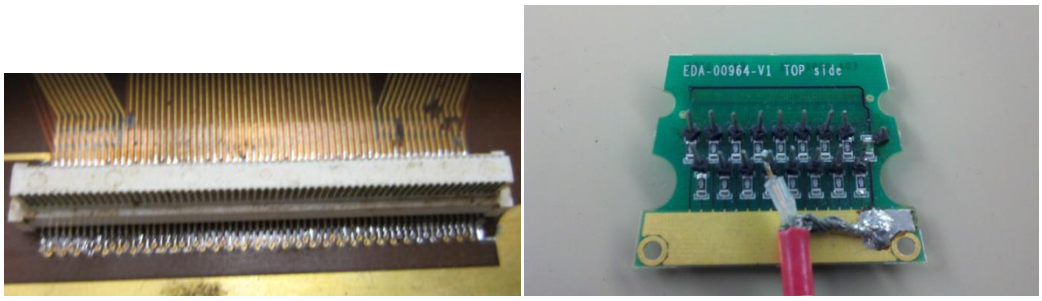

Figure 3.2: Photo of a Panasonic AXK6SA3677YG connector (left) drag soldered to the readout strips for one channel of the 10 cm 10 cm standard triple-GEM detector and the green connector (right) used to connect to the ORTEC 124PC preamplifier.

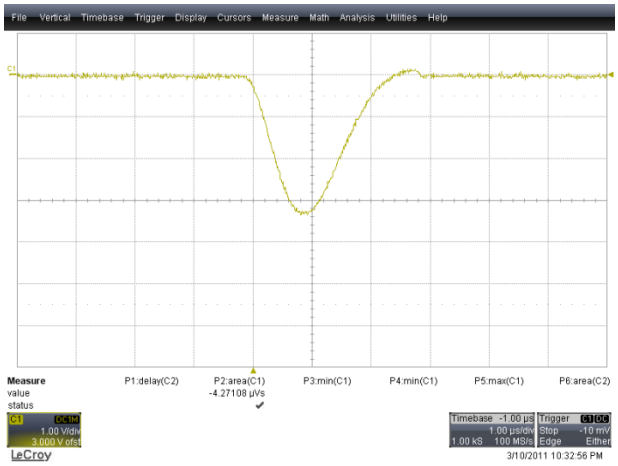

Figure 3.3: Screenshot from the oscilloscope showing a single, good pulse from the GEM detector and readout electronics for data collection.

Triggering is a very simple and effective means of ensuring minimal noise is included in a data sample. The settings we use for our triggering are on the leading negative slope of the pulse we wish to read. This means that for a signal to trigger our data collection it must have a negative slope that falls below the

minimum voltage level set. Ideally this minimum voltage would be as close to zero as allowable, but noise from the detector is usually the limiting factor in this.

The second important characteristic of a signal in the oscilloscope is the area under the signal's curve. This area represents the total charge read by the detector (ie. the full electron avalanche). Due to random path processes inside the gas of the detector, not all of the electrons reach the readout strips at the same time. This is what gives our pulses a somewhat inverted Gaussian shape. By integrating the entire area under the curve of our signal we include the charge deposited by all of the electrons. The ORTEC 124PC preamplifier also integrates the signal when it is processed, but the area data recorded was found to provide much better histograms than just the minimum peak data.

We do not have an automatic data storage program on our oscilloscope. Instead we use an excel sheet with a macro programmed into it. This macro has been refined bit by bit as testing has progressed and can be found in Appendix B. It works by connecting the excel sheet to the data readout program on the oscilloscope, and then copying the designated information into one of the spreadsheet cells. There is a counter in the macro that updates with each point taken. This tells the excel sheet how far down the column it should be copying the next point and tells the user how many counts have already been recorded.

There is another cell on the excel sheet where the user inputs the number of data points desired in the run. The macro will collect data until it reaches that number or until it is manually ended by the user. Another useful function to this macro is the recording of the start and finish times for the collection. These times are used to compute the average rate of collection, which we are just as interested in knowing as the mean energy of the particles we measure some times.

Unfortunately, the finish time is not recorded if the macro is manually ended, but the user can easily add this information. The biggest downsides to the use of an excel sheet and a macro for our data collection are that nothing else can be done on the oscilloscope during data aquisition and there is no way to save the data while it is being collected. For this reason we have plugged the oscilloscope into an uninterruptable power supply (UPS). Before the purchase of a UPS we lost a few sets of data that had not yet finished and been saved when a power surge restarted the oscilloscope.

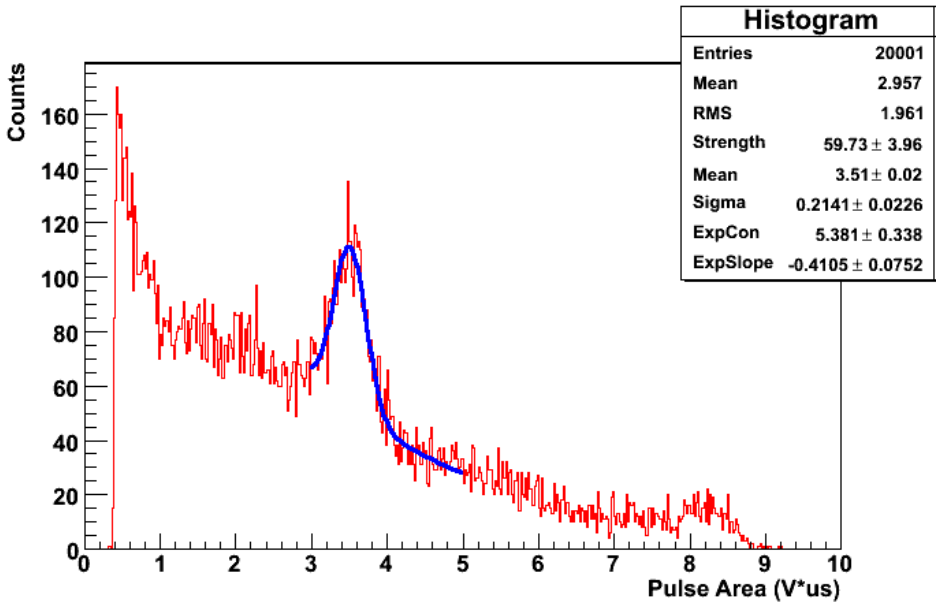

Figure 3.4: Histogram of energy levels of a Cd-109 source on a 30 cm 30 cm GEM detector with a combination of a Gaussian and exponential curve fit to the peak.

After we have finished a data set we then have to analyze it. Analysis is done with a root script, shown in Appendix C and D, which takes the recorded charge of each pulse (in V*μs) and bins them, then plots it in a histogram. The bin widths can be redefined in the root script if necessary. This plot then has a curve fit

to it based on another command in the script. For data collected with an X-ray source such as Fe-55 or Cd-109 we used a script that plots a combination of an exponential and a Gaussian curve over the main peak, shown in Appendix C. This is done by an iterative process using a user inputted range around where the main peak should be. The final output of the script is a histogram with the curve fit to it, along with a statistics box containing information such as the number of counts plotted, the mean value of the Gaussian, the error in the parameters, etc. Figure 3.4

A much simpler script is used to analyze cosmic data. Because of the energy of cosmic ray muons they are considered to be minimum interacting particles. This means the energy than X-ray pulses deposited in the GEM detector is always going to be much lower in energy and will fit a Landau curve instead of an exponential or Gaussian. The script used to fit these Landau curves to the cosmic ray muon data histograms is an earlier version of the script used for radioactive source data and is shown in Appendix D. Figure 3.5 shows a histogram of one data set fit with a Landau curve. The script works with the same process of binning, plotting, and iteratively fitting the Landau curve to the data, as well as giving the information on the curve in a statistics box in the top right corner of the plot, but it is not capable of fitting multiple curves to a single data set.

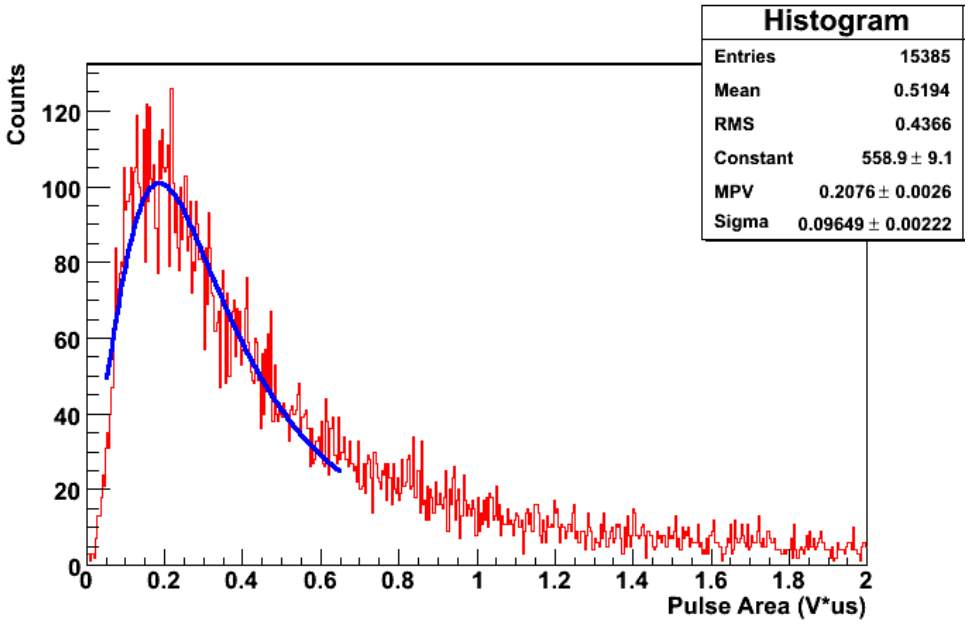

Figure 3.5: Histogram of cosmic ray muon data collected on a 30 cm 30 cm GEM detector with Landau curve fit to the peak.

3.2 Noise Hunting

The difference between background and noise is a subtle distinction that needs to be made. Background is defined as any signal from an actual source or process that occurs and leaves a detectable signal being read by the detector but is not part of what you are looking for. A background signal may contain other signals from unaccounted for sources or sources in the same field of view that cannot be removed. Background in our X-ray source data collections come from cosmic ray muons, which cannot be shielded against and are always present in our data sets.

Noise, unlike background, does not originate from a process that leaves detectable signal. It instead originates in the readout electronics connected to the

detector and, in rare cases, in the detector itself. Examples of noise originating in our detector would be sparking on a GEM foil causing a false signal, but this is a very rare occurrence. When working with a detector of any kind it is important to understand the signal you are looking for so the noise can be eliminated. One good method to hunt out noise with a new detector is to use a known and well understood signal that can be easily identified in the readout. With such a signal and very limited background, everything else should be noise. We used radioactive X-ray sources as our known signals in short collections runs to minimize the impact of the cosmic ray muons in the background.

Many steps can be taken to eliminate external sources from being included in the noise. Some of the more effective means we used in hunting out the noise in our detectors were to remove any extra electronic equipment such as power supplies for other equipment from the area around the detectors, as they proved to provide interfering electric fields which caused noise. Turning off the fluorescent lights above the detectors significantly reduced the noise as well. We also wrapped the bottom of our detectors in foil which was connected to ground in order to shield them from the electronics beneath and around the table that could not be removed.

In the case of the two smaller detectors, a sheet of Kapton was placed between the foil and the bottom of the detector to prevent contact between the foil and any metal, especially the screws holding the detector together. This would have caused a grounding issue inside the detector, which could be worse than the noise we were attempting to eliminate. Wrapping the entire detector in foil rather than just the bottom did not reduce the background at all, and proved problematic for later gain uniformity tests. For this reason we did not leave foil on the tops of the detectors.

We currently only have one preamplifier in our lab. Because of this we are limited to reading out a single connector on the GEM detector at a time. With this limitation there also comes another source of noise in our signal. When a single connector is being read by the electronics, the other connectors must be grounded to prevent charge sharing between the strips. This is done by shorting all 128 strips from each of the unused connectors to ground via adapted female Panasonic connectors. In an attempt to further reduce the noise we connected each of these capped off connectors to a common ground, but this did not affect our noise at all.

The largest source of noise came from something we believed was done to assist in our readout. The green connector shown in figure 3.2, which is used to connect the Panasonic connector on the GEM to the preamplifier, has 16 pins. Each of these 16 pins is connected to a grouping of 8 strips on the GEM readout. A wire had previously been soldered to connect all 16 pins, which meant connecting all 128 readout strips. This allowed us to read an entire connector channel (5 cm 30 cm) at once. This proved to be a large source of noise because in connecting all of these strips it also combined their capacitance in a parallel circuit. Each strip has a large surface area, which provides capacitance. Connecting 128 strips in parallel added all of that capacitance together. Small fluctuations in the voltage, combined with this high capacitance, induced charge, which then read as noise in the electronics. Connecting the preamplifier to a single pin on the green connector rather than all 16 greatly reduced the number of strips connected, and thus noise from this capacitance issue. We left the wire connecting the other 15 pins connected in order to ground out the adjoining strips and further reduce the noise.

Upon closer examination of the connector we realized there were small resistors connecting each of the pins to the grounding plate, which made our grounding wire a bit extraneous. More importantly, it meant that we had

inadvertently connected 15 of these resistors in a parallel circuit to our common ground, which was also connected to the active pin we were reading from. This large change in the resistance of our input signal could be a cause of an impedance mismatch in our electronics, which would then cause signal reflection and degradation. We had already removed every other source of noise that could be removed and shielded as best we could against the ones that could not be dealt with, so we figured this impedance problem must be our culprit.

The removal of the grounding wire on the connector strips eliminated just about all of the noise left in the detector. Before the removal of this wire we were working with the lowest gain (1x) of our amplifier and our noise triggers were as high as 200 mV. After the removal of the strip we were able to start working at a gain of 10 and triggering levels of 75 mV. Our readout capabilities were now limited by the capabilities of the oscilloscope with which we collect our data, not the noise in our detectors.

The detection of cosmic ray muons is an example of background signal that is both not noise and cannot be removed from the readings of the detector. It would take an unreasonable amount of shielding to prevent the detection of muons, which is why we are so interested in detecting them in the first place. For this reason the profile of cosmic ray muons detected by the GEM detector needs to be taken into account as much as the noise in the readout must be eliminated. To this end many hours of both low and high statistic cosmic counts were taken with each of the detectors after we eliminated as much noise as we could. These data will be discussed in a later section.

GEM 9 Pedestal			GEM 10 Pedestal		
Connector	Mean (V*μs)	Rate (Hz)	Connector	Mean (V*μs)	Rate (Hz)
Con1	0.010	37.22	Con1	-0.047	46.80
Con2	0.010	36.85	Con2	-0.047	49.92
Con3	0.009	36.99	Con3	-0.047	50.00
Con4	0.009	36.67	Con4	-0.047	50.25
Con5	0.012	36.54	Con5	-0.047	49.67
Con6	0.013	37.13	Con6	-0.046	50.17
Con7	0.013	36.76	Con7	-0.047	50.00
Con8	0.015	36.63	Con8	-0.049	51.28
Con9	0.014	36.76	Con9	-0.049	50.76
Con10	0.014	36.45	Con10	-0.049	50.59
Con11	0.015	36.58	Con11	-0.049	50.93
Con12	0.014	36.76	Con12	-0.049	51.28
Average	0.012	36.78	Average	-0.048	50.14

Figure 3.6: Tables for the pedestal data for GEM 9 (left) and GEM 10 (right). These include the mean value of the energy peak and collection rate for each of the twelve connectors on both GEM detectors.

A real test of the noise in the detectors was taken in the form of pedestal data shown in figure 3.6. Pedestal data is taken with the GEM detector HV powered to a non-operational level in order to read only the noise generated by the detector and the electronics connected to it. For our pedestal data we powered the GEM detectors with 1000 V rather than the operational levels of 4000-4100 V. This guaranteed that all of the data taken would be noise only and would not include background sources like cosmic rays. To further guarantee that our pedestal data was random noise and could not be dominated by a fluke reading, like one that might come from a power surge or random discharge, we used an external trigger source for our collection. The external trigger was taken by placing a radioactive source (Sodium-22) on a scintillator. The random nature of radioactive

decay then provided us with a sufficiently random trigger to guarantee our pedestal data was truly random.

The tables of pedestal data shown in figure 3.6 clearly show very low background noise levels in the GEM detectors at non-operational levels. As a comparison, the mean charge peak for the Fe-55 source on GEM 9 is around 2.2 V*μs, yielding a signal to noise ratio (SNR) of 18. This is very good because it means we have eliminated all of the major noise in our system and are only seeing minor fluctuations that are expected in any electronics.

3.3 10 cm 10 cm Detectors

Two prototype 10 cm 10 cm GEM detectors were constructed before the larger 30 cm 30 cm GEM detectors in order to prove the usefulness of triple-GEM detectors before scaling up. One of these smaller detectors is of a very similar build as the larger GEM detectors that we performed the majority of our tests on. It is constructed with three stretched and framed GEM foils and has an X-Y readout. Each connector channel still covers 5 cm wide, so there are only two connectors per direction instead of the six in the larger detectors. There are a few key differences for this detector compared with the larger ones. The largest difference is in the top piece of the detector. For this smaller GEM detector the top is a stretched layer of Mylar rather than the more solid fiberglass honeycomb. This Mylar top allows for testing using lower energy X-ray sources than with the fiberglass because it is much thinner and more transparent to those energies. The second major difference in construction of this smaller detector is that it is screwed together, not permanently glued and sealed. This allows for taking the detector apart to check the quality of the GEM foils after they have been in use. For an

initial prototype detector this is an important feature because it allows us to see how the internal components age with use.

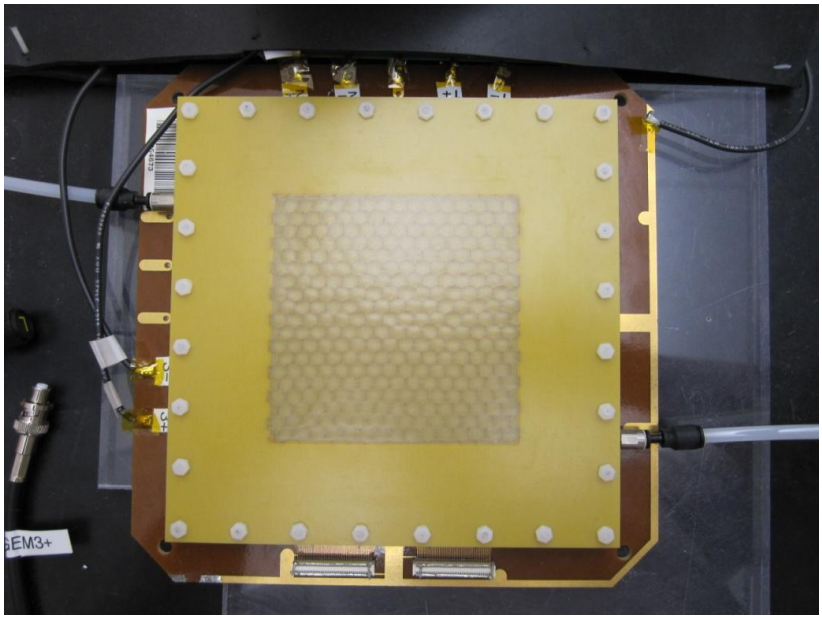

Figure 3.7: Photo of the 10 cm 10 cm honeycomb GEM detector.

The second of the two smaller GEM detectors is constructed differently. In this detector the three GEM foils and the drift foil are not stretched or framed. Instead they have an excess amount of Kapton around the edges that is not cut off, through which they are mounted on the screws that hold the whole detector together. To keep the foils flat and separated they have a honeycomb structure placed between each of them in the stack, which is why it is referred to as the honeycomb GEM detector. This detector was a prototype exploring the possibility of not needing to stretch the GEM foils at all, which is one of the time and cost limiting factor in the construction of GEM detectors. It also only has a one dimensional readout, as opposed to the two dimensional readout the rest of the GEM detectors have.

3.3.1 Standard GEM

The first tests performed were noise hunting on the standard GEM detector. The first major noise signal that we identified in this detector involved large positive pulses. This was definitely noise as our pulses should be negative, as discussed earlier. On their own, these positive pulses would not really affect our data because they simply would not trigger without having a negative leading edge. It is still important to isolate this noise though because it may be connected to other sources of noise.

Another, and much more problematic source of noise we discovered in our early tests on this small GEM detector were large bipolar pulses. These pulses started with a large characteristic positive pulse, followed by a leveled-off region approximately at ground, then a large negative pulse. An example of a bipolar pulse can be seen in figure 3.8. The positive pulse is characteristic because it had the same shape and height every time a bipolar pulse was detected, even if the other traits of the pulse changed. There was a correlation between the flat intermediate portion of the reading and the negative pulse however. The longer the signal remained near ground, the more energy there was in the negative pulse. This included both a deepening of the minimum energy triggered and the width of the negative pulse. We were never able to identify the exact source of these bipolar pulses, but we assume they were connected to the positive pulses, both because of the characteristic positive pulse and the fact that both of these noise signals disappeared together after changing our readout to a single pin on the green connector and removing the problematic grounding wire.

Periodic noise comes in the form of a signal with a noticeable frequency and is typically a symptom of an external source of noise. Many times a periodic

signal can be mistaken for random noise when its frequency is longer than the timescale of signals you are actually looking for. When we encountered a new noise signal in our detectors the first test was to zoom out the time scale and check to see if the noise was periodic or not. This happened on more than one occasion with our detectors, which because frustrating at times when we eliminated one source of noise only to encounter another with a similar profile hidden underneath it. Several periodic noise signals were caused by power supplies for other electronic equipment near our detectors; especially transformer boxes for DC powered electronics such as a laptop and our data acquisition card for scintillators.

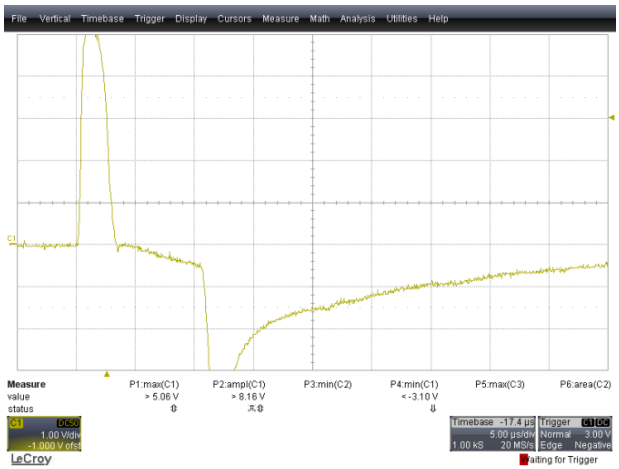

Figure 3.8: Screenshot from the oscilloscope showing a bipolar pulse.

There were a couple of instances when we believed we had eliminated all of the sources of noise we could possibly eliminate, and decided to open the GEM detector to see if any of our issues might be internal. The first thing we checked when we opened the detector was the spacing for each of the GEM foils. We found one corner to be missing one of its small spacers the first time this detector was opened, making that corner spacing 0.25 mm low. With a 2 mm total spacing between the foils, this was enough of a problem to possibly explain some of our issues. We also checked the quality of the foils compared to when the detector was

first put together. In this we looked for problems caused by sparks on the GEM foil, which would either connect the two sides of the foil by burning through the Kapton or create an area of bad electric field. This would have been a much larger issue, but we did not find any such sparking on the GEM foils.

The GEM foils were also checked for any dust or small particle debris that could plug up the etched holes or cause large sparks in the future. Even if we didn't find any debris inside the detector we decided to clean everything before putting it back together. This is done by very carefully wiping down with an ethanol soaked wipe, and then gently blowing clean with compressed nitrogen. Ethanol is used because it dries very quickly and leaves no residue, and the nitrogen is simply what we had in the compressed tank inside the clean room.

The first thing to recognize about the data taken with both the standard and honeycomb 10 cm 10 cm GEM detectors is that it was mostly taken before the grounding wire that caused the resistance issues had been removed because this particular issue was not discovered until work began on the larger GEM detectors. Repeated tests on the larger GEM detectors before and after the removal of the problematic wire proved that while the energy resolution suffered from the added noise, gain uniformity was not as affected as we had originally thought it might be.

The best way to test the gain uniformity of our detectors is with a known X-ray source. In our lab we have a collection of 9 different radioactive sources, two of which have sufficiently low energy X-ray emissions to properly test our GEM detectors. Iron-55 (Fe-55) is the best source to use, emitting an X-ray at 5.9 keV. This X-ray unfortunately has approximately 95% attenuation in our fiberglass honeycomb frames, which is why one of the smaller GEM detectors has a Mylar top, which is much more transparent to this energy level. Figure 3.9 shows a

histogram plot of one such data collection. This collection is what we refer to as a high-statistics run because of the number of counts is almost 800,000. Our typical data sets contained between 25,000 and 50,000 data points, which are enough to yield an evident peak and to plot our fitting curve while not taking too long. On average these typical data sets would take between 20 minutes to an hour to run, while the high-statistics data sets would be left to run overnight.

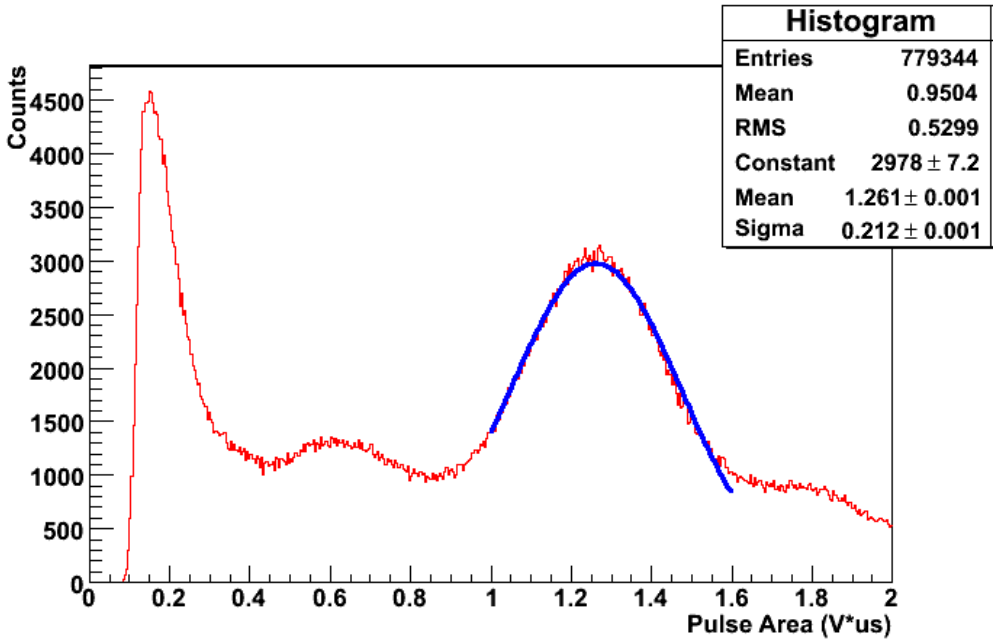

Figure 3.9: Histogram of energy levels for a Fe-55 source on the standard 10 cm 10 cm GEM detector with a Gaussian curve fit to the peak.

Unlike the data collected with the radioactive sources, all of our cosmic data sets had to be run overnight. The average muon flux at sea level is only one incident muon per square cm per minute. Our smaller GEM detectors have an active area of 50 cm^2. On top of this, these tests were performed before the noise was entirely eliminated, meaning a larger percentage of incident muons than we would have liked were lost in the noise. Figure 3.10 is an example of one of our

overnight data collections on cosmic ray muons using the standard 10 cm 10 cm GEM detector.

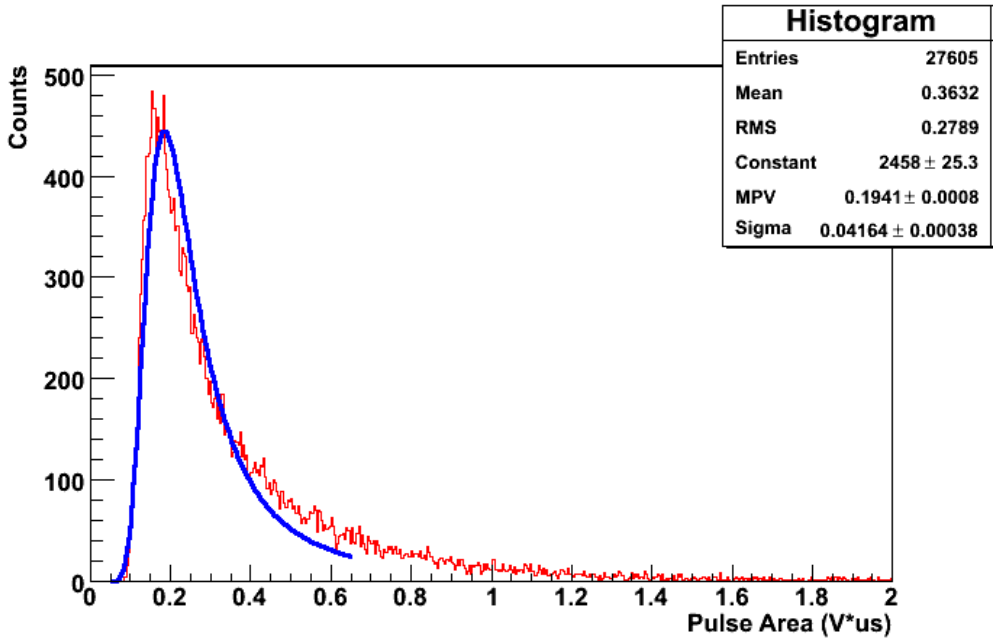

Figure 3.10: Histogram of cosmic ray muon data collected on standard 10 cm 10 cm GEM detector with Landau curve fit to the peak.

3.3.2 Honeycomb GEM

One of the time and cost limiting factors in the GEM detector fabrication comes from the stretching of the GEM foils themselves. It takes approximately half a day to stretch a GEM foil, glue it to its frame, and then let it sit in the stretching apparatus for the glue to cure. It would be a large step forward for GEM detector technology if they did not require at least a day each for construction. This GEM detector was built as a proof of concept in an attempt to find a way to build GEM detectors quicker and cheaper by avoiding the stretching process entirely and instead using a thin honeycomb structure like the one shown in figure 3.11 placed between the foils. These honeycomb structures keep the foils relatively flat and at

an evenly spaced distance from each other while at the same time filling the least amount of space between the foils with material other than the gas we want the electrons to avalanche through. Each of these points is very important.

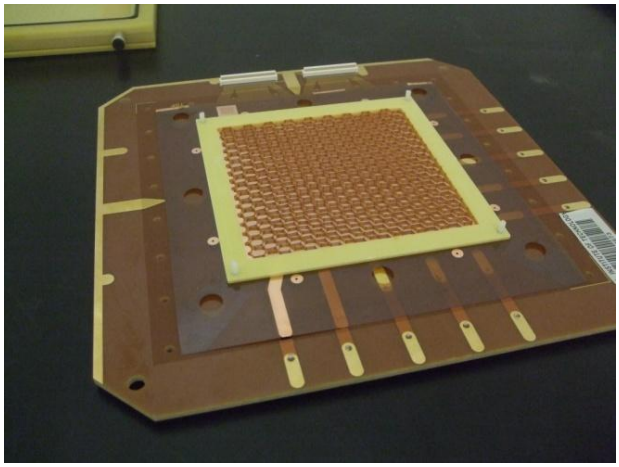

Figure 3.11: Photo of the opened honeycomb 10 cm 10 cm GEM detector with the bottom GEM foil and honeycomb spacer in place [5].

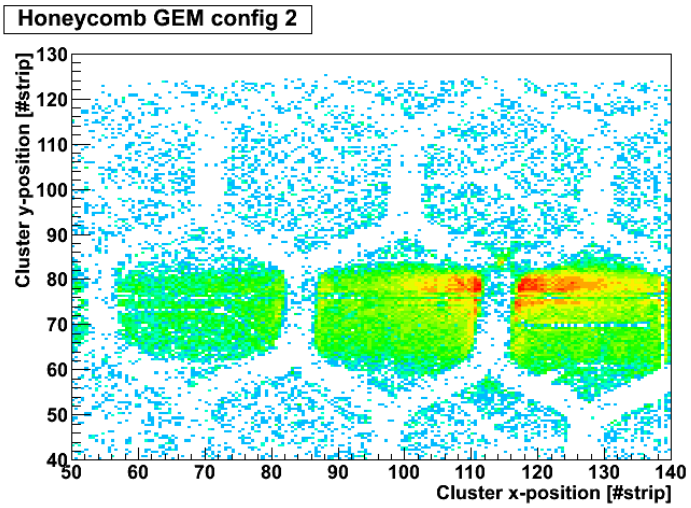

Figure 3.12: Hit occupancy of a honeycomb GEM detector showing the dead area caused by the honeycomb spacers between the GEM foils [18].

Having excess material between the GEM foils is an issue because that material will absorb the electrons it encounters instead of propagating the electron avalanche. This causes "dead area" in the GEM detector where electrons from incident interactions do not propagate all the way to the readout strips at the bottom of the detector. Groups with a fuller set of readout electronics have seen the distinct structure of the honeycomb as "dead area", shown in figure 3.12, for similar honeycomb GEM detectors even with very thin layers of material used in the honeycomb structures [18].

There are other issues with using honeycomb structures inside the GEM detector on top of these "dead areas". As a general rule, any noise that we encountered in our standard GEM detector was more pronounced in our honeycomb GEM detector. Absolute triggering levels would have to be set more than 25% higher to avoid noise, meaning any data in the lower energy ranges was lost in noise. Fibers from the honeycomb structure are also a concern. Some small fibers from the honeycomb were found on the GEM foils when we opened the smaller detectors to check their foils and clean them. These fibers, like any other particles, can cause major sparking issues and non-uniformity in the gain by plugging the holes etched in the GEM foils. Construction of GEM detectors is done in a clean room specifically to avoid these issues, but this doesn't help much if the honeycomb structure introduces them anyway.

Another added advantage to being able to take the detectors apart, aside from being able to check and clean their insides, is the ability to move the Mylar top frame from the standard GEM detector to the honeycomb GEM detector. This allowed us to perform the same tests using the Fe-55 source on both detectors.

Figure 3.13 shows a typical histogram for our radioactive source data taken on the honeycomb GEM detector. Unlike data collected with the standard GEM detector, the peak that should arise from the source data is not as pronounced. The bump in the noise dominated histogram is roughly in the same energy region as the defined peak for the other detector, but it is not nearly as resolved or easily recognized.

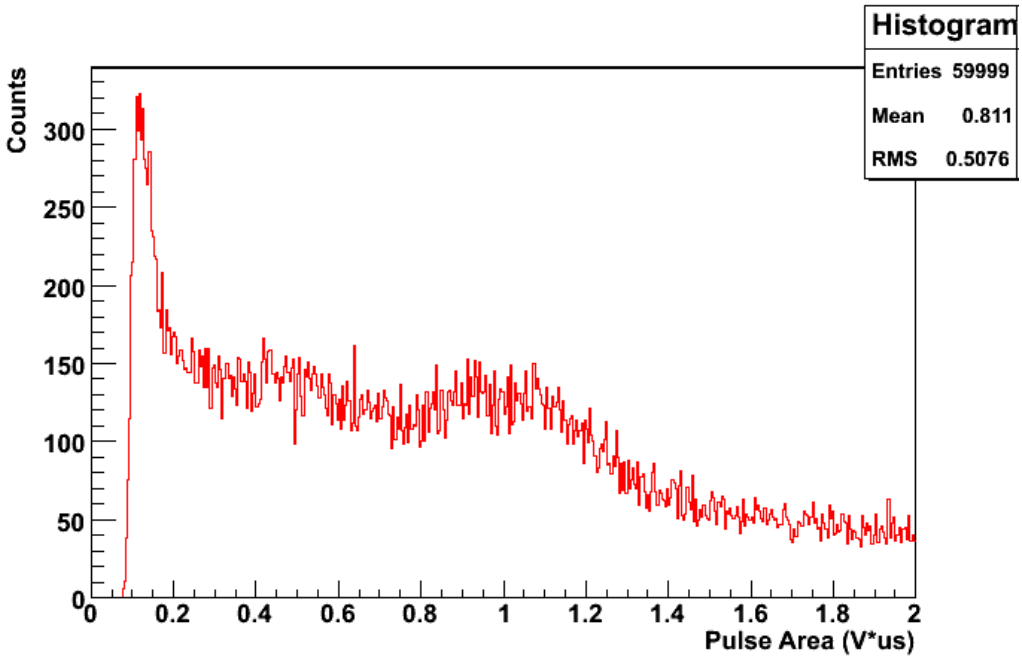

Figure 3.13: Histogram of energy levels for a Fe-55 source on the 10 cm 10 cm honeycomb GEM detector.

3.4 30 cm 30 cm Detectors

The two 30 cm 30 cm triple GEM detectors we built here using our prototype IR stretching rack are the final two detectors for a set of ten to be used in the prototype muon tomography station [5]. As such we have named these two detectors by their numbers for the tomography station; GEM 9 and GEM 10. They were both constructed in the standard fashion for GEM detectors, having their drift

foil glued to the bottom of the top structure and each of their GEM foils stretched and framed. We also had the fiberglass boards machined to the appropriate size before gluing on our readout foil. The most difficult part to this process was soldering the Panasonic AXK6SA3677YG connectors to the readout. This was done by drag soldering with Kester #951 liquid flux and a Weller PTA 1/8 inch flat soldering tip along with Magna-Sighter magnifying lenses to affix all 128 channels to their appropriate strips without connecting them to any of the adjacent strips. All of the parts were then glued into a stack, which was sealed after the glue had cured. This makes it impossible to open either of these GEM detectors without destroying them. For a much more detailed procedure for the production of these triple-GEM detectors please see the thesis by A. Quintero [5].

3.4.1 Gain Measurements

Testing the gain uniformity of our detectors was our first objective to make sure the detectors would operate properly for the muon tomography station and to validate our IR stretching process. We chose not to use the Fe-55 source in our original tests because of the attenuation problem for the lower energy X-ray in our fiberglass structure, choosing the Cd-109 source instead because it could provide us with a distinct signal in a much more manageable time frame. Choosing the Cd-109 source was not done by random guessing or happenstance. We tested each of the 9 radioactive sources we have in the lab on our detector and the Cd-109 source provided us with the best peak data in our histograms in the most reasonable amount of time. It was not until much later in our testing that we discovered the data we were collected was not in fact directly from the X-ray emitted from this source.

As discussed earlier, the Cadmium-109 source (Cd-109) has a 22 keV X-ray emission that causes photoluminescence in the copper of the drift foil, yielding instead a combination of white X-ray noise and two characteristic emission lines at 8 keV and 8.9 keV. This was discovered after we had tested each of the 72 points on both of our larger GEM detectors for uniformity and decided to run an overnight collection using Fe-55 to compare the mean values of the energy peaks. Figures 3.14 and 3.15 show histograms for the Fe-55 and Cd-109 high-statistics run respectively. Running this data collection over night meant introducing an appreciable amount of background signal from cosmic events. To counteract this problem our analysis code had to be reworked to subtract the cosmic data from the histogram.

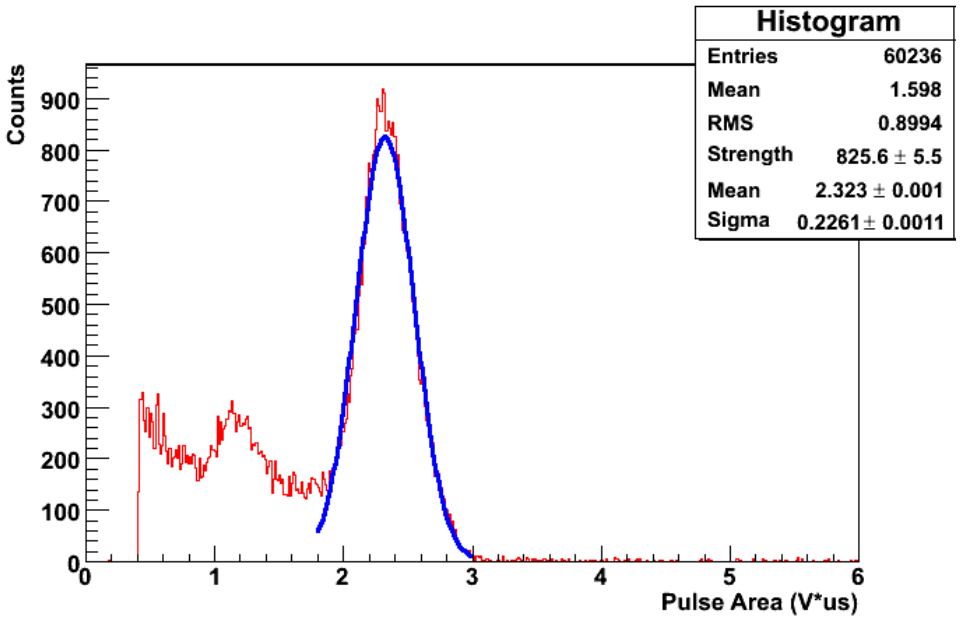

Figure 3.14: High-statistics histogram of energy levels for a Fe-55 source on a 30 cm 30 cm triple-GEM detector.

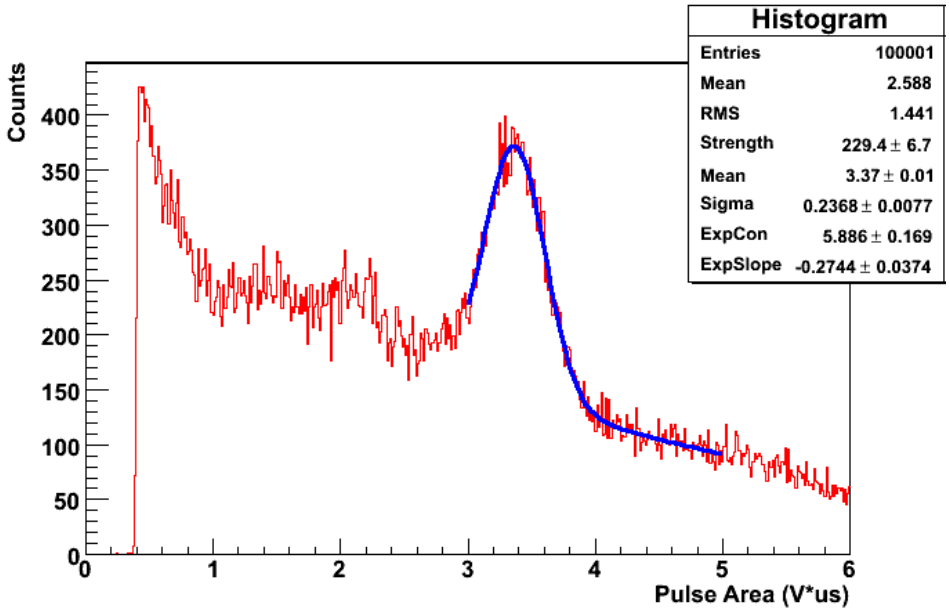

Figure 3.15: High-statistics histogram of energy levels for a Cd-55 source on a 30 cm 30 cm triple-GEM detector using the same experimental setup as for Fig. 3.14.

Our data plots up to this point were only plotted with consideration to the charge the oscilloscope read out (in units of V*μs), but with two known peaks from Fe-55 and Cd-109 at the same location on the detector the charges could be calibrated with each other to show the energy of the incident X-ray detected. Much to our surprise, and concern, the calibration was not what we had expected. We would expect an almost linear relation between the energy of the incident photon and the energy read by the oscilloscope because the GEM detectors work on a gain principle of multiplying the number of primary electrons. This gain should be the same within statistical average regardless of the number of primary electrons, therefore our relationship between incident X-rays of different energies should be linear. In comparing the two peaks, they were much too close together to represent 5.9 keV and 22 keV X-rays.

Our next step in analyzing our two peaks was to compare their relative energies to zero and calibrate them. In this method we found the relative energy difference between them to be about 2.6 keV. If the Fe-55 peak was taken to be at its appropriate location this would place our peak for the Cd-109 data around 8.5 keV. This is far short of the 22 keV we had expected to see, but fits right between the two characteristic lines for the copper photoluminescence [9]. From the RMS on both plots (figures 3.14 and 3.15), we also notice that the peak from the Fe-55 data is about 62% as wide as the peak from the Cd-109 data. This could be accounted for if we take the peak in the Cd-109 data to be an unresolved combination of the two copper peaks. This would also explain why our peak calibrates to approximately 8.5 keV.

This calibration can also be done with the Fe-55 histogram as long as there is an escape peak to compare the main photopeak location. The escape peak of argon has a known energy at 3.2 keV less than the primary peak [1]. Along with the known energy of the X-rays emitted from Fe-55 and the two locations, these two peaks are enough to perform a calibration. There is a small peak in the histogram shown in figure 3.14, which may be the escape peak, centered at 1.16 V*μs. Comparing the position of this escape peak to that of the photopeak at 2.32 yields a correlation about 9% off from the linear relationship we would expect.

3.4.2 Uniformity Measurements

Our method for testing the gain uniformity of the two GEM detectors, GEM 9 and GEM 10, was primarily dictated by our readout electronics. After removing the grounding wire on our readout connector we could only read a narrow grouping of eight strips approximately 0.3 cm wide on each channel. It made the most sense then to take our measurements in locations where data could be compared for both

the X and Y readout planes. This would allow us to see the gain uniformity of the detector as well as the charge sharing of our readout board at the same time.

Charge sharing is an important concept for the X-Y readout in our detectors. When the electron avalanche reaches the readout plane of the detector it is first incident upon the top layer of readout strips, generally referred to as the X plane because it is horizontal to the positioning of the HV board. This first layer of the readout has much thinner strips than the bottom layer in order to allow more of the electrons to induce signal onto the Y plane strips. The X strips (top layer) do still have more induced signal than the Y strips (bottom) because they are closer to the drifting avalanche of electrons. Despite the differences in the strip thicknesses, the electrons are going to be more attracted to the first conducting surface they approach. According to the COMPASS group web site [10], we expect the average energy peak of our data to be approximately 20% higher on the X strips than the Y because of this.

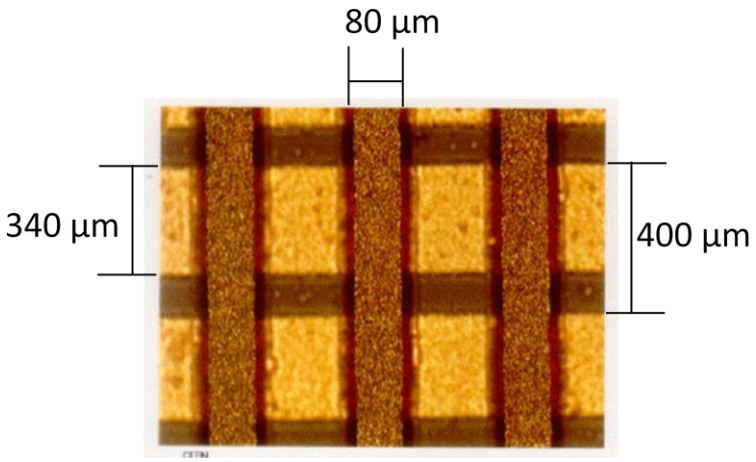

Figure 3.16: Magnified image of the X-Y readout strips using an optical microscope. Both layers have a pitch of 400 µm and the top and bottom strips are 80 µm and 340 µm wide respectively [10].

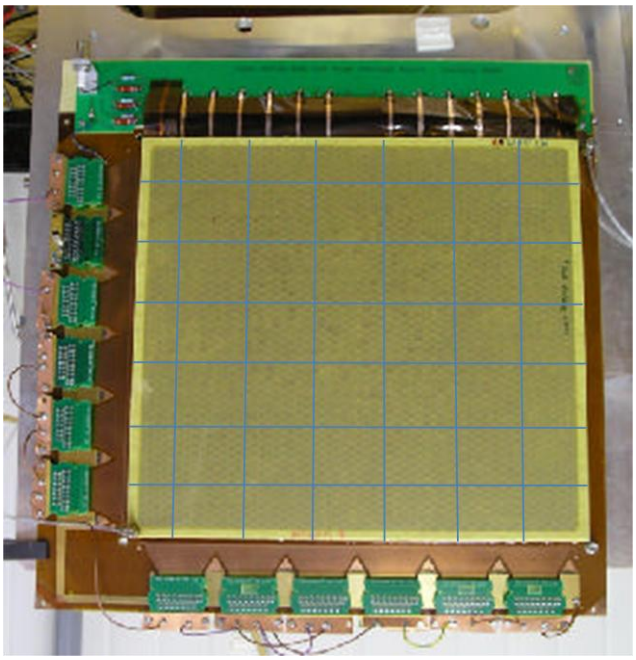

Figure 3.17: 30 cm 30 cm GEM detector marked with the same grid pattern used for our measurements.

With both gain uniformity and charge sharing in mind our decision on where to place the Cd-109 source for data collection was simply to mark where our active readout strips would cross. This gave us a uniform pattern as seen in figure 3.17, with 36 locations to test for each readout plane on the GEM detector, each evenly spaced by 5 cm from the next one on any side.

A table of the mean position of the photopeaks is compiled after collecting and analyzing the data for each of the 36 points marked on the GEM detector. This table is then normalized to the average value of these mean peak positions. Figure 3.18 shows the normalized plots for both the gain uniformity and collection rate tests performed on the X strips of GEM 9, while figures 3.19 through 3.21 are a collection of the histograms used to make the normalized gain uniformity map. All the histograms used in subsequent gain uniformity maps can be found in Appendix

E. Gain uniformity is considered acceptable if the maximum variation does not exceed 20%, which this readout plane does not. Our maximum variation was -18% in the bottom right corner with a few other scattered low points. For the most part this was a very uniform data set and is the best of the four uniformity plots obtained from our detectors with an average photopeak location at 3.65 V*μs.

Data for the rate of collection is also taken, plotted, and normalized for our uniformity map to compare to any discrepancies that may arise in the gain uniformity as well as tell us if any part of our GEM detector is not collecting properly. Having any part of the detector collecting excessively fast or slow compared to the rest of the detector would indicate some issue with the detectors. Slow collection rates could be accounted for with bad charge sharing between the X and Y readout planes. It could also be a symptom of plugged holes in the GEM foils, which would leave gaps in our active area for reading out. Excessively fast collection rates could indicate some form of discharge inside the detector that is causing a localized noise, which would also mean a bad readout area.

The normalized collection rate uniformity map for the X readout of GEM 9 has a concentrated area of low collection rates in the top center, ranging as low as -16% from the average. These low collections rates do not directly correspond to problem areas in the gain uniformity map however. A couple of locations to share a below average value in both maps, but they do not constitute a trend in this detectors capabilities. This plane for GEM 9 readout has an average collection rate of 24.35 Hz.

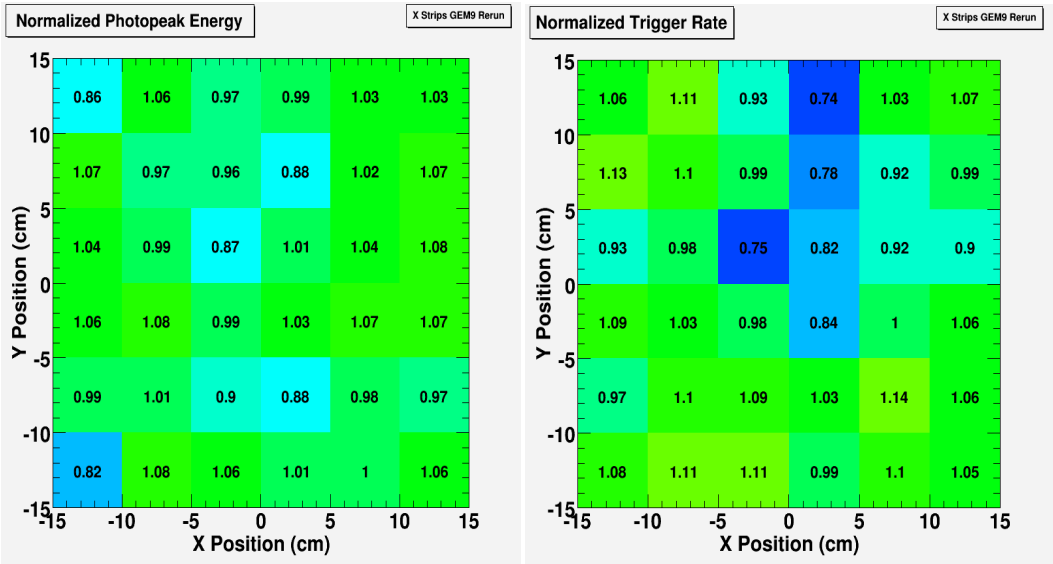

Figure 3.18: Normalized maps of gain uniformity (left) and collection rate uniformity (right) for the X-plane of GEM 9.

The Y readout of GEM 9 is not nearly as uniform as the X readout. This was by far the most non-uniform of our data sets. As can be clearly seen in figure 3.22, there are very large discrepancies in the gain uniformity, especially in the regions where no mean photopeak location data could be collected. What is meant by no mean photopeak data could be collected is every repeated data collection in this area failed to produce a peak to which a Gaussian curve could be fit in the histogram. Each point in this data set was repeated three times, each time providing the same or similar results. The reproducibility of these bad results proved that the first readings were not a fluke or simply a bad data run and there are serious issues with the uniformity of this detector in this projection.

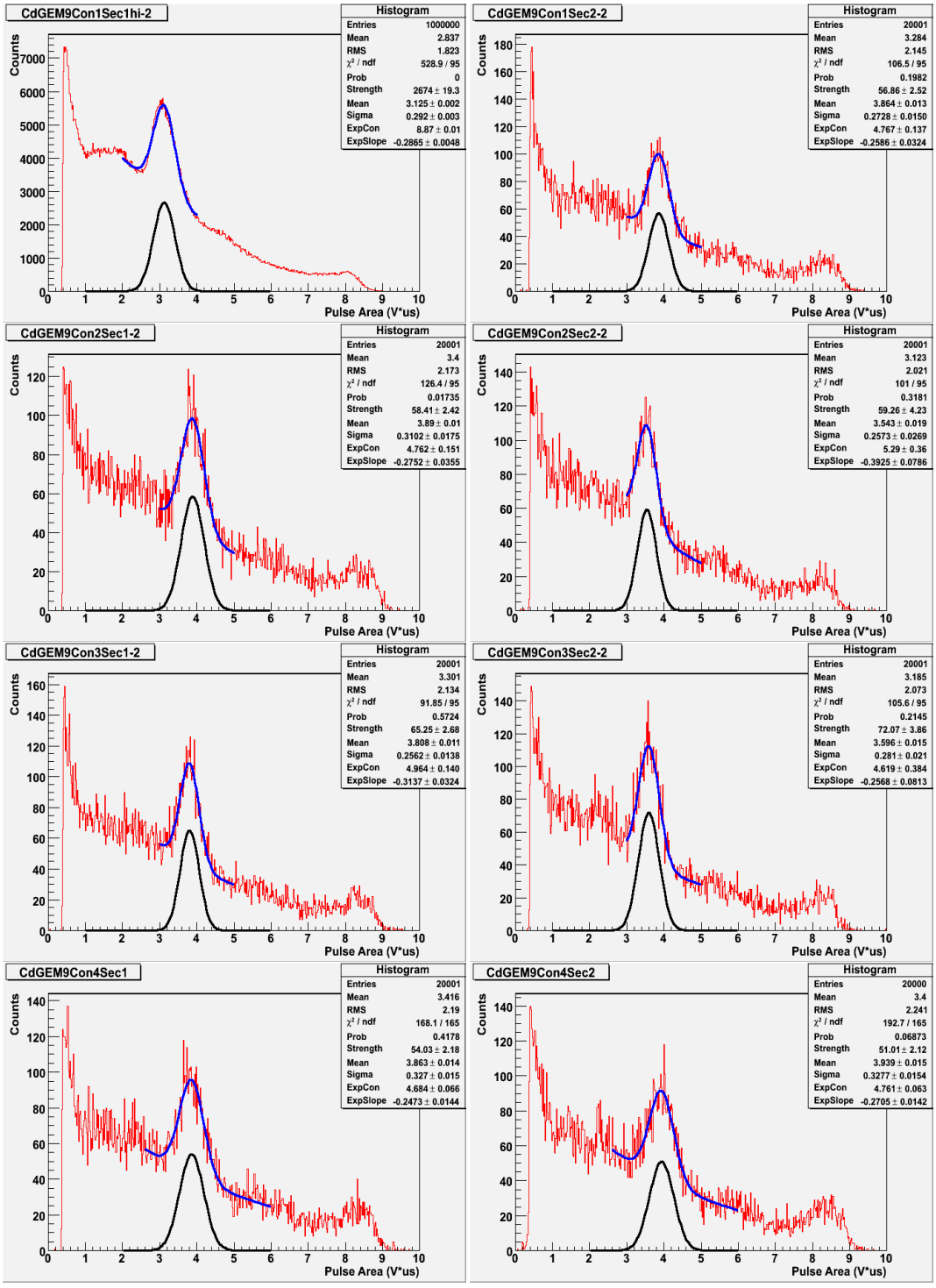
CdGEM9Con1Sec1hi-2
Histogram
Entries 1000000
Mean 2.837
RMS 1.823
χ² / ndf 528.9 / 95
Prob 0
Strength 2674 ± 19.3
Mean 3.125 ± 0.002
Sigma 0.292 ± 0.003
ExpCon 8.87 ± 0.01
ExpSlope -0.2865 ± 0.0048
Counts
Pulse Area (V*us)
CdGEM9Con1Sec2-2
Histogram
Entries 20001
Mean 3.284
RMS 2.145
χ² / ndf 106.5 / 95
Prob 0.1982
Strength 56.86 ± 2.52
Mean 3.864 ± 0.013
Sigma 0.2728 ± 0.0150
ExpCon 4.767 ± 0.137
ExpSlope -0.2586 ± 0.0324
Counts
Pulse Area (V*us)
CdGEM9Con2Sec1-2
Histogram
Entries 20001
Mean 3.4
RMS 2.173
χ² / ndf 126.4 / 95
Prob 0.01735
Strength 58.41 ± 2.42
Mean 3.89 ± 0.01
Sigma 0.3102 ± 0.0175
ExpCon 4.762 ± 0.151
ExpSlope -0.2752 ± 0.0355
Counts
Pulse Area (V*us)
CdGEM9Con2Sec2-2
Histogram
Entries 20001
Mean 3.123
RMS 2.021
χ² / ndf 101 / 95
Prob 0.3181
Strength 59.26 ± 4.23
Mean 3.543 ± 0.019
Sigma 0.2573 ± 0.0269
ExpCon 5.29 ± 0.36
ExpSlope -0.3925 ± 0.0786
Counts
Pulse Area (V*us)
CdGEM9Con3Sec1-2
Histogram
Entries 20001
Mean 3.301
RMS 2.134
χ² / ndf 91.85 / 95
Prob 0.5724
Strength 65.25 ± 2.68
Mean 3.808 ± 0.011
Sigma 0.2562 ± 0.0138
ExpCon 4.964 ± 0.140
ExpSlope -0.3137 ± 0.0324
Counts
Pulse Area (V*us)
CdGEM9Con3Sec2-2
Histogram
Entries 20001
Mean 3.185
RMS 2.073
χ² / ndf 105.6 / 95
Prob 0.2145
Strength 72.07 ± 3.86
Mean 3.596 ± 0.015
Sigma 0.281 ± 0.021
ExpCon 4.619 ± 0.384
ExpSlope -0.2568 ± 0.0813
Counts
Pulse Area (V*us)
CdGEM9Con4Sec1
Histogram
Entries 20001
Mean 3.416
RMS 2.19
χ² / ndf 168.1 / 165
Prob 0.4178
Strength 54.03 ± 2.18
Mean 3.863 ± 0.014
Sigma 0.327 ± 0.015
ExpCon 4.684 ± 0.066
ExpSlope -0.2473 ± 0.0144
Counts
Pulse Area (V*us)
CdGEM9Con4Sec2
Histogram
Entries 20000
Mean 3.4
RMS 2.241
χ² / ndf 192.7 / 165
Prob 0.06873
Strength 51.01 ± 2.12
Mean 3.939 ± 0.015
Sigma 0.3277 ± 0.0154
ExpCon 4.761 ± 0.063
ExpSlope -0.2705 ± 0.0142
Counts
Pulse Area (V*us)

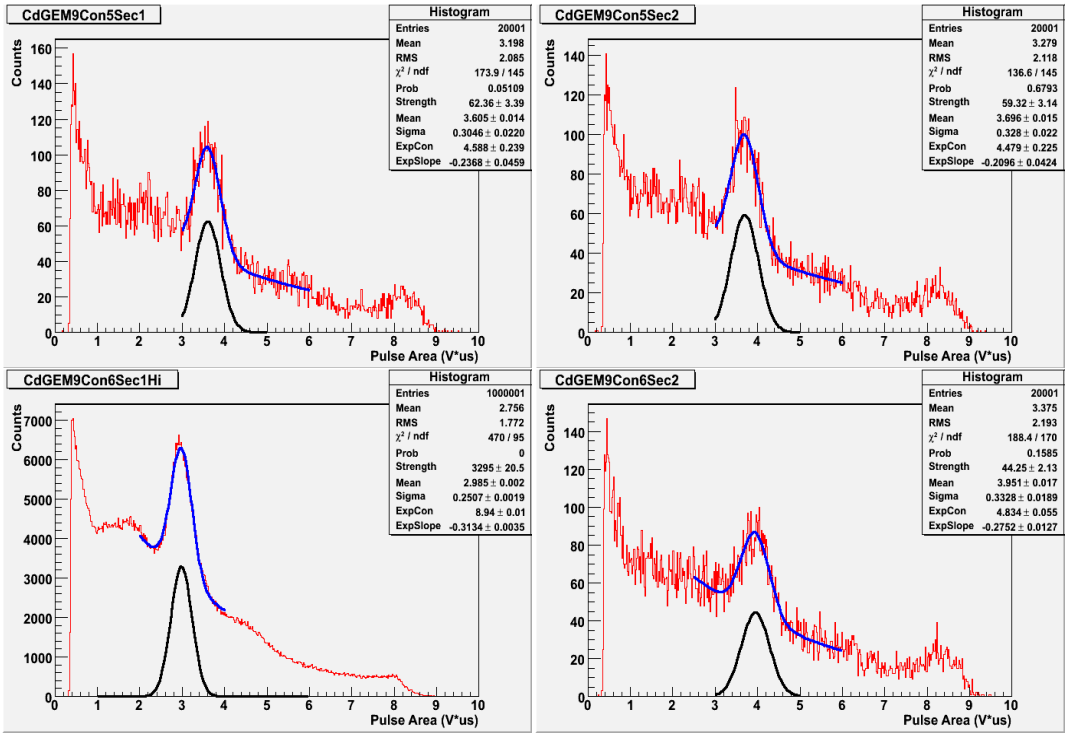

Figure 3.19: Histograms for the first and second columns of data used to make the normalized uniformity map for the X readout of GEM 9 in figure 3.18.

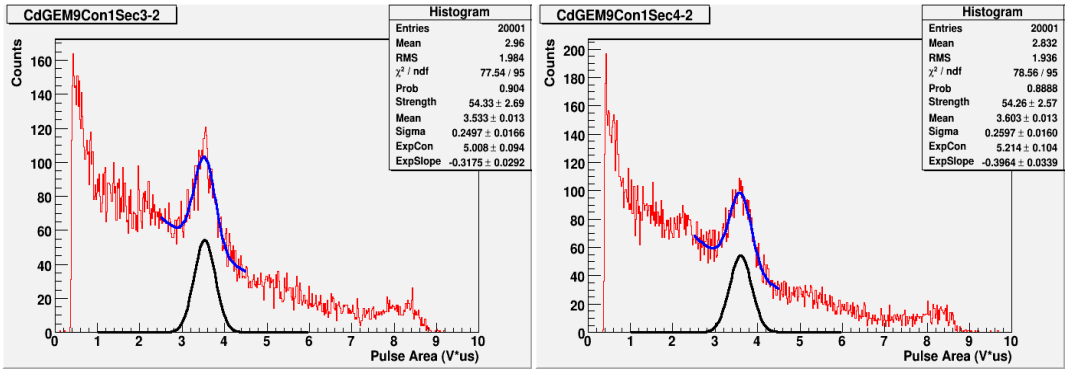

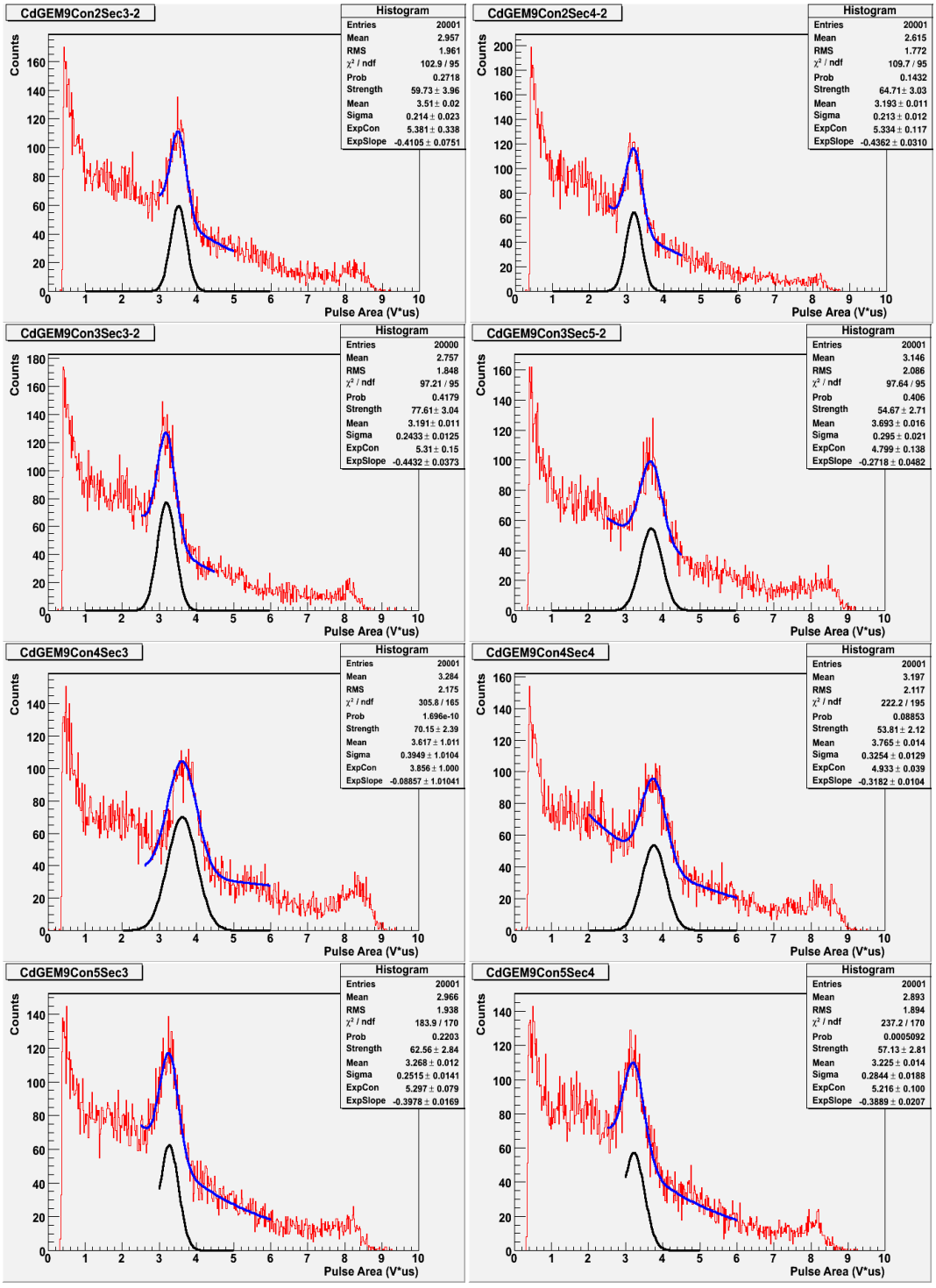
CdGEM9Con2Sec3-2
Histogram
Entries 20001
Mean 2.957
RMS 1.961
χ² / ndf 102.9 / 95
Prob 0.2718
Strength 59.73 ± 3.96
Mean 3.51 ± 0.02
Sigma 0.214 ± 0.023
ExpCon 5.381 ± 0.338
ExpSlope -0.4105 ± 0.0751
CdGEM9Con2Sec4-2
Histogram
Entries 20001
Mean 2.615
RMS 1.772
χ² / ndf 109.7 / 95
Prob 0.1432
Strength 64.71 ± 3.03
Mean 3.193 ± 0.011
Sigma 0.213 ± 0.012
ExpCon 5.334 ± 0.117
ExpSlope -0.4362 ± 0.0310
CdGEM9Con3Sec3-2
Histogram
Entries 20000
Mean 2.757
RMS 1.848
χ² / ndf 97.21 / 95
Prob 0.4179
Strength 77.61 ± 3.04
Mean 3.191 ± 0.011
Sigma 0.2433 ± 0.0125
ExpCon 5.31 ± 0.15
ExpSlope -0.4432 ± 0.0373
CdGEM9Con3Sec5-2
Histogram
Entries 20001
Mean 3.146
RMS 2.086
χ² / ndf 97.64 / 95
Prob 0.406
Strength 54.67 ± 2.71
Mean 3.693 ± 0.016
Sigma 0.295 ± 0.021
ExpCon 4.799 ± 0.138
ExpSlope -0.2718 ± 0.0482
CdGEM9Con4Sec3
Histogram
Entries 20001
Mean 3.284
RMS 2.175
χ² / ndf 305.8 / 165
Prob 1.696e-10
Strength 70.15 ± 2.39
Mean 3.617 ± 1.011
Sigma 0.3949 ± 1.0104
ExpCon 3.856 ± 1.000
ExpSlope -0.08857 ± 1.01041
CdGEM9Con4Sec4
Histogram
Entries 20001
Mean 3.197
RMS 2.117
χ² / ndf 222.2 / 195
Prob 0.08853
Strength 53.81 ± 2.12
Mean 3.765 ± 0.014
Sigma 0.3254 ± 0.0129
ExpCon 4.933 ± 0.039
ExpSlope -0.3182 ± 0.0104
CdGEM9Con5Sec3
Histogram
Entries 20001
Mean 2.966
RMS 1.938
χ² / ndf 183.9 / 170
Prob 0.2203
Strength 62.56 ± 2.84
Mean 3.268 ± 0.012
Sigma 0.2515 ± 0.0141
ExpCon 5.297 ± 0.079
ExpSlope -0.3978 ± 0.0169
CdGEM9Con5Sec4
Histogram
Entries 20001
Mean 2.893
RMS 1.894
χ² / ndf 237.2 / 170
Prob 0.0005092
Strength 57.13 ± 2.81
Mean 3.225 ± 0.014
Sigma 0.2844 ± 0.0188
ExpCon 5.216 ± 0.100
ExpSlope -0.3889 ± 0.0207
Counts
Pulse Area (V*us)

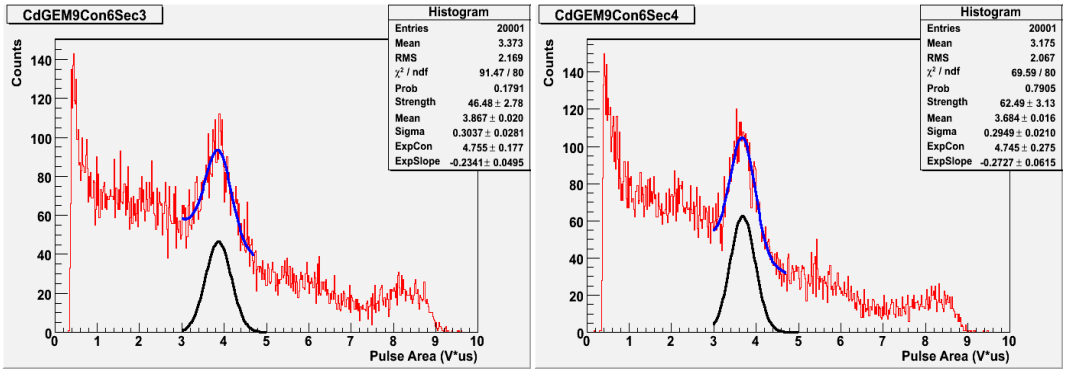

Figure 3.20: Histograms for the third and fourth columns of data used to make the normalized uniformity map for the X readout of GEM 9 in figure 3.18.

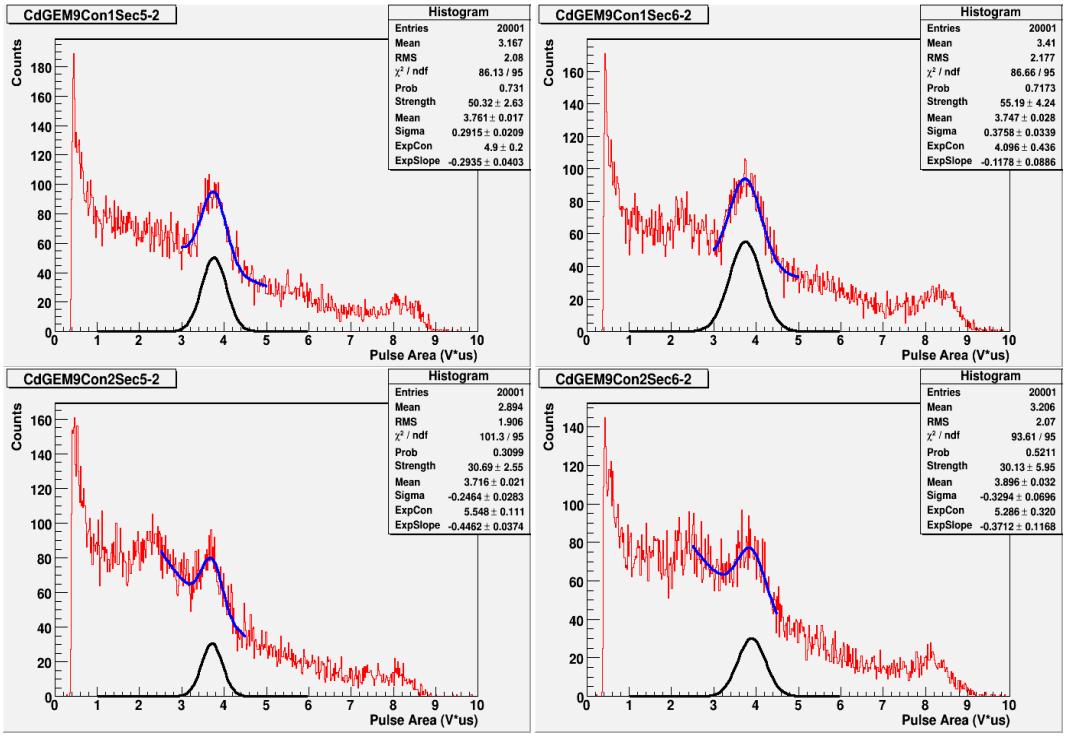

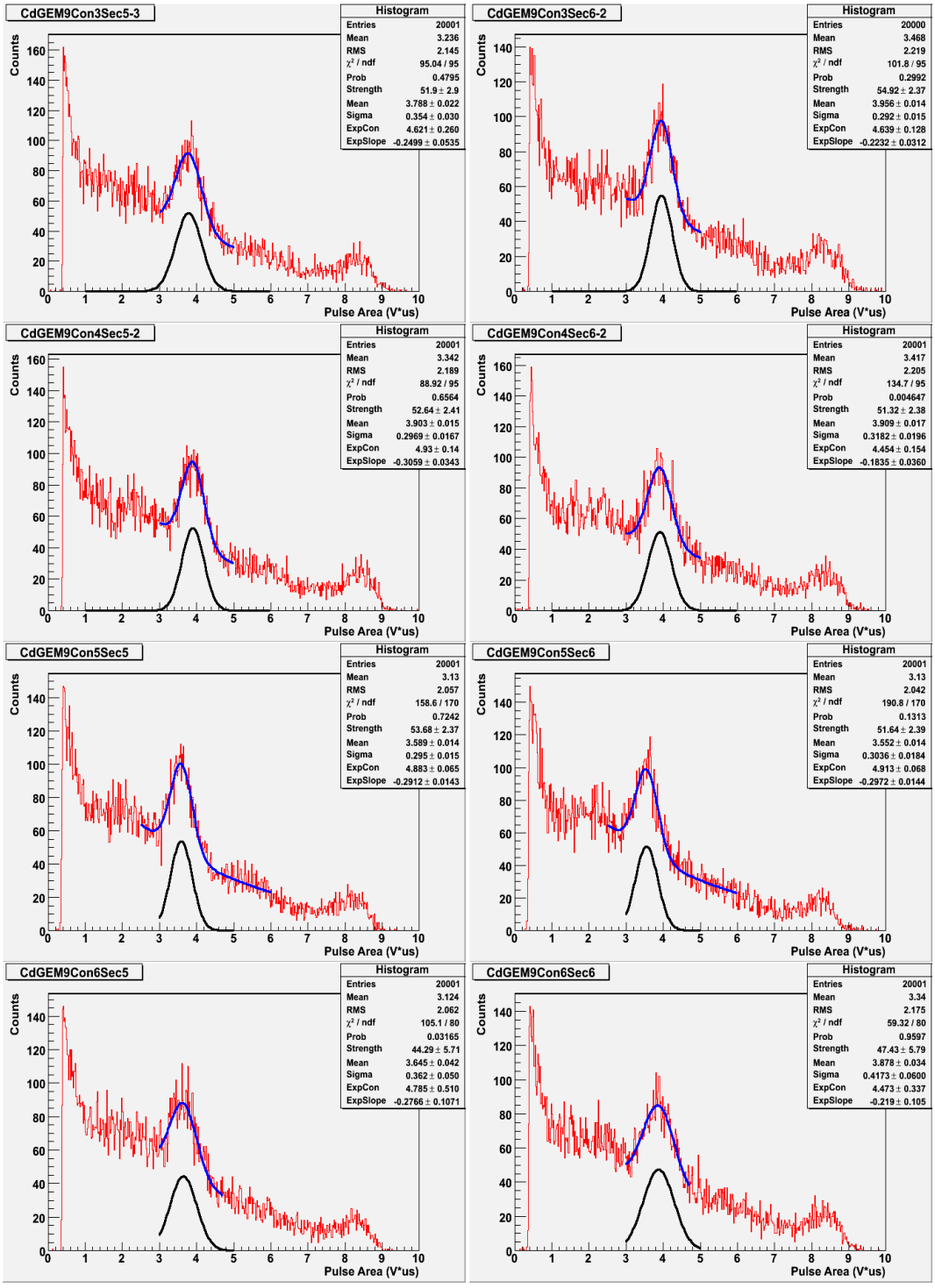

Figure 3.21: Histograms for the fifth and sixth columns of data used to make the normalized uniformity map for the X readout of GEM 9 in figure 3.18.

The sharp contrast between the X and Y uniformities leads us to believe that the problem lies within the readout board itself and not in the GEM foils or other regions of the detector. If the detector were bad, then we would have expected to see these issues on both directions of the readout, not just the Y strips. A comparison of the averages for the mean charge on the X readout and Y readout (excluding areas without a mean photopeak location found), as seen in figure 3.23, shows the X readout to be almost 10% higher than the Y readout. This is not quite the 20% that we expect to see, but it does follow the trend we expect with the X strips collecting higher charge than the Y strips.

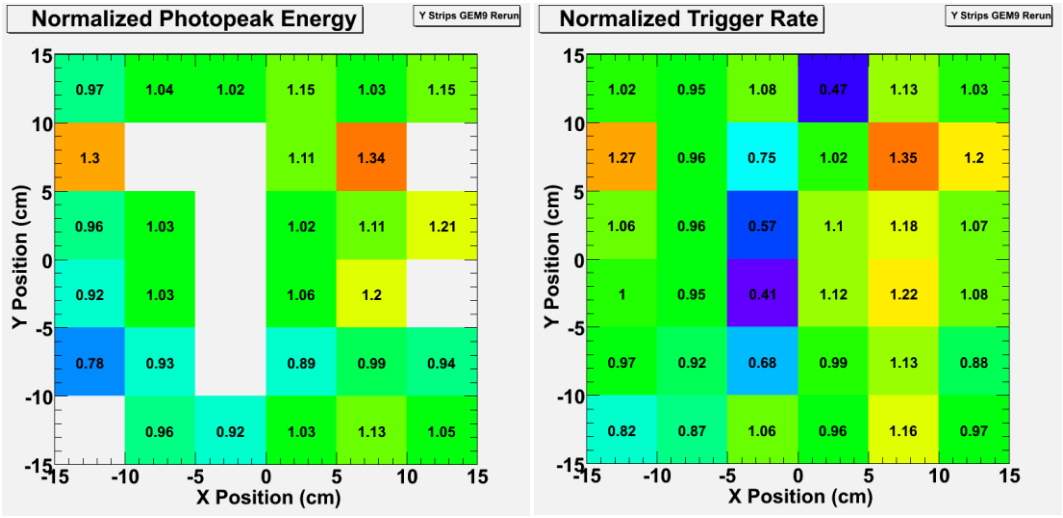

Figure 3.22: Normalized maps of gain uniformity (left) and collection rate uniformity (right) for the Y readout of GEM 9.

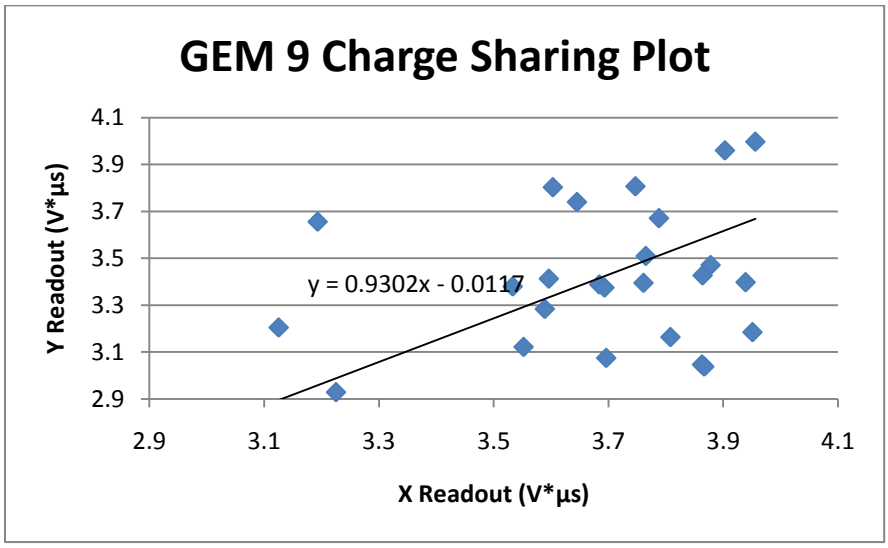

Figure 3.23: Mean photopeak locations for GEM 9 X and Y readout plotted to establish the charge sharing trend.

The rate of data collection for the Y readout does appear to share the non-uniformity of the gain measurements. We see very low collection rates in many of the areas that we failed to obtain a photopeak for. The average collection rate of the Y strips is 30.10 Hz, which greater than the average collection rate of the X strips by nearly 22%. This was not something that we expected to see in our data, but it is repeatable not only in GEM 9, but in GEM 10 as well.

Gain uniformity results for GEM 10 were fairly well behaved, with a few exceptions. Figure 3.24 shows the normalized plots for the X readout of GEM 10. Here we can see one area in the top left corner that appears to have an excessively high energy compared to the rest of the detector. It is also surrounded by areas of above average energy. This is indicative of a localized problem in the gain of our GEM detector although the point in the far corner is the only one outside the 20% variation that we consider to be acceptable. There are also a few locations with below average energy levels, but again they fall within what we consider to be

allowed. The bottom left corner however does not show any photopeaks. Not including the bottom left corner, the average photopeak location for the X readout of GEM 10 was 2.87 V*μs, and the average collection rate was 21.41 Hz.

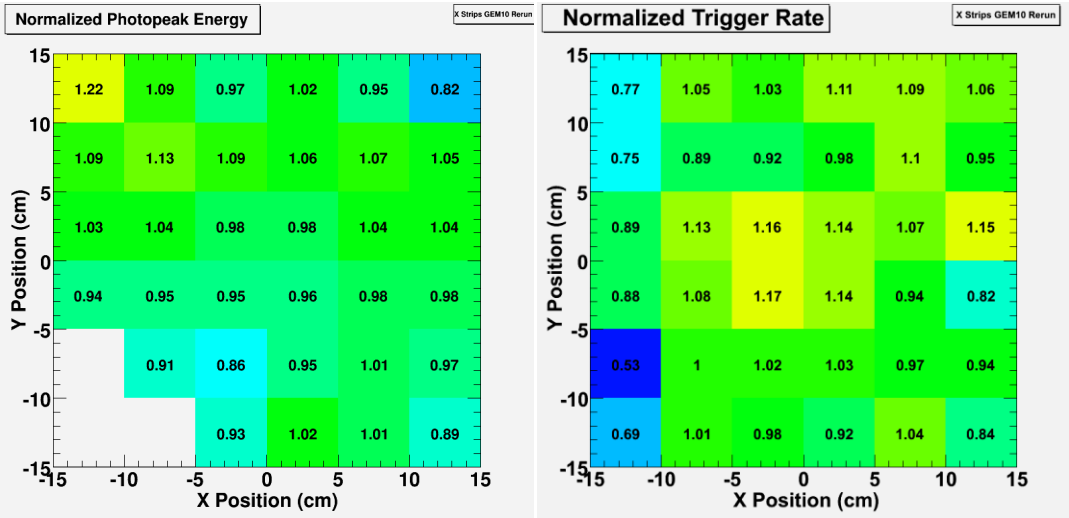

Figure 3.24: Normalized maps of gain uniformity (left) and collection rate uniformity (right) for the X-plane of GEM 10.

We do not consider the lack of photopeaks in the spectra for these locations on GEM 10 to be related to the problems with the Y strips on GEM 9. In GEM 9 we were able to obtain very good uniformity data on the X readout, even in the locations that did not provide data on the Y readout. The bottom left corner of GEM 10, however, lacks data on both the X and Y readouts in this localized area. These problem areas were extensively tested for reproducibility, and indeed proved to be reproducible problems and not just an isolated bad data set.

The data collection rate for the X and Y readouts of GEM 10 do again correlate to these problem areas in the detector, showing much slower rates where our data has issues. The top left corner shows a rate at 23% less than average on the X plane and points in the bottom corner where no data is available collect at

nearly half the normalized rate. There is also a pattern of low collection rates surrounding this problem area which corresponds to areas with photopeaks below the average for their planes.

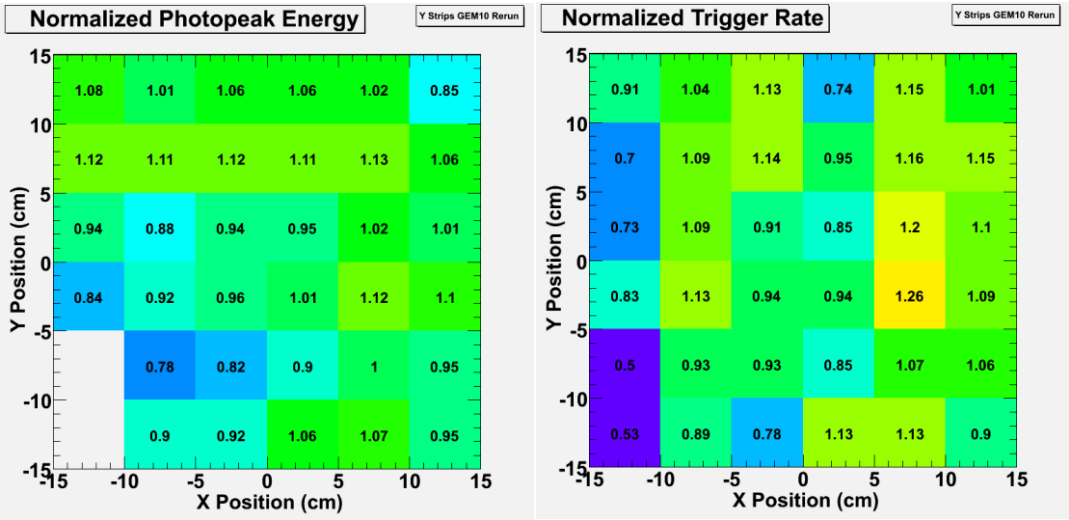

Figure 3.25: Normalized maps of gain uniformity (left) and collection rate uniformity (right) for the Y-plane of GEM 10.

The gain uniformity of the Y readout for GEM 10 does not exactly correspond to the X readout. We do see a slightly elevated charge level in the top left corner, but not nearly as much as would be expected if there was indeed a localized increase in the gain of the detector. There are only a few locations outside the bottom left corner we have already identified that we might suspect to have issues in this data set, and they all have below average energy levels. The top right corner of GEM 10 does appear to be uniformly low in its gain on both planes of the readout. The other low points near the bottom left corner seem to be correlated to the much larger problem of not being able to achieve any resolvable photopeaks in the near the corner. Mean photopeak location for the Y readout of GEM 10, not including the corner locations, was 2.26 V*μs and the mean collection rate was 28.09 Hz.

Charge sharing for GEM 10, as seen in figure 3.26, does fit well to the expected values. The average mean energy peak for the X plane is approximately 24% higher than the average on the Y plane. This is much closer to the expected 20% difference than was found with the test on GEM 9.

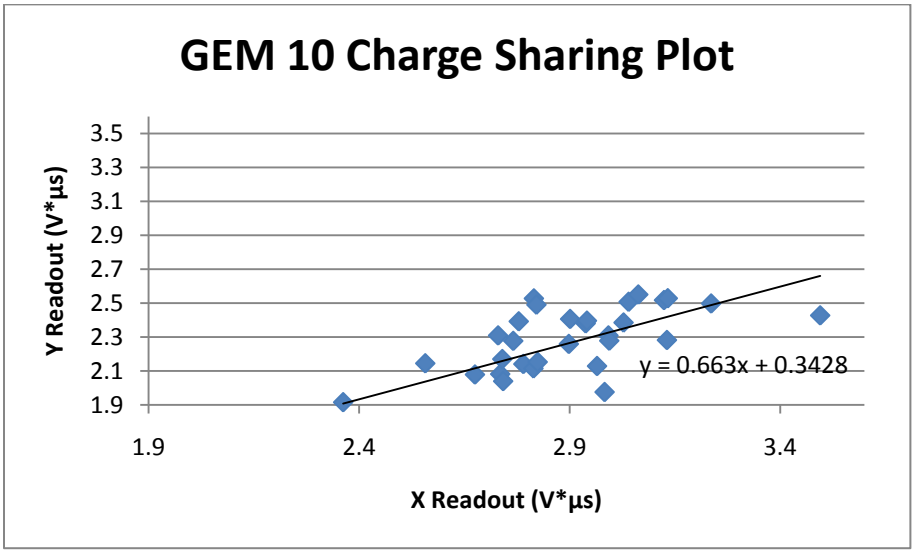

Figure 3.26: Mean photopeak locations for GEM 10 X and Y readout plotted to establish the charge sharing trend.

All of the data collected on both GEM 9 and 10 have been collected under as similar conditions as possible. Our electronics have all been set to the same settings for every run included in mapping the uniformity of these two detectors. There were many occasions when settings would be changed to perform another test, but they were always changed back and checked before we continued in our uniformity collections. These settings include the gain of our amplifier (10), the operational voltage from our high voltage supply (4100 V), and all of our oscilloscope settings (triggering level, energy resolution, and time resolution).

With this in mind, there does not appear to be a good correlation in the absolute gain of our two GEM detectors. In the units of the oscilloscope (V*μs), the average charge for the X readout of GEMs 9 and 10 are 3.64 and 2.87 respectively. This is almost a 39% difference in the energy read out using the same radioactive source on the same relative areas of the GEM detectors. The Y readout has an even larger discrepancy with the average energy of GEM 9 of 3.31 and GEM 10 of 2.26, yielding almost a 53% difference. The only explanation available for such a large difference in the gains of these two detectors must come from the GEM foils, either in the quality of the foils themselves or a problem that arose from the stretching and framing process.

Every GEM foil was tested at 500 V for leakage current before and after the framing process, as discussed in section 2.3.2, and every foil passed both times. Figure 2.7 shows a table of the leakage currents recorded in those tests. However, there were a couple of foils that had slightly higher levels of leakage current than the others that did not pass on the first testing. These foils had to be brought up to the desired voltage slower than the others in order to burn off impurities. There were no further problems in the testing after these impurities had been burned off and the GEM foils were able to hold 500 V with less than 5 nA of leakage current, which allowed us to go ahead and build them into a detector. If this were to cause a problem in the GEM detector we would expect it to be in the form of sparking, rather than non-uniformity.

Pictures from the stretching process were reviewed after the testing of GEM 10 revealed a large issue in the bottom left corner. In one of these pictures, shown in figure 3.27, small amounts of wrinkling were noted on one of the GEM foils. It cannot be determined after that fact whether these small wrinkles are actually present in the GEM foil or if they are a product of the way the foil was being held

when the photo was taken. Nor is it known that this foil was constructed into the GEM 10 detector, as its identification number cannot be seen in the photo. Each of the GEM foils were visually inspected and any wrinkling would have been noted if it had been seen before the GEM foils were permanently glued together.

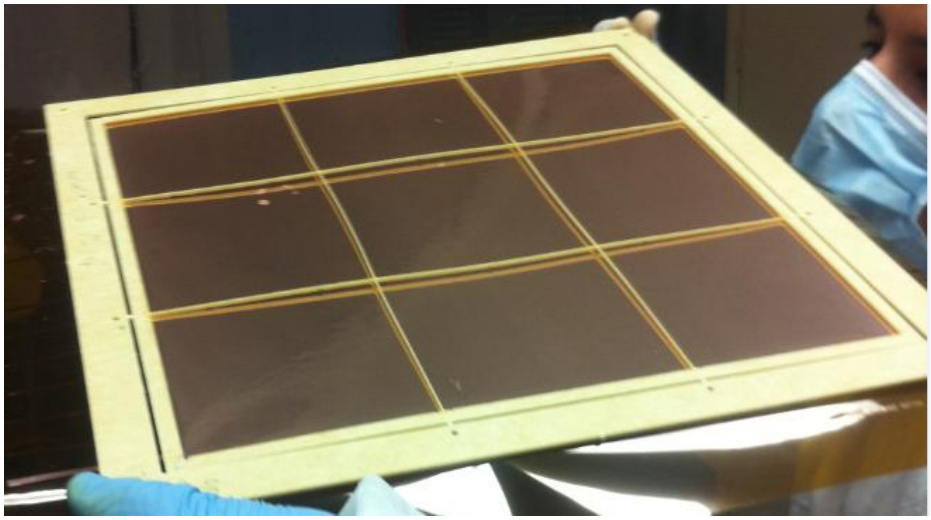

Figure 3.27: GEM foil with evidence of some wrinkling in the bottom left corner, which may help explain the problem area in GEM 10.

3.4.3 Cosmic Muon Measurements

Our GEM detectors were originally built to track paths of cosmically generated muons. This is a tested field in which the application of GEM detectors is already a known value. It makes sense that we would test our GEM detectors for uniformity in the detection of these muons.

There is a relatively constant muon flux everywhere on the planet because muons are constantly being generated by cosmic rays interacting in our atmosphere. It is impossible to test our GEM detectors for uniformity with muons in the same manner used with the radioactive sources because muons are a

minimum interacting particle and can pass through very large quantities of material without being absorbed. Instead we settled on collecting data for each connector. Originally we had our readout connector wired to read all 128 strips of a Panasonic connector, of which there are 12 on each GEM detector. This allowed us to effectively test the entire active area of the GEM detector using the muon flux. The rate of this collection combined with the area of a single readout set could then be compared to the expected rate of 1 $cm^{-2}min^{-1}$. Each of these runs were taken over night even with the entire Panasonic connector being read out in order to obtain a sufficient number of data points to be considered a high-statistics run.

We discovered that this wire connecting all of the pins of the connector was a very large source of noise well after we had tested each of the connectors on both GEM detectors. This was a major setback because first tests after the removal of the wire showed that our data collected was indeed noise dominated and could not be used. We were also pushed up against a deadline of the GEM detectors being sent to CERN in Geneva for testing in the project they were originally constructed for and had to re-run all of our data collections. Re-runs using the radioactive sources took precedent over the cosmic data, so we were unable to retest all 24 channels with cosmic ray muons. On top of this setback, we were now working with 1/16 of the active area of our readout board. We cannot compare the data collection rates from our original tests to the new, and proper, tests due to the impact of the noise, but this did significantly reduce the readout capabilities.

We were able to perform much more extensive testing on GEM 9 than we were with GEM 10 due to the time constraints in sending out GEM detectors to CERN. Tests performed on GEM 9 included overnight data collections at our operational voltage of 4100 V for the detection of cosmic muons on half of our connectors, as well as a plateauing test to confirm we were working at the

appropriate voltage to begin with. The plateauing test involved the use of two of our smallest scintillator paddles turned on their sides with one positioned directly above and below the active area of the GEM detector we were reading. The acquisition card connected to the scintillators was then set up to provide an external trigger to the oscilloscope whenever a coincidence was detected in the two scintillators. Data was then collected at different operation voltages in order to show which voltage would be ideal for the detection of muons. This was not a perfect test because the scintillators used were 1 cm wide and 10 cm long. This is approximately 3 times too wide and 1/3 the length for the active area we were able to read. Each of these collections took more than 50 hours and two of them had to be rerun due to electrical glitches ruining the data sets. With these limitations we were only able to obtain six data points to plot, four of which were usable.

Each run collected 5000 data points, but we did not expect all of these to be real muon detections both because of the size discrepancies in the scintillators and the active area of the GEM detector as well as the lower operation voltage in some of our runs. Analysis of this plateauing procedure started with plotting a histogram of the charges detected in the run. A Gaussian curve was then fit to the only peak which was located at very low energy levels. This peak is generated from the random noise and background of the GEM detector when a muon triggered both scintillators but was not read in our active area. The fit to this peak gave us both the mean value as well as its standard deviation. Charge levels read higher than the mean value plus three times the standard deviation are more than 99% likely to be outside the noise, and thus actual detections of muons. This minimum value was then used as a cut in each of our runs and the number of actual muons detected was found and plotted against the high voltage applied to the detector.

The plot shown in figure 3.28 clearly shows an increasing trend in the number of fraction of muons detected by the GEM detector as the high voltage is increased from 3800 to 4000 V. It then levels off from 4000 to 4100 V. The leveling off is the plateau we are looking for in the plot, and it tells us these levels are the best to operate under for optimum response in the GEM detectors. Similar tests have been performed by other groups in the past, which is why we have known to operate around 4000 to 4100 V in our GEM detectors all along. This test was done as a confirmation that GEMs 9 and 10 were working at the same conditions of the GEM detectors already constructed using more conventional means.

The overnight data collections taken on both GEM 9 and GEM 10 provided very similar plots, regardless of the connectors tested. Each detector showed its own characteristic histograms, as seen in figures 3.29 and 3.30, plotted from these data sets with an evident charge peak. Landau curves were fit to each of the histograms with low sigma. The average charge peak collected on GEM 9 was 0.46 V*μs, with an average collection rate of 0.30 Hz. Histograms of data collected with GEM 10 had an average charge peak at 0.21 V*μs, with an average collection rate of 0.33 Hz. The charge peak for GEM 9 is more than double the charge peak for GEM 10. GEM 9 having a higher charge peak is consistent with the X-ray source data, but not quite to this extent.

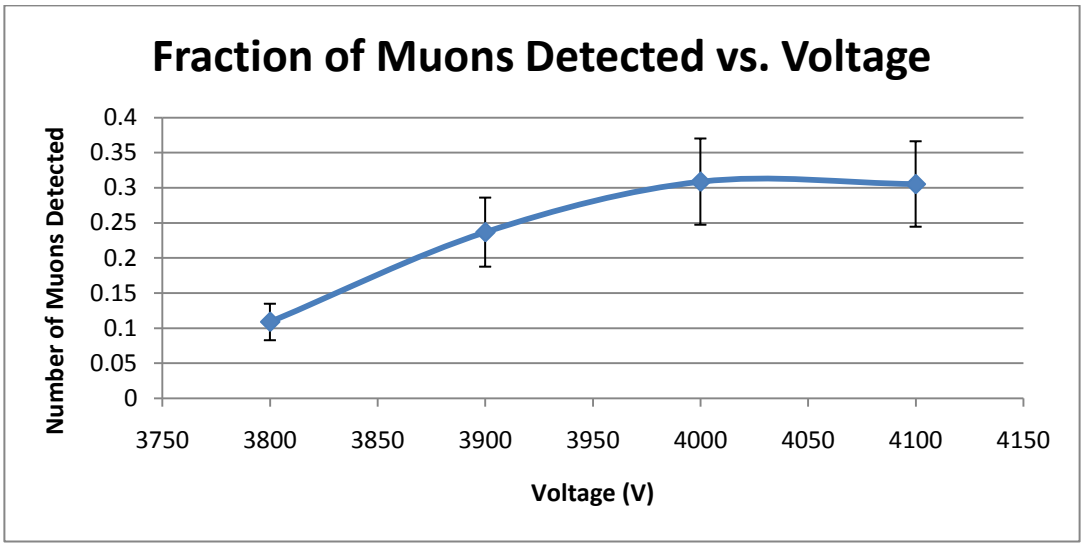

Figure 3.28: Fraction of muons detected triggered by two scintillator coincidence trigger vs. high voltage applied to the GEM 9 detector.

There are only 8 active strips in these cosmic ray muon collections, yielding an active area 0.3125 cm wide and 30 cm long. Considering the random path nature for electrons moving through the gas and the spread of an electron cloud when the avalanche occurs, we can expect to receive signals for muons that pass through the nearby strips as well, yielding an active strip closer to 0.5 cm wide and 30 cm long. With this information, along with the average collection rates, the average muon flux detected was calculated to be 1.27 $cm^{-2}min^{-1}$, which is a bit higher than the accepted 1 $cm^{-2}min^{-1}$, but does fall within statistical error, especially with the assumption about the width of the readout area.

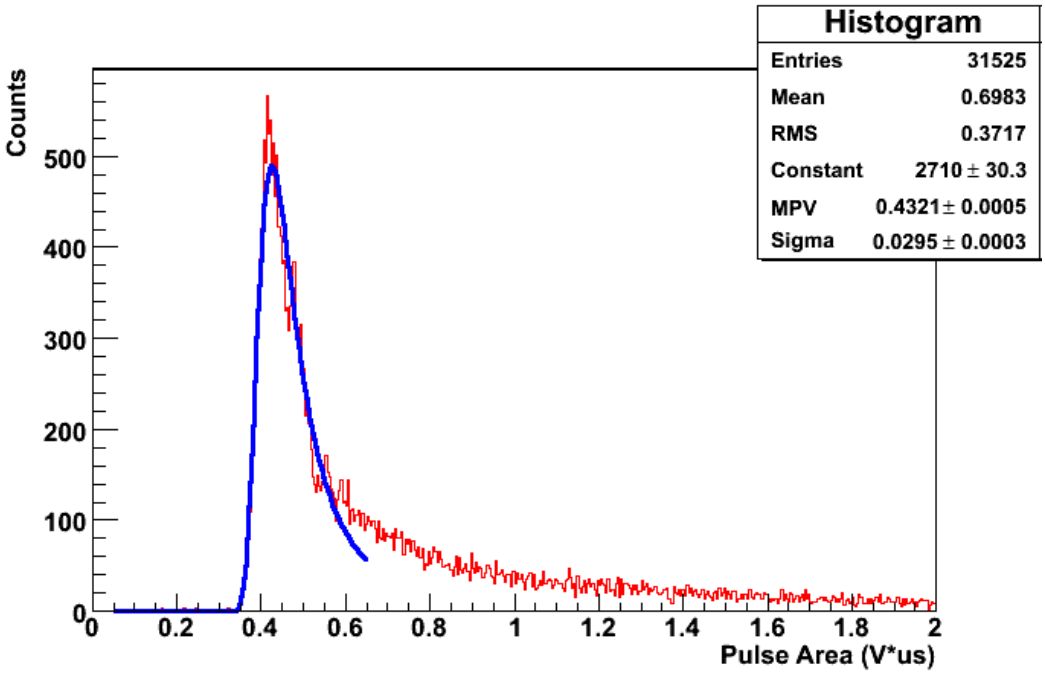

Figure 3.29: Characteristic histogram of cosmic ray muon data collected with GEM 9 fit with a Landau curve to the charge peak.

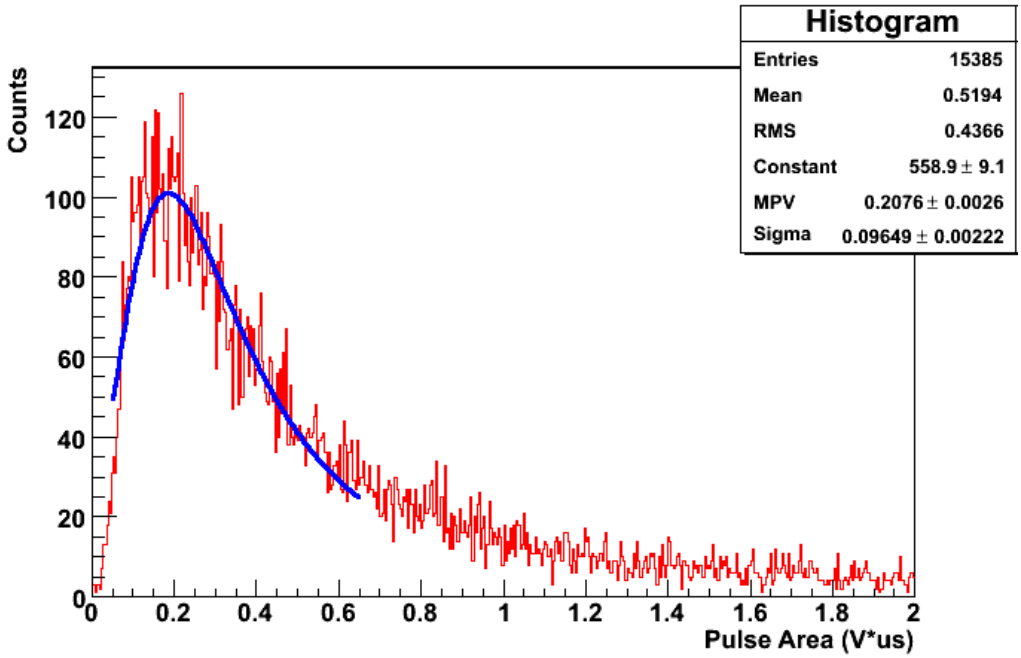

Figure 3.30: Characteristic histogram of cosmic ray muon data collected with GEM 10 fit with a Landau curve to the charge peak.

Chapter 4 Coded Aperture Mask

4.1 Concept

The penetrating capability of X-rays is simultaneously an advantage, giving us a glimpse at the "high energy" universe, and a disadvantage in astronomical observations. The greatest advantage is that these X-rays, when observed, allow us to look deeper into regions of space where other readable radiation energetic charged particles are more completely absorbed. A major disadvantage to these X-rays is that they are difficult to focus in our detectors using optical means. Mirrors and other focusing techniques can be used to focus radiation of longer wavelength and lower energy, but X-rays have a tendency to pass straight through these optical devices unhindered. There is also an issue with losing X-rays in the much stronger background radiation due to their lower flux from cosmic sources if the detector used is sensitive to more than just the X-ray band of interest.

The sensitivity of GEM detectors in the X-ray energy range has already been discussed at length, especially with the use of X-ray sources to test the uniformity of each GEM detector we constructed. GEM detectors are also sensitive to fast moving charged particles, but they are not sensitive to lower energy photons because of the structure of its frame. About 95% of lower energy radiation ($E < 5$ keV) is absorbed in this structure, while higher energy radiation ($E > 15$ keV) passes through the entire detector undetected. If we exchanged the top structure with a sheet of Mylar, which we have tested on our 10 cm 10 cm GEM Detectors, the lower-energy sensitivity can be improved to include softer X-rays and still exclude other unwanted radiation in the optical and UV bands. Exchanging the argon gas in the detector for a heavier gas like xenon would also

increase the higher energy limit from 15 keV closer to 100 keV. This gives GEM detectors an interesting window of energy sensitivity to be used in X-ray astronomy.

According to NASA's High Energy Astrophysics Science Archive Research Center [19] there should be more than one million known X-ray sources of interest to astronomers as of 2010. This number is dramatically increased from a single source in the early 1960 when this field was getting started. For a more modern comparison, this number is nearly double the 550,000 known sources in 2007, which is more than double the 220,000 known in 2005. These sources include objects such as active galactic nuclei, supernovae, binary stars, and many other interesting topics of research to astronomers today. Technology is racing to keep up with the field of X-ray astronomy growing at such a rapid pace, making any improvements to previous detectors an important step forward.

There have been many techniques researched and developed to improve the resolution capabilities of X-Ray astronomy, including the coded aperture mask. A coded aperture mask is an array of opaque and empty cells, usually square shaped, made from a higher-density material such as Tungsten [13]. Coded aperture masks find their origins in pinhole camera. The small hole size of a pinhole provides increased angular resolution, but at the same time decreases the sensitivity of the instrument by greatly decreasing the flux of X-rays incident upon the detector. Thus, the hole size provides a tradeoff between angular resolution and detector sensitivity. This compromise is also present in the use of a coded aperture mask. The angular resolution for the coded aperture mask and detector combination is given by a simple equation [13].

Where: -$\delta\theta$ is the angular resolution

-m is the mask hole size

-l is the distance between the mask and the detector

-d is the position sensitivity of the detector

The opaque cells in a coded aperture mask are made sufficiently thick to block incident X-rays and leave a shadow on a position-sensitive detector, such as a GEM detector, behind the mask. The shadow pattern created by a single point source is simply a recreation of the same pattern of opaque cells from the mask projected onto the detector, referred to as a shadowgram [13]. Figure 4.1 shows a coded aperture mask projecting its shadowgram onto the detector behind it. Hole patterns in the top left of the mask can be matched directly to the patterns shown on the detector [18].

Any complex source can be broken down into a combination of many point sources. As such, any shadowgram created on the position-sensitive detector is a combination of the same mask pattern projected at different angles. Figure 4.2 shows two point sources tracked through a coded aperture mask with their respective shadowgrams overlapping on the detector. This combined pattern does lead to some distinct issues when working with a coded aperture mask. Each part of the mask involved in creating a shadow pattern from a distinct source is referred to as a "working zone" [13]. Each source generally requires its own working zone in the projection of this pattern in order for full reconstruction to be possible. This does not mean each individual source has to project through its own distinct empty cells. It does, however, mean that too much overlap from multiple patterns can degrade the signal quality in reconstruction.

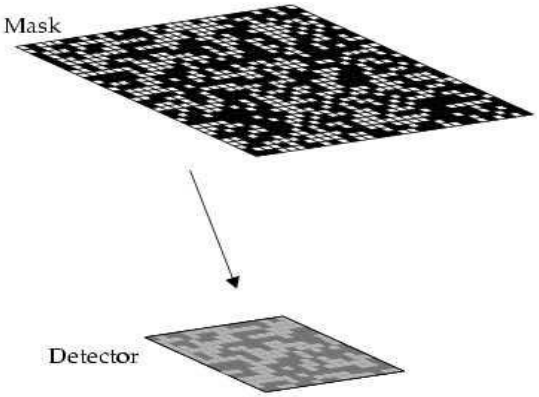

Figure 4.1: Diagram of a coded aperture mask above a position sensitive detector, showing the shadowgram projected by the mask [15].

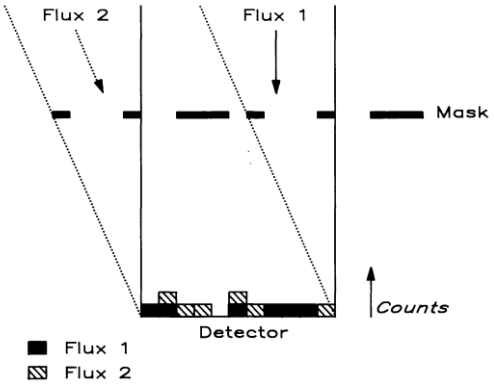

Figure 4.2: A diagram of two far away point sources projecting a shadow of the mask pattern onto the position-sensitive detector from different angles [13].

Anther concern for the coded aperture mask and detector array is the effective field of view of the instrument. There are two distinct fields of view to be considered, and those are the Fully Coded Field of View (FCFV) and the Partially Coded Field of View (PCVW). The Fully Coded Field of View is the region where all detected photons must pass through the coded mask before reaching the detector, while the Partially Coded Field of View allows some fraction of the detected photons to pass by the edges of the coded mask [13]. Figure 4.3 shows how the FCFV and PCFV are determined for a coded aperture mask and detector by connecting straight lines from near and far edges of the mask and detector respectively.

It is always best to try to keep any source you wish to image in the Fully Coded Field of View with a coded aperture mask instrument. Signal degradation can occur if too many photons can enter through the Partially Coded Field of View and wash out the shadowgram left by the fully covered area.

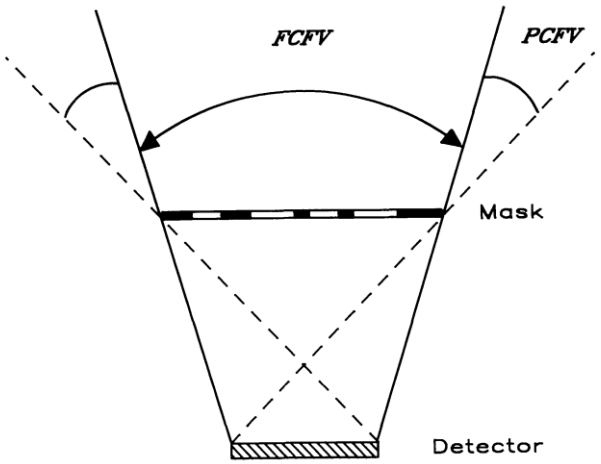

Figure 4.3: Diagram of a coded aperture mask and detector showing both the Fully Coded Field of View and the Partially Coded Field of View [13].

There are three possible geometries for the coded mask and detector arrangement. The first geometry is the simplest, with both the detector and the mask being the same size. This geometry is a bit limiting because the only FCFV is directly on axis with the instrument [20]. It does, however, provide excellent position resolution and a high signal to noise ratio for imaging on that primary axis. The second geometry has a much wider FCFV with the mask being larger than the detector. Masks are typically twice the size of the detector in this geometry in order to provide a large FCFV without cutting the signal to noise ratio down by too much. The final geometry is the reverse of the second with the detector larger than the mask. This provides an equivalent field of view to the second geometry and improved SNR as long as the PCFV is shielded to prevent washing out, but is not widely used primarily because position sensitive detectors are much more difficult and expensive to manufacture than the coded aperture mask [13].

4.2 Imaging with a Coded Aperture Mask

The reconstruction of an image from a coded aperture mask first involves a point spread function, A(x,y), for the aperture transmission. This is a function for which cells in the coded aperture mask are opaque or transparent. An object distribution function, S(x,y), which is a two dimensional point spread function of the object being imaged, is also required. The z axis is unimportant for astronomical imaging, and thus not included in either of these functions because the detector is only capable of two-dimensional analysis, in x and y, and because with the great distance involved in astronomical observations the z term for the source spread function typically doesn't matter. These two spread functions, combined with a term B(x,y) for the signal independent noise of the mask and detector, gives us the spatial distribution of the detected flux, D(x,y) [13]:

In this equation the * represents the convolution operator. This spatial distribution can then be multiplied by a decoding function G(x,y) specific to the coded aperture mask to obtain a better estimate of the object spread, .

For a much more in-depth explanation on analyzing the point spread functions of the source and the mask, as well as an analysis for obtaining the final image please see E. Caroli et al. [13].

The quality of the image received after analysis is highly dependent on the coded aperture mask itself as well as the decoding function used. As such, there

has been a lot of research and testing on which types of coded aperture masks work best. Original coded aperture masks were constructed using random filling of some percentage of cells in the mask; usually 50%. This process, however, cannot be completely random because any filled cell must border at least one other filled cell in order to actually hold its position. We cannot have filled cells floating in the middle of empty ones unless the transparent cells were to be filled with some other low-density material.

The random nature of this type of mask allows for easier identifying of patterns in the shadowgram imaged on the detector, but is much harder to analyze with a point spread function. Uniformly redundant arrays (URA's) are coded aperture masks whose open cells are placed in a regular rectangular or hexagonal pattern according to an algorithm. This allows for a much easier point spread function of the mask and the redundant image produced provides a very high SNR after reconstruction [13]. Non-redundant arrays (NRA's) are a subset of URA's which have no redundancy in their hole pattern. The vector spacing between any two transparent cells in an NRA is unique, making reconstruction much more precise. NRA's provide much more ideal imaging properties with a major drawback in sensitivity. The number of transparent cells is very limited in order to achieve the non-redundant hole pattern, as only around 10% transparency can be achieved with an NRA, and mask shape and size may not always match the desired detector [13].

More recent research suggests using a mask with a predetermined point spread function based on the spread function of the source we wish to image. Masks with a Gaussian distribution of opaque and transparent cells are proposed for this technique. They would provide Gaussian Random Fields (GRF's) in their image pattern, which have homogeneous and isotropic statistical properties. The

properties of the mask can be predetermined for the source. This means the GRF's can provide us with a way to create a coded aperture mask with the predetermined imaging characteristics we desire without as much of a tradeoff as URA's or NRA's in terms of angular resolution and detector sensitivity [21].

4.3 Modeling a Coded Aperture Mask

We used computer simulations in order to test the viability in using a GEM detector with a coded aperture mask for imaging X-ray sources. These simulations were all run with the SWORD program [22] developed by the Radiation Safety Information Computational Center around the Geant4 simulation toolkit. It was not possible to simulate the actual X and Y plane readout strips of the GEM detectors we are currently working with in this programming language. The detector is constructed as a pixel detector instead, having pixels the size of the position resolution we are capable of reaching with our GEM detectors.

The first step in working with these models was to construct the GEM detector. Rather than building the entire structure of the detector, which would take extra computing time to compile in each of the runs, I settled for making the detector a pure argon volume. This is not too far off from using a true GEM detector because the structure of the detector should be fairly transparent at the energies we wish to detect and the argon in the drift region is where our incident X-rays are going to interact to start the electron avalanche that will become our detected signal. The first step was to run a few preliminary test models to see if an argon volume would work. These test runs did show that this form of detector could work and the best energy photons to test it with were 6 keV X-rays. However, calculations made after the first few runs showed an efficiency of only

10% with the argon volume detector. For this reason a NaI detector volume was used in subsequent runs, as it had over 80% efficiency in the program.

Constructing the detector was the next step in the modeling. This was done by first making a single cell, or pixel, of the detector and defining its size and energy resolution. We used an energy resolution of 13% at 10 keV in our model, while the size of the cell varied in different runs. The first iteration of this model used square cells that were 400 μm across and 3 mm deep. These dimensions match the pitch of our readout strips and the depth of the drift region for our GEM detectors. The actual position resolution for our GEM detector is closer to 130 μm, but we felt it best to start with the larger cells mostly because of the increased amount of time each simulation takes when working with smaller cells. Once the first cell is created and defined as a detector element it can then be made into a large array of cells to form one large, position sensitive detector. This same process was used for both the argon and NaI detectors. In this way the efficiency of the NaI detector could be used to obtain higher statistic runs while still having the same detector characteristics as the actual GEM detector we were attempting to model.

Constructing the coded aperture mask was done in a fashion similar to that of the detector. First a single 2mm square cell 7 mm deep was constructed out of lead. These dimensions were chosen because they seem to be a fairly standard size for coded aperture mask cells [15]. This first cell is then made into a full coded aperture mask by selecting how many cells the mask will have on each side and the percent of these cells that to be opaque. All mask patterns used in these simulations were with randomly generated opaque and transparent cells. The SWORD program only allowed for changes in cell spacing, which was set to zero

so there was no excess material between mask cells, and the percent of the mask to be made opaque.

Constructing the mask proved to be a major source of errors in early iterations of the models. While the actual error involved in the program remains unclear, it was related to the relative size and number of pixels between the coded mask and the detector used. Once the mask is completed it is then moved to the desired location in front of the detector, which was left at the origin of the model for simplicity. Finally, the mask and detector are established as a single instrument for analysis purposes, and the coded aperture mask telescope is completed.

The last thing each of these models required was one or more X-ray sources to be imaged placed within the FCFV some distance away from the mask and detector. Different versions of the model used different sources, ranging from single point emissions to larger spheres, as well as line sources. Glass objects of the desired size and dimension were used for this. Glass was chosen because it is very transparent to most wavelengths of radiation and would not interfere with the projected photons. The glass object was then defined as a surface generating radioactive source with the "test gun" feature to fire photons of the desired 6 keV energy. Small glass spheres were used as point sources, while larger spheres and cylinders and boxes were used for the extended objects and line sources to be imaged.

4.4 Results

In each run the total area of the detector is set to be 5 cm 5 cm. This is much less active area than our actual GEM detectors, but the number of pixels that would be needed for a 30 cm 30 cm detector made each run prohibitively long,

thus the detector had to be scaled down. The coded aperture mask used in each of the models is 15 cm 15 cm, 7 mm thick, and has 2 mm 2 mm cells. This is larger than the originally desired 10 cm 10 cm mask (twice the size of the detector) due to some error in the SWORD program that would not allow for a smaller mask. Most runs have a 10 cm distance between the detector and the mask. In some instances the distance was increased to 20 cm or 30 cm in an attempt to increase the angular resolution of the instrument. The thickness of the coded aperture mask versus the width of each cell can cause auto-collimation in the signal [15], as demonstrated by figure 4.4, blocking X-rays outside an allowable incident angle (θ) given by the equation:

$$\theta = \tan^{-1}\left(\frac{m}{t}\right)$$

Where m is again the width of the mask cells and t is the thickness of the mask. Our models had an allowed angle of almost 16 degrees before auto-collimation became an issue, and none of the sources used for imaging exceeding this field of view, thus this problem never came up.

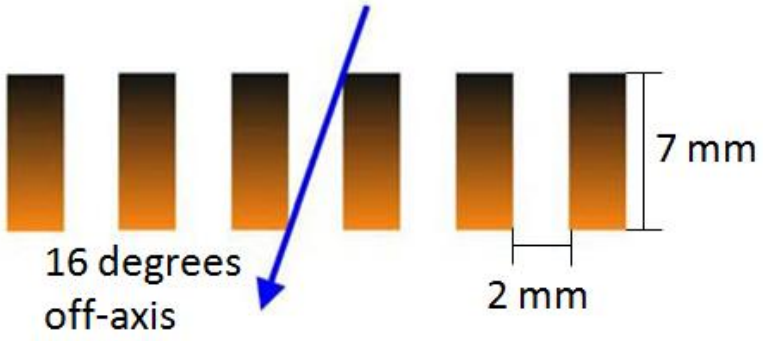

Figure 4.4: Side view of a set of opaque and transparent coded aperture mask cells showing the cell width, mask thickness, and auto-collimation angle of the mask [15].

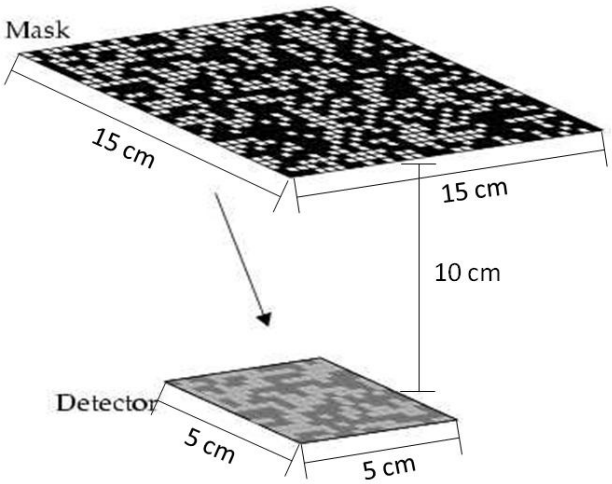

Figure 4.5: Diagram of the typical coded aperture mask and detector setup used in the SWORD [22] models. Mask dimensions are 15 cm 15 cm 0.7 cm, with cell of dimension 2 cm 2 cm. Detector dimensions are 5 cm 5 cm 0.3 cm with pixels of dimension 0.04 cm 0.04 cm or 0.013 cm 0.013 cm. The mask depicted in this diagram is not the actual configuration of the mask used in the models [15].

The simplest form of imaging modeled was with a single radioactive point source. It did not matter if the point source was used to emit a single energy photon or a full spectrum, but analysis was quicker for the single energy runs. This point source is placed a large distance away from the mask and detector instrument, then has an emission direction defined. This emission direction is why the distance between the source and the detector is our limiting factor. The GEANT4 process for a radiation source emits the radiation randomly in all directions. The emission direction defined on the source only tells the program which photons to log for analysis. For example, we placed the point source 10 m away from the detector. At this distance approximately 2×10^{-4}% of the radiation flux from the point source will pass through the active area of the 5 cm 5 cm detector.

Each run taken for analysis was done by generating 10^9 photons, of which 2000 should have passed through the mask and detector and only around 100 actually interacted in the argon volume. The expected flux should have been around 1000, as our masks with the single point source have 50% opaque cells. This does not necessarily guarantee that 50% of the area through which the radiation actually passed through was opaque or transparent, but the variation in this does not account for only having 10% efficiency in the detector. Use of the NaI detector however allowed us to read between 800 and 950 photon in the same situation, which is why the model was changed.

Successful reconstructions with the point source were achieved using both the NaI and argon detectors despite the lower efficiency in the latter. An image using the single point source and argon detector is shown in figure 4.6 with a signal to noise ratio of 1.8. The reconstruction algorithm used by the SWORD program is not available to anyone not on the development group, thus I cannot elaborate on the functions used to create the images from the shadowgram. Even the original shadowgram of the detector is unavailable for the models. The results for the single point source were retested both with the source at the same location as the previous model as well as moved around the x and y plane to ensure the reconstruction was actually imaging the source and not coincidently placing it in the proper location. Each of these runs was successful in reconstructing the correct x and y positions of the point source. These would be considered very low statistic analyses which are very prone to being noise dominated, yet they were still successful in imaging our source.

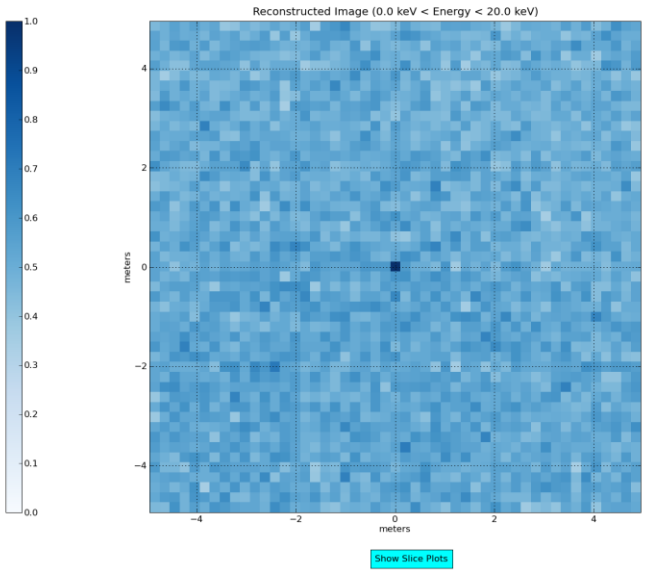

Figure 4.6: Reconstructed image of a single point source using a 5cm 5cm argon detector volume with 400 um cells and a 15cm 15cm lead coded aperture mask with 2mm 2mm cells. This image was reconstructed with approximately 100 photons detected.

Each reconstructed model is shown as an x-y image as well as in two slice plots, like the ones seen in figures 4.6 and 4.7 respectively. The image is what is obtained after the reconstruction algorithm built into the SWORD program [22] is run on the shadowgram. Each cell is then normalized based on the intensity of the source it should contain based on this reconstrction. Darker cells in this model represent higher correlation to the source location, whereas lighter cells represent little to no source present. The locations displayed on the cut plots can be chosen with a sliding line to show numerical values for any locations in the image. A rough estimate for the signal to noise ratio of the image can then be obtained by averaging the numbers for cells with the desired signal and the noise in all the other surrounding cells. The noise in this image is entire due to the image reconstruction, as there are no background sources in the model.

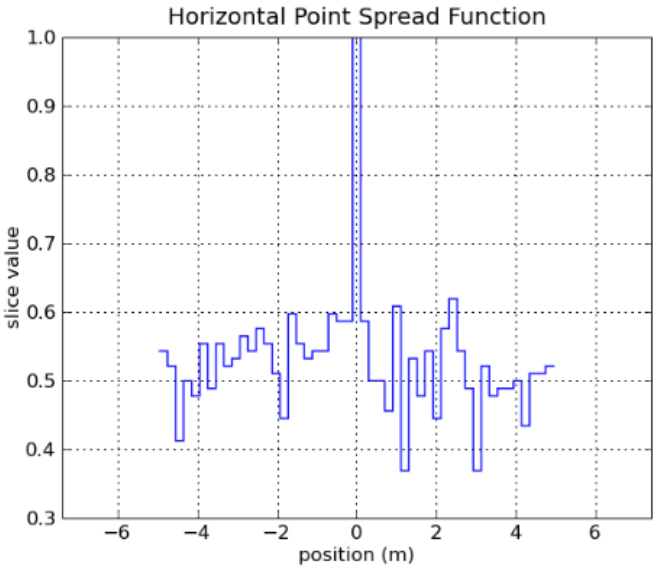

Figure 4.7: Horizontal slice plot of the point spread function of the image in figure 4.6 with the point source evident at the center. This slice gives signal to noise ratio of around 1.8.

Models using two point sources between one and three meters apart were also successfully reconstructed with SNR a bit lower than was achieved for the single point source models. One such model with the two sources spaced 2.25 m apart had a SNR of 1.4 for one source and 1.3 for the other, but the X-ray sources were clearly defined and in the correct locations in the image. Reconstruction was also successful for three point sources, but the SNR was greatly diminished. Two of the sources were clearly defined, but the third was nearly lost in the noise. SNR for these sources were 1.4, 1.3 and just above 1.

Investigation of line sources came after the successful reconstruction of the point source models. These models had much lower SNR, typically around 1.1, than the point source models. Single line reconstructions were still possible, despite the lower SNR. Figure 4.8 shows a single, vertical, 1 m line source successfully imaged. The line was clearly visible and occupying the correct

number of pixels in the image. The vertical slice plot shown in figure 4.9 yields a SNR of 1.1 for this reconstruction. Multiple line source models, however, suffered some losses in the reconstructions. Models of parallel lines would sometimes lose one end of one of the lines in the noise. Reconstructions of intersecting lines would have even lower SNR, between 1 and 1.1, along with clipped off sides of both lines, as seen in figure 4.10.

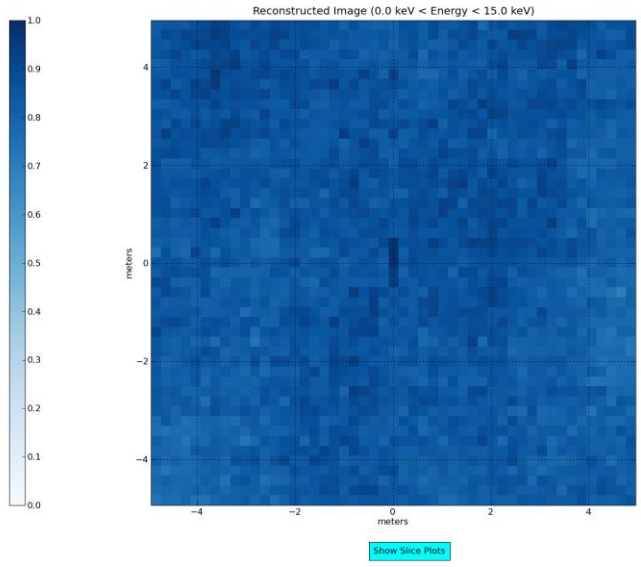

Figure 4.8: Reconstructed image of a single line source with SNR 1.1 using the 5 cm 5 cm NaI detector with 130 um pixels and a 15 cm 15 cm lead coded aperture mask with 2 mm 2 mm cells. The single line source is well defined and properly sized from an analysis with 1100 photons.

The last set of models run comprised larger, more extended objects such as the flat side of a large cylinder or box and large radii spheres. The box and cylinder are much better representations of astronomical objects because the distance from the detector to any point on the object is closer to constant with their flat surfaces. Spheres with radius 0.5 m proved to be very problematic, as the objects were only

10 m from the detector. None of the models using spheres were able to reconstruct any part of the object, which is understandable given larger change in relative distance for the emitting surface.

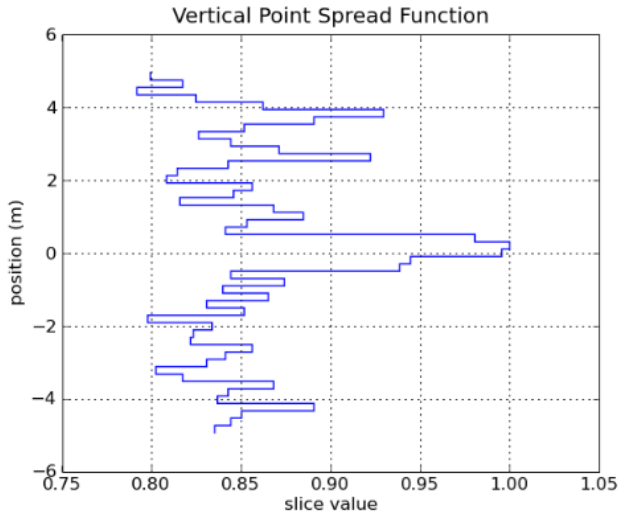

Figure 4.9: Vertical slice of the point spread function through the line source in the image of figure 4.8. This slice gives signal to noise ratio of around 1.1.

Models using the surface of a with box sides less than 0.5 m in length as the X-ray source were successfully reconstructed. Position resolution in the instrument was only 0.2 m for this distance, so the box sides were read at 0.6 m in the image seen in figure 4.11. Reconstruction of images for boxes larger than this all failed, being entirely noise dominated. This is also reasonable, as objects with that much surface area would dominate a large portion of the sky seen by the detector and would probably wash out parts of the shadowgram needed for reconstruction.

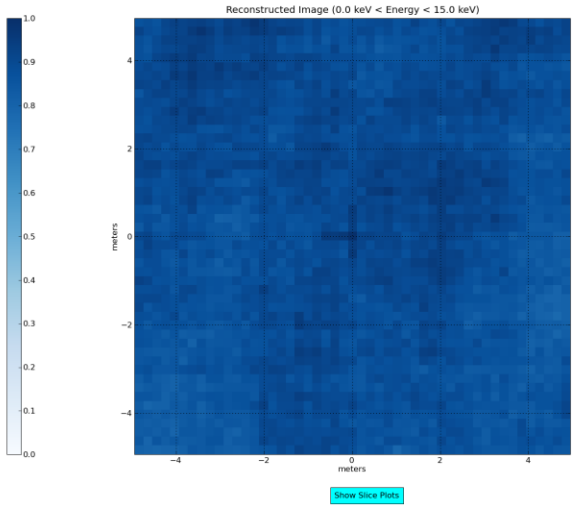

Figure 4.10: Reconstructed image of two crossed line sources using the same detector and coded aperture mask defined in figure 4.8. The cross pattern has lost parts of both lines in the bottom and right sides and has a SNR slightly below 1.1. 3300 photons were detected and used in the reconstruction of this image.

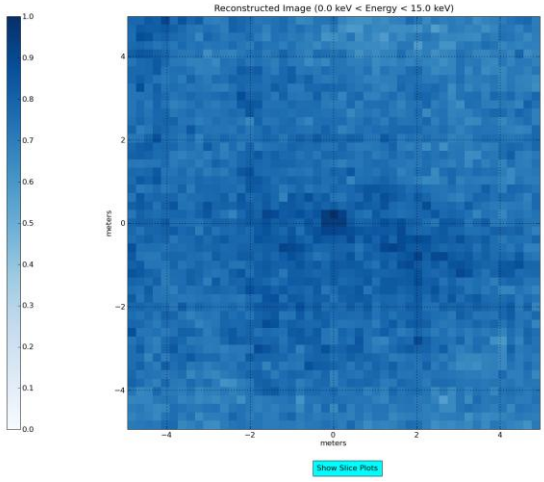

Figure 4.11: Reconstructed image of a box source with 0.5 m long sides using the same detector and coded aperture mask defined in figure 4.8. The top of the box is better defined, but the whole source is visible above the noise with an SNR of 1.2. Approximately 1200 photons were detected and used in the reconstruction of this image.

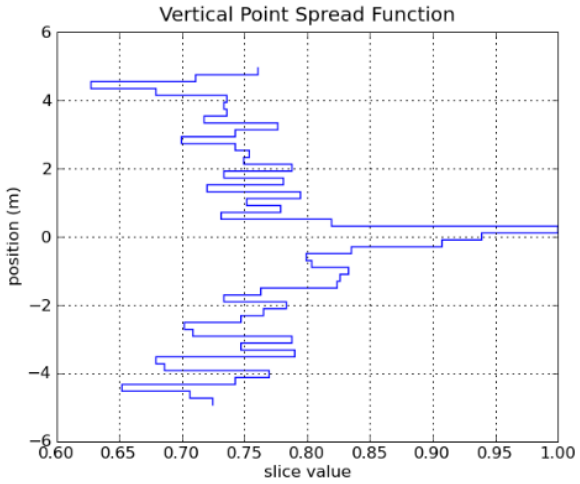

Figure 4.12: Vertical slice plot of the point spread function through the center of the box source in the image of figure 4.11. This slice gives signal to noise ratio of around 1.2.

All models using the flat side of a cylinder were unexpectedly failures. The reconstruction shown in Fig. 4.12 is the best run achieved, and only part of the area of the cylinder is shaded slightly darker than the background. Average SNR for this region is barely above unity, which is why this model is considered a failure. There are several locations on the image that are shaded just as dark as the actual source location, meaning the source was not properly identified by the SWORD reconstruction algorithm [22]. It should be noted for all of the large sources that the number of photons per pixel of the image is much lower than for the models with successful reconstruction. This is due to the method through which GEANT4 and SWORD generated photons from a source. In this program a source generates the determined number of photons symmetrically, only tracking photons which pass through the determined volume. For larger sources this can reduce the number of photons per pixel detected to less than 100, severely reducing the statistics, and thus reconstruction capability, of the model.

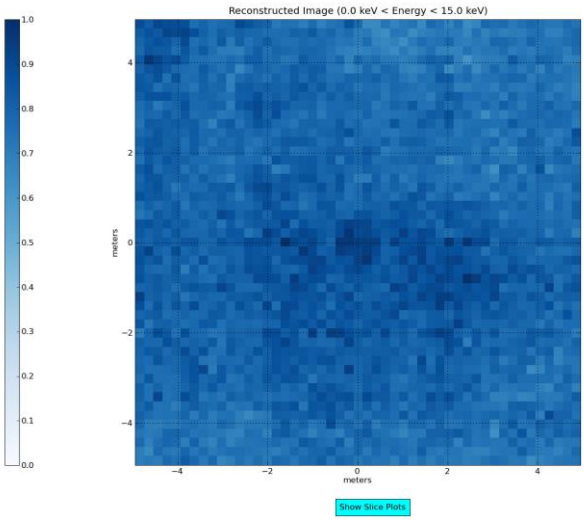

Figure 4.13: Nearly successful reconstruction of the flat side of a cylinder with radius 0.5 m using the same detector and coded aperture mask defined in figure 4.8. 1100 photon were used in this reconstruction, but the SNR barely above 1 so the reconstruction is considered a failure.

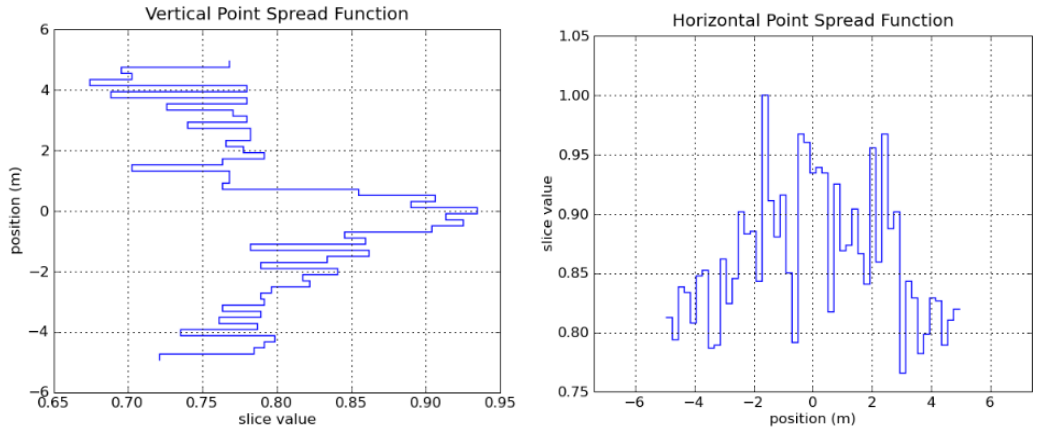

Figure 4.14: Vertical (left) and horizontal (right) slice plots of the point spread function through the center of the cylinder source in the image of figure 4.13. This slice gives signal to noise ratio barely above 1.

Chapter 5 Conclusions and Summary

Two different infrared stretching devices were constructed using the low cost materials easily available from local hardware stores. The stretching devices both involved a hanging rack with multiple 250 Watt infrared light bulbs affixed around the outside edge. This light rack was positioned above acrylic stretching frames, which held a GEM foil tightly between them. These two light racks were tested extensively for their temperature uniformity, which turned out to have a maximum variation of six degrees Celsius, and stretching capabilities. The smaller light rack and acrylic stretching frames were successfully used to stretch and frame six 30 cm 30 cm GEM foils, which were then constructed into two fully operational GEM detectors. The larger light rack was used to successfully stretch a large CMS test GEM drift foil. The success of these tests and the successful stretching of the GEM foils shows the IR stretching rack to be a viable technique. It is cost efficient, saves space, and successfully stretches GEM foils to the required tension for use in a GEM detector.

The two 30 cm 30 cm triple GEM detectors constructed using our IR stretching technique were extensively tested for their gain uniformity with the use of multiple radioactive X-ray sources. There was a lot of noise hunting and canceling involved in this procedure in order to validate our results, which lead to the repeating of our measurements multiple times. We found the 5.9 keV soft X-ray generated by the Fe-55 to be 95% absorbed by the fiberglass structure of the top of or GEM detector frame. We also found the use of a Cd-109 source emitting 22 keV X-rays to be the most effective source for timely and high-statistics data collections.

The use of the 22 keV X-rays from the Cd-109 source produced an unexpected side effect in the GEM detectors in the form of photoluminescence from copper GEM foils. This meant that all of our tests were actually done with a collection of two unresolved copper emissions at 8 keV and 8.9 keV averaging into a single peak around 8.5 keV. The gain uniformity tests of the GEM detectors was not invalidated by this unexpected effect because these copper X-rays were most likely generated in the drift foils at the top of the detector and subsequently interacted with the argon in the drift region to create an electron avalanche. This is the same process through which any X-ray would be detected, thus did not adversely affect the Gain of the detector. This effect was tested and confirmed with long, integrated data collection using the lower energy X-rays from the Fe-55 source.

Gain uniformity tests for both GEM detectors provided mixed results. GEM 9 had a very uniform photopeak location for almost all the 36 locations tested for the X readout, yielding a maximum variation of -18% in one of the corners. The Y readout, however, was very non-uniform had several locations that failed to provide a resolvable photopeak entirely. Uniformity tests for both the X and Y readouts of GEM 10 were neither as good as the X readout of GEM 9 nor as bad as the Y readout of GEM 9. There was an issue with the bottom left corner of both the X and Y readout for GEM 10 failing to provide a resolvable photopeak. Aside from this, and a trend for slightly lower than average photopeak locations around the problem area, the gain for GEM 10 was fairly uniform.

Research into the possible uses for GEM detector in astronomy showed the use of coded aperture masks with GEM detectors to be a promising field of study. Coded aperture masks are used for higher resolution imaging in the X-ray band and rely more on the position resolution of a detector than the energy resolution

capabilities. GEM detectors do have an increased time and position sensitivity compared to conventional detectors such as CCD's used with coded aperture masks. The issue of photoluminescence from the copper drift foil is a major issue for energy sensitivity, as well as the fiberglass top structure we used in our detectors. This structure issue can be remedied by using a thinner Mylar top, which was tested and proven to work on the smaller 10 cm 10 cm GEM detector.

The capabilities of a GEM detector used with a coded aperture mask were tested with computer simulations using the SWORD program with mixed, yet promising results. The models show a capability to image point sources in the FCFV with a high degree of accuracy, even with a low number of photons read by the detector. Many models were run with one, two, and three point sources in the detectors FCFV, and all of these models provided a successfully reconstructed image of the point sources in exactly the correct positions. Signal to noise ratio for these point source models ranged from 1.8 for the single source to 1.4 for the double source and 1.3 for the triple source.

Successful images were also reconstructed using longer line sources and extended box sources. These models reconstructed the single line source with the correct length and in the correct location with an average SNR around 1.1. The imaging of multiple line sources or much larger, sources such as spheres, cylinders, and larger boxes, were not as successful as expected. Use of two line sources did provide successfully reconstructed images with SNR slightly below that of a single line source, but models using three or more line sources became entirely noise dominated. Box sources with sides 0.5 m long were also successfully modeled, but models using a large cylinder or larger box source also became noise dominated and failed to reconstruct the image.

References

[1] F. Sauli, “Principles of Operation of Multiwires Proportional and Drift Chambers,” Lectures given in the academic training program of CERN, 1977.

[2] K. Nakamura *et al.* (Particle Data Group), “Review of Particle Physics,” Physics Letters B, vol. 667, issue 1-5, p. 1-6, 2008.

[3] S. Tavernier, “Experimental Techniques in Nuclear and Particle Physics,” Berlin: Springer, 2010.

[4] D. Ter Haar, “Collected Papers of L. D. Landau. First ed. New York: Gordon and Breach,” Science Publishers Inc., 1965.

[5] A. Quintero, “Construction and Performance of Gas Electron Multiplier Detectors for Nuclear Contraband Detection Using Muon Tomography,” Thesis. Florida Institute of Technology, 2010

[6] F. Murtas, “Development of a gaseous detector based on Gas Electron Multiplier (GEM) Technology,” http://www.lnf.infn.it/seminars/talks/murtas_28_ 11_02.pdf, 2002.

[7] A. Mooradian, “Photoluminescence of Metals,” Phys. Rev. Letters, vol. 22, p. 185-187, 1969.

[8] J. Conolly, “Generation of X-Rays,” http://www-outreach.phy.cam.ac.uk/camp hy/xraydiffraction/xraydiffraction_index.htm, 2007.

[9] “Characteristic X-Rays of Copper,” Phywe Series of Publications, 2001.

[10] CERN Gas Detectors Development (GDD) web page: http://gdd.web.cern.ch/GDD, 2011.

[11] M. Titov, “New Developments and Future Perspectives of Gaseous Detectors,” Nucl. Instr. and Meth. A, vol. 581, p. 25-37, 2008.

[12] F. Murtas, “Development of a gaseous detector based on Gas Electron Multiplier (GEM) Technology,” http://www.lnf.infn.it/seminars/talks/murtas_28_11_02.pdf, 2002.

[13] E. Caroli, J. Stephen, G. di Cocco, L. Natalucci, A. Spizzichino, “Coded Aperture Imaging in X- and Gamma-Ray Astronomy,” Space Science Reviews, vol. 45, p. 349-403, 1987.

[14] D. Abbaneo et al., “Construction of the First Full-Size GEM-Based Prototype for the CMS High-η Muon System,” Proc. IEEE Nucl. Sci. Symp., 2010.

[15] J. Grindlay, J. Hong, “Optimizing Wide-Field Coded Aperture Imaging: Radial Mask Holes and Scanning,” Proc. SPIE 5168, 402 (2004); doi:10.1117/12.506260.

[16] M. Alfonsi et al., “Activity of CERN and LNF Groups on Large Area GEM Detectors,” Nucl. Instr. and Meth. A, vol. 617, p. 151-154, 2010.

[17] M. Staib, B. Benson, K. Gnanvo, M. Hohlmann, A. Quintero, "Thermal Stretching of Large-Area GEM Foils Using an Infrared Heating Method," RD51 Note 004, 2011.

[18] D. Abaneo et al., "Characterization of GEM Detectors for Application in the CMS Muon Detection System," RD51 Note 005, 2010.

[19] S. Drake, "How Many Known X-Ray (and Other) Sources Are There?," http://heasarc.gsfc.nasa.gov/docs/heasarc/headates/how_many_xray.html, 2007.

[20] G. Skinner, "The Sensitivity of Coded Mask Telescopes," Applied Optics IP, vol. 47, p.2739-2749, 2008.

[21] B. Schafer, "Coded Mask Imaging of Extended Sources With Gaussian Random Fields," ArXiv Astrophysics e-prints 0407286, 2004.

[22] SWORD. Vers. 3.2. Oak Ridge National Laboratories, Radiation Safety Information Computational Center, 2010. Computer software.

Appendix A: Landau Distribution

When a fast moving charged particle passes through a medium it deposits an amount of energy per unit length traversed according to the Bethe-Bloch equation. This process however is a statistical process. This means that even if two particles enter the medium with the exact same charged and energy, they will not necessarily deposit the same quantity of energy in the medium they traverse. As long as the initial energy of the particles is much larger than the energy they deposit in the medium and the distance travelled through the medium is short, the energy deposited will fit to some unknown distribution.

Let us denote our unknown distribution as $f(x,\Delta)$, where x is the thickness of our material through which the particles will travel, and Δ is the minimum energy deposited by the particle. When a particle enters the medium with an initial energy , it will deposit some energy in the range of $\Delta + d\Delta$. Next we shall define the probability of energy loss per unit length as $\omega(E,\varepsilon)$, where E is the energy of the particle at the time of the interaction and ε is a quantized energy loss. Because we have already stated the initial energy of the particle is much larger than the energy lost to the medium, we can approximate E with , which simplifies the probability of energy loss per unit length to $\omega(\varepsilon)$ because is constant. It is also important to note that the integral of our distribution over the energy deposited must be normalized ( ).

The differential change of the unknown distribution per unit length can be written as:

— (1)

We can use a Laplace transformation on this because x and Δ are both independent variables. For the transformation with respect to Δ we have:

(2)

This can then be inverted to obtain an equation for $f(x,\Delta)$ in terms of $\varphi(p,x)$:

(3)

Multiplying (1) by and integrating both sides gives us:

(4)

Imposing the surface boundary condition at $x = 0$ we must have $f(0,\Delta) = \delta(\Delta)$. This means there is a single particle of energy incident upon the detector $x = 0$. Plugging this into (2) gives us $p(\Delta) = 1$. Using these bounds to integrate (4) gives us:

(5)

Plugging (5) back into (3) now gives us the general solution for our unknown distribution.

(6)

While (6) may be the general solution to our distribution, it is not applicable without first defining the probability function $\omega(\varepsilon)$. In order to do this we must

place bounds on the energy ε. Let be a characteristic atomic energy, and be the maximum energy a fast moving charged particle can transfer to an electron during ionization. Using these we can say the only important values of p in (5) follow the criteria:

,

We will now define a new energy where From this we can make the approximation , which in turn gives us:

(7)

Applying the criteria an equation for $\omega(\varepsilon)$ can be obtained:

(8)

Where: - is Avogadro's Number

- e is the Electron charge
- ρ is the density of the medium
- is the sum of the atomic numbers of the molecules in the medium
- is the sum of the atomic weights of the molecules in the medium
- m is the electron mass
- v is the velocity of the particle

Substituting (8) into the first integral on the right side of (7) gives:

,

(9)

The new variable I is the ionization potential of the atoms in the medium. A generally accepted form of I is , with If we plug (8) into the second integral on the right side of (7) we get:

(10)

(10) can be simplified by substituting $z = p\varepsilon$ and remembering .

(11)

The sum of the last two terms on the right side of the equation is the well known value of –C, where C is Euler's constant (C = 0.577…). Simplifying (11) yields a much easier equation to work with.

(12)

Substituting (12) into (7) and (9) and simplifying now yields us:

(13)

A new quantity is introduced here to combine our constants and the co-ordinate x.

(14)

Combining (13) with our general equation (6) and simplifying yet again with a new term , we now obtain a workable integral form for our distribution.

(15)

(16)

Solving the integral in (16) in terms of λ now yields us the equation for a Landau distribution.

(17)

This derivation follows from Reference [4].

Appendix B: Computer Code to Save LeCroy Oscilloscope Data in Excel

```
Sub Button1_Click()

Dim NumMeasurements As Long

' Connect to the DSO
Set app = CreateObject("LeCroy.XStreamDSO")

‘The limit for the number of counts collected is taken from a value entered into the named cell
NumMeasurements = Cells(8, 5)

‘Set the coupling of the oscilloscope to 50 Ohms
app.Acquisition.C1.Coupling = "DC50"

‘Write data collected to excel sheet
Cells(1, 3).Value = app.Utility.DateTimeSetup.CurrentDateAndTime
'For j = 1 To 5
   For i = 1 To NumMeasurements - 1 Step 1
      'Cells(i, 1).Value = app.Measure.P4.Out.Result.Value
      'Cells(i, 7).Value = app.Measure.P5.Out.Result.Value
      Cells(i, 2).Value = app.Measure.P2.Out.Result.Value
      Cells(9, 5).Value = i
      If Cells(i, 2).Value <> Cells(i + 1, 2).Value Then
         Do While Cells(i, 2).Value = app.Measure.P2.Out.Result.Value
            Cells(i + 1, 2).Value = app.Measure.P2.Out.Result.Value
         Loop
      Else
         'Cells(i + 1, 1).Value = app.Measure.P4.Out.Result.Value
         'Cells(i + 1, 7).Value = app.Measure.P5.Out.Result.Value
         Cells(i + 1, 2).Value = app.Measure.P2.Out.Result.Value
      End If
   Next i
'Next j
Cells(2, 3).Value = app.Utility.DateTimeSetup.CurrentDateAndTime

Set app = Nothing
End Sub
```

Appendix C: Computer Code to Analyze Source Data in Root

```
void analysisup(TString dataFile = "foo", Float_t LFit, Float_t RFit) {

  //Set up file stream and open data file

  TString dataFilePath = gSystem-
>UnixPathName(TCint::GetCurrentMacroName());
  dataFilePath.ReplaceAll("analysisup.C","");
  dataFilePath.ReplaceAll("/./","/");
  TString dataFiletxt = dataFile;
  dataFiletxt.Append(".txt");
  dataFilePath.Append(dataFiletxt) ;
  ifstream dataFileStream;
  dataFileStream.open(dataFilePath.Data());

  // Set Histogram name, bins and limits
  TH1F *histogram = new TH1F("Histogram",dataFile,500,0,10);

  Float_t x;

  do {
    dataFileStream >> x;
    histogram->Fill(x) ;
  } while(dataFileStream.good()) ;

  // Axis labels
  histogram->SetXTitle("Pulse Area (V*us)");
  histogram->SetYTitle("Counts");
  histogram->GetYaxis()->SetTitleOffset(1.15);


  // Set the limits of the fitting curve
  TF1 *myfit = new TF1("myfit","gaus(0)+expo(3)",LFit,RFit);

  //Set the fit line color and position for the data box to the top right corner
  myfit->SetLineColor(kBlue);
  gStyle->SetOptFit(1111);
  gStyle->SetStatX(1);
  gStyle->SetStatW(.15);
```

```
 gStyle->SetStatH(.15);

 // Starting Parameters for the fit (take a guess)
 myfit->SetParNames("Strength","Mean","Sigma","ExpCon","ExpSlope");
 myfit->SetParameters(100, 2.5, .4, 0, 0);

 // Fit the spectrum
 histogram->Fit("myfit","+R");

 //Prepare gaussian for display and take parameters from fit
 TF1 *fSignal = new TF1("fSignal", "gaus(0)",1,6);
 Double_t param[5];
 myfit->GetParameters(param);
 fSignal->SetParameters(&param[0]);

 //Draw histogram and save image
 TCanvas *c = new TCanvas;
 histogram->SetLineColor(kRed);
 histogram->Draw();
 fSignal->Draw("SAME");
 TImage *img = TImage::Create();
 img->FromPad(c);
 img->WriteImage(dataFile.Append(".png"));
 delete c;
 delete img;
 delete histogram;
 delete fSignal;
}
```

Appendix D: Computer Code to Analyze Cosmic Ray Muon Data in Root

```
void analysis(TString dataFile = "foo.txt") {

  // Set up the data file stream and open the data file
  TString dataFilePath = gSystem-
>UnixPathName(TCint::GetCurrentMacroName());
  dataFilePath.ReplaceAll("analysis.C","");
  dataFilePath.ReplaceAll("/./","/");
  dataFilePath.Append(dataFile) ;
  ifstream dataFileStream;
  dataFileStream.open(dataFilePath.Data());

  // Set Histogram name, bins and limits
  TH1F *histogram = new TH1F("Histogram","GEM9Con5Cosmic",500,0.0,10.0);

  Float_t x;

  do {
    dataFileStream >> x;
    histogram->Fill(x) ;
  } while(dataFileStream.good()) ;

  // Axis labels
  histogram->SetXTitle("Pulse Area (V*us)");
  histogram->SetYTitle("Counts");
  histogram->GetYaxis()->SetTitleOffset(1.15);


  // Set the limits of the fitting curve
  TF1 *myfit = new TF1("myfit","landau",0.4,2.4);

//Set the fit line color and position for the data box to the top right corner
  myfit->SetLineColor(kBlue);
```

```
  gStyle->SetOptFit(0111);
  gStyle->SetStatX(1);
  gStyle->SetStatW(.15);
  gStyle->SetStatH(.15);


// Fit the spectrum
  histogram->Fit("myfit","+R");

 //Draw histogram and save image
  histogram->SetLineColor(kRed);
  histogram->Draw();
  TImage *img = TImage::Create();
  img->FromPad(c1);
  img->WriteImage("GEM9Con5Cosmic.png");
  delete img;
  c1->Close();
}
```

Appendix E: Histograms Used to Make Gain Uniformity Maps

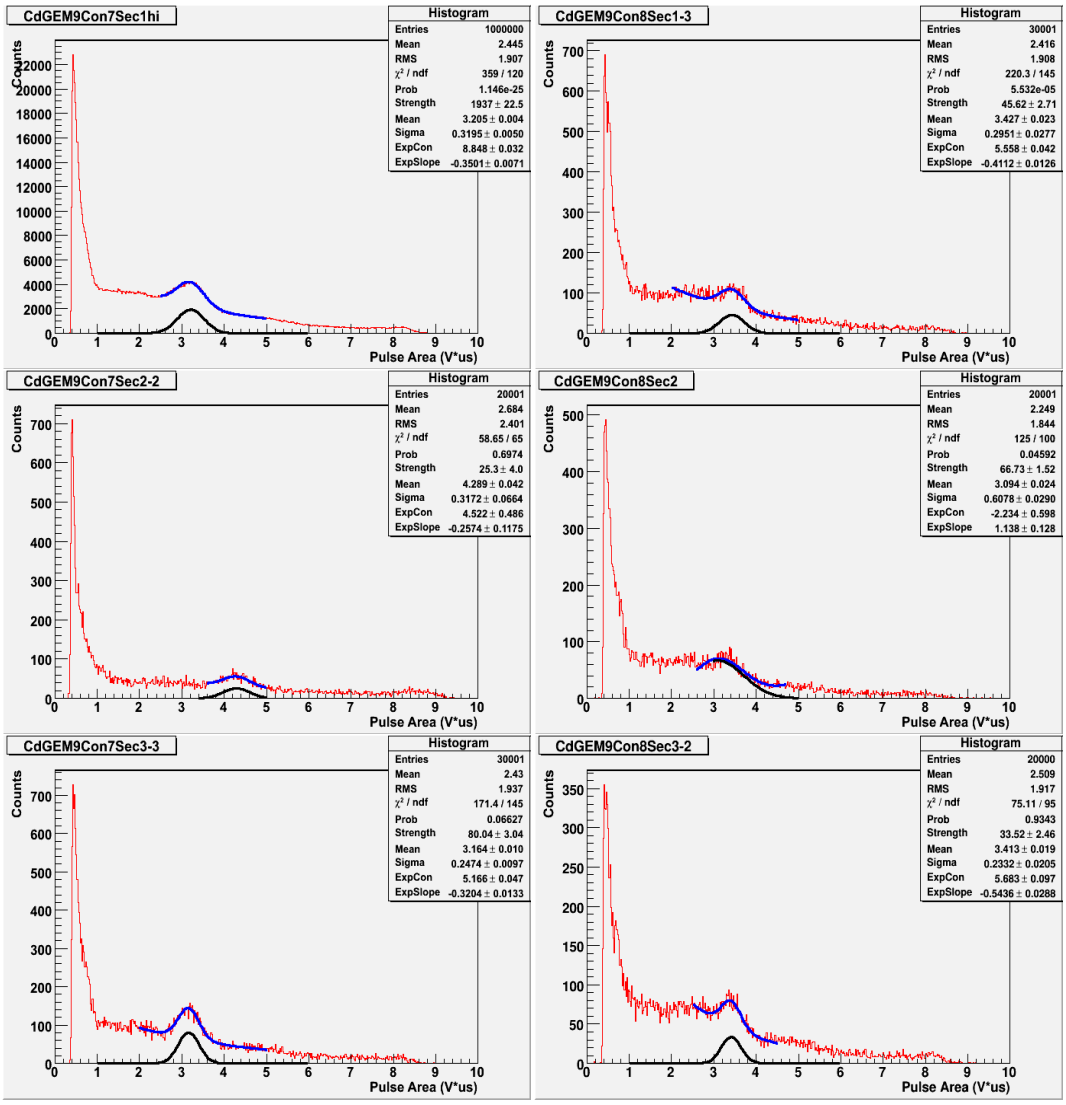

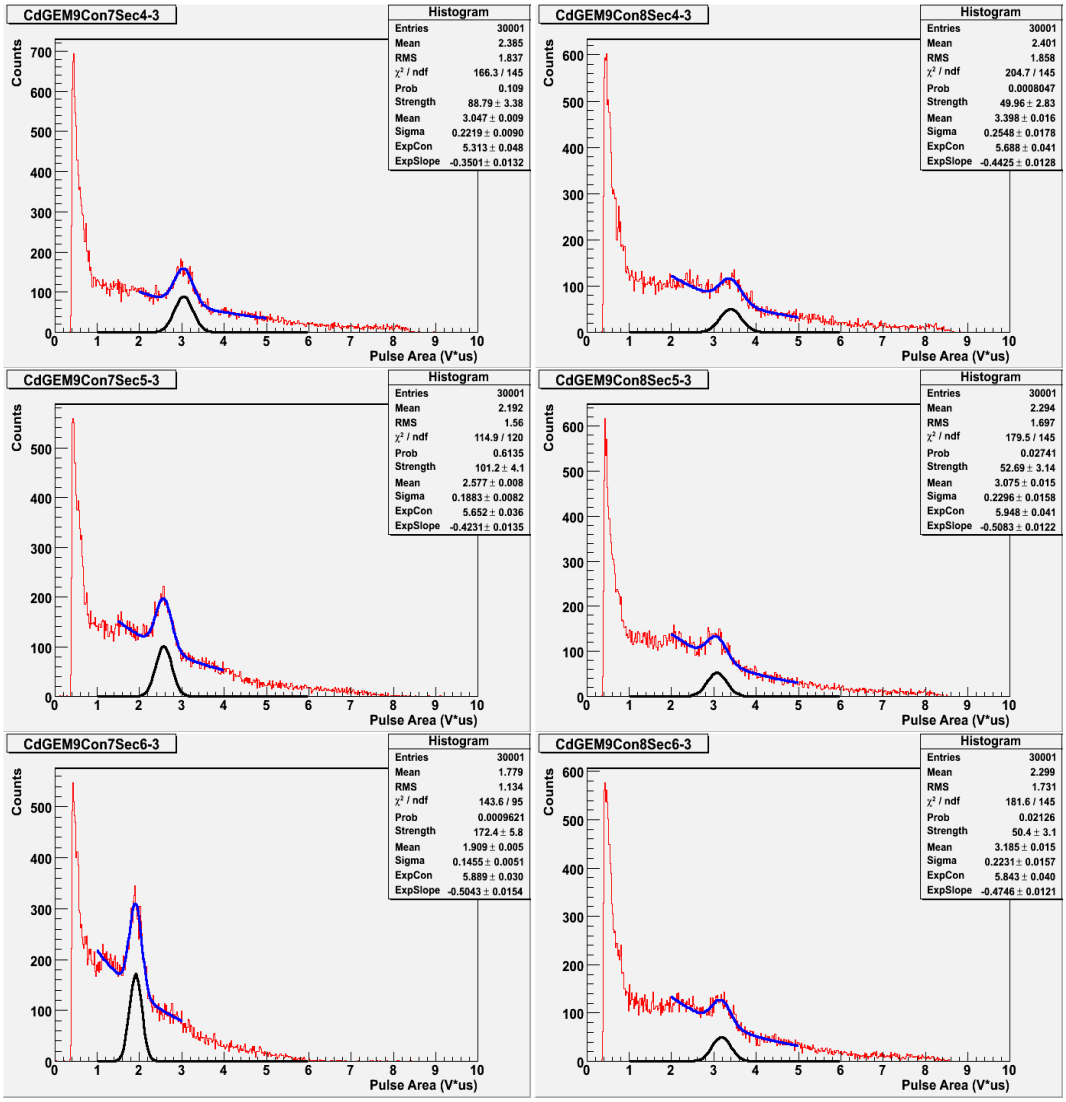

Histograms for the first and second columns of data used to make the normalized uniformity map for the Y readout of GEM 9 in figure 3.22.

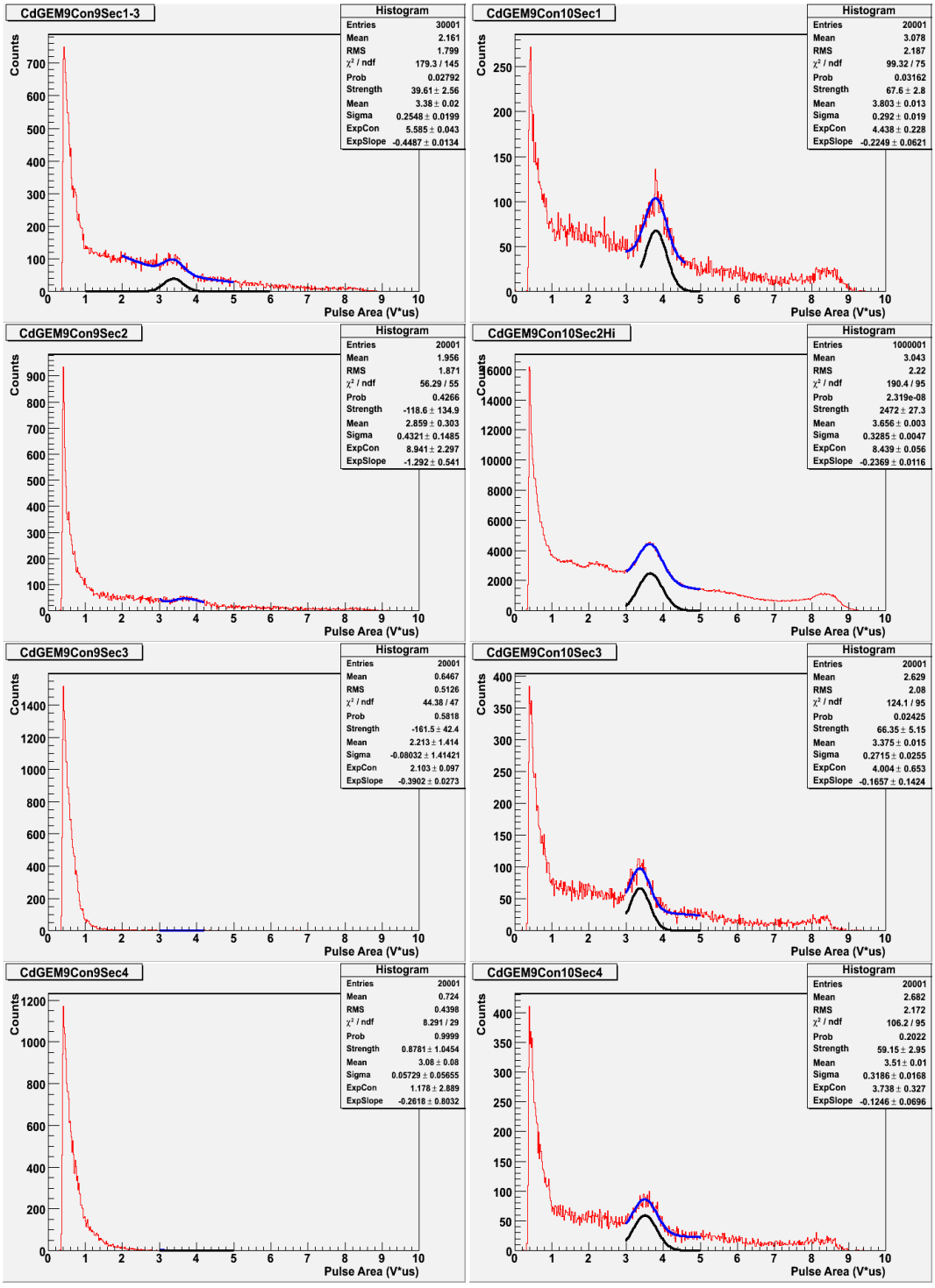
CdGEM9Con9Sec1-3
Histogram
Entries 30001
Mean 2.161
RMS 1.799
χ² / ndf 179.3 / 145
Prob 0.02792
Strength 39.61 ± 2.56
Mean 3.38 ± 0.02
Sigma 0.2548 ± 0.0199
ExpCon 5.585 ± 0.043
ExpSlope -0.4487 ± 0.0134
Counts
Pulse Area (V*us)
CdGEM9Con10Sec1
Histogram
Entries 20001
Mean 3.078
RMS 2.187
χ² / ndf 99.32 / 75
Prob 0.03162
Strength 67.6 ± 2.8
Mean 3.803 ± 0.013
Sigma 0.292 ± 0.019
ExpCon 4.438 ± 0.228
ExpSlope -0.2249 ± 0.0621
Counts
Pulse Area (V*us)
CdGEM9Con9Sec2
Histogram
Entries 20001
Mean 1.956
RMS 1.871
χ² / ndf 56.29 / 55
Prob 0.4266
Strength -118.6 ± 134.9
Mean 2.859 ± 0.303
Sigma 0.4321 ± 0.1485
ExpCon 8.941 ± 2.297
ExpSlope -1.292 ± 0.541
Counts
Pulse Area (V*us)
CdGEM9Con10Sec2Hi
Histogram
Entries 1000001
Mean 3.043
RMS 2.22
χ² / ndf 190.4 / 95
Prob 2.319e-08
Strength 2472 ± 27.3
Mean 3.656 ± 0.003
Sigma 0.3285 ± 0.0047
ExpCon 8.439 ± 0.056
ExpSlope -0.2369 ± 0.0116
Counts
Pulse Area (V*us)
CdGEM9Con9Sec3
Histogram
Entries 20001
Mean 0.6467
RMS 0.5126
χ² / ndf 44.38 / 47
Prob 0.5818
Strength -161.5 ± 42.4
Mean 2.213 ± 1.414
Sigma -0.08032 ± 1.41421
ExpCon 2.103 ± 0.097
ExpSlope -0.3902 ± 0.0273
Counts
Pulse Area (V*us)
CdGEM9Con10Sec3
Histogram
Entries 20001
Mean 2.629
RMS 2.08
χ² / ndf 124.1 / 95
Prob 0.02425
Strength 66.35 ± 5.15
Mean 3.375 ± 0.015
Sigma 0.2715 ± 0.0255
ExpCon 4.004 ± 0.653
ExpSlope -0.1657 ± 0.1424
Counts
Pulse Area (V*us)
CdGEM9Con9Sec4
Histogram
Entries 20001
Mean 0.724
RMS 0.4398
χ² / ndf 8.291 / 29
Prob 0.9999
Strength 0.8781 ± 1.0454
Mean 3.08 ± 0.08
Sigma 0.05729 ± 0.05655
ExpCon 1.178 ± 2.889
ExpSlope -0.2618 ± 0.8032
Counts
Pulse Area (V*us)
CdGEM9Con10Sec4
Histogram
Entries 20001
Mean 2.682
RMS 2.172
χ² / ndf 106.2 / 95
Prob 0.2022
Strength 59.15 ± 2.95
Mean 3.51 ± 0.01
Sigma 0.3186 ± 0.0168
ExpCon 3.738 ± 0.327
ExpSlope -0.1246 ± 0.0696
Counts
Pulse Area (V*us)

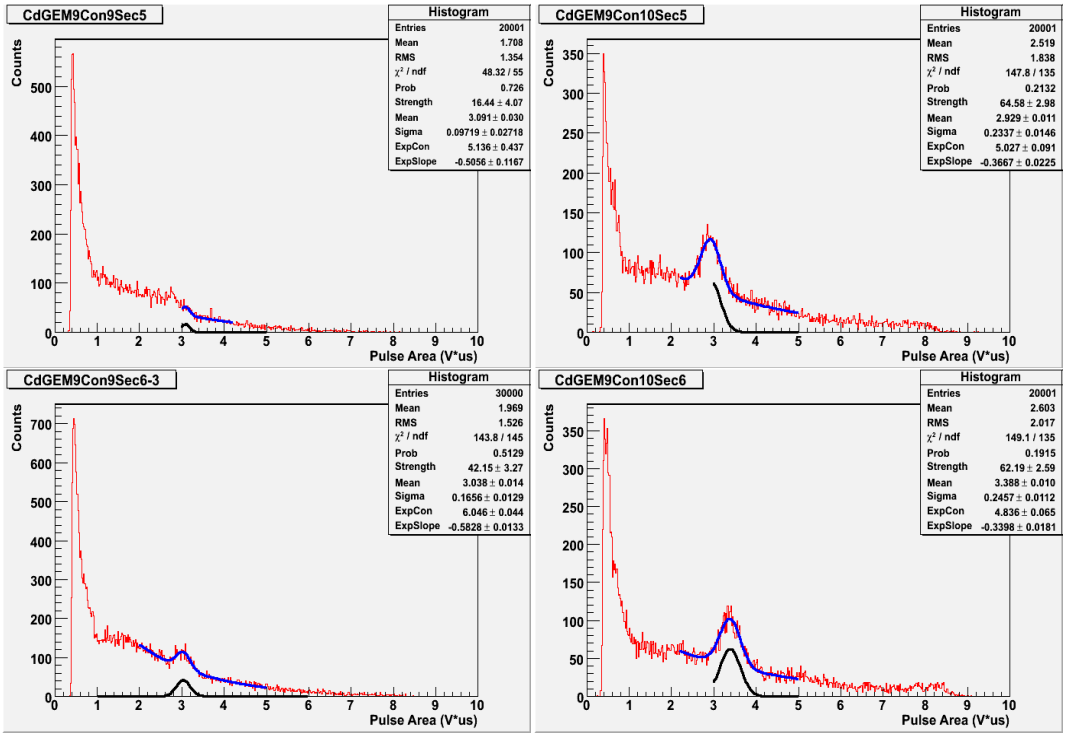

Histograms for the third and fourth columns of data used to make the normalized uniformity map for the Y readout of GEM 9 in figure 3.22.

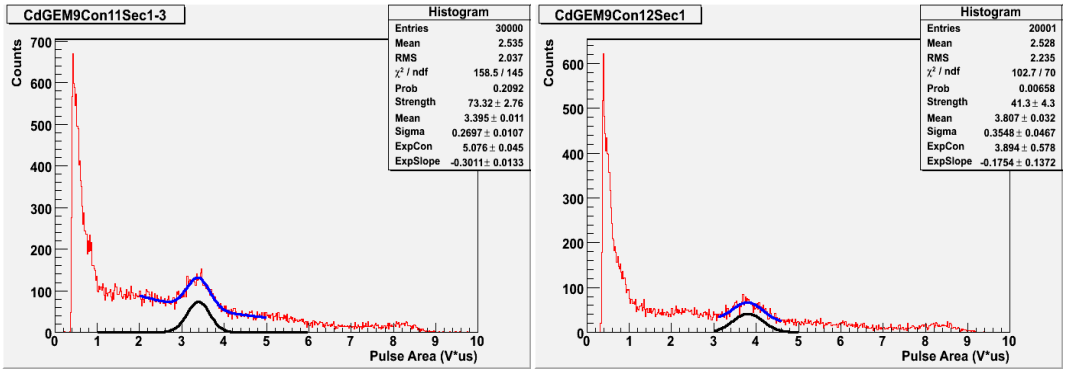

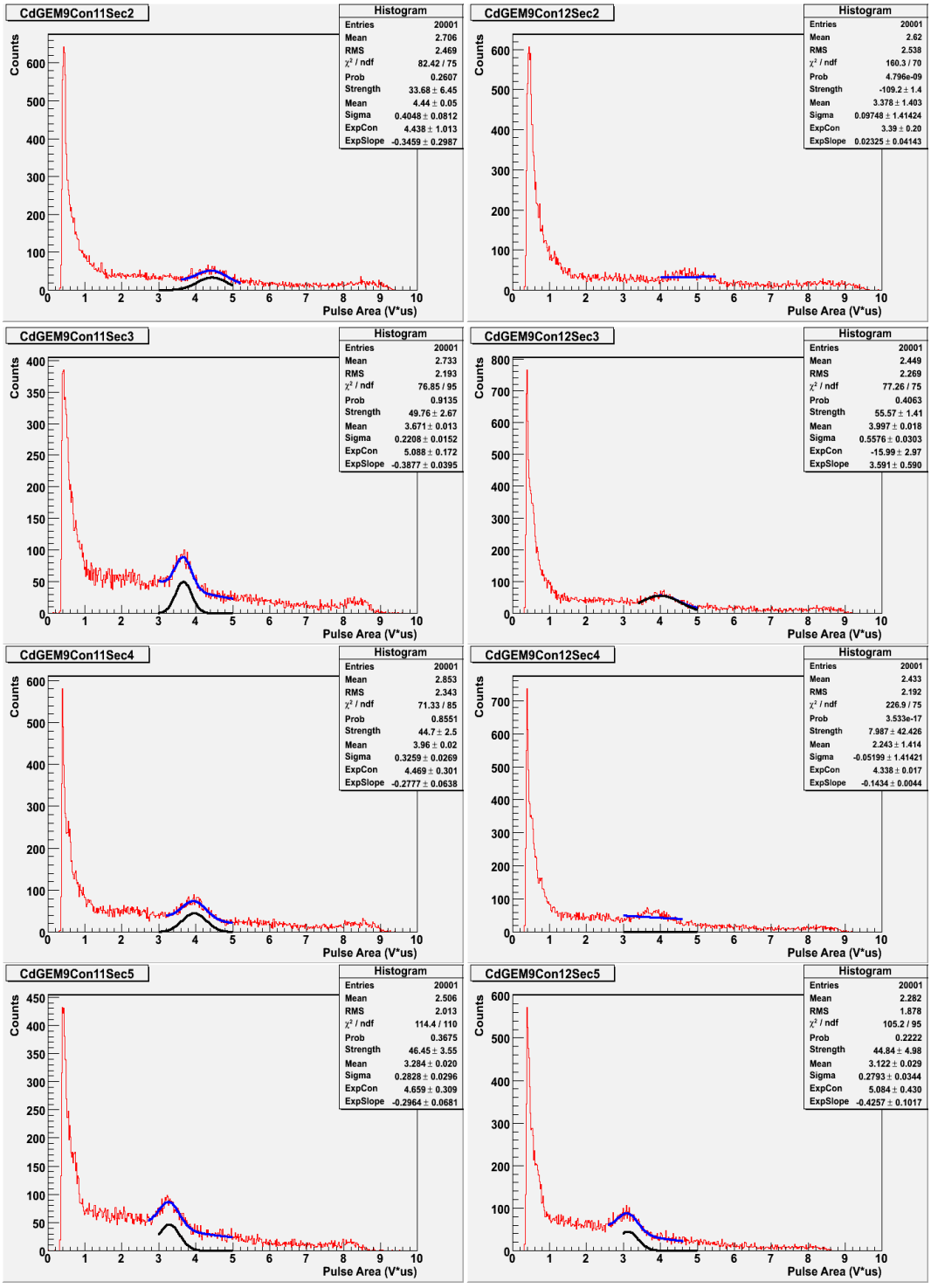
CdGEM9Con11Sec2
Histogram
Entries 20001
Mean 2.706
RMS 2.469
χ² / ndf 82.42 / 75
Prob 0.2607
Strength 33.68 ± 6.45
Mean 4.44 ± 0.05
Sigma 0.4048 ± 0.0812
ExpCon 4.438 ± 1.013
ExpSlope -0.3459 ± 0.2987
Counts
Pulse Area (V*us)
CdGEM9Con12Sec2
Histogram
Entries 20001
Mean 2.62
RMS 2.538
χ² / ndf 160.3 / 70
Prob 4.796e-09
Strength -109.2 ± 1.4
Mean 3.378 ± 1.403
Sigma 0.09748 ± 1.41424
ExpCon 3.39 ± 0.20
ExpSlope 0.02325 ± 0.04143
Counts
Pulse Area (V*us)
CdGEM9Con11Sec3
Histogram
Entries 20001
Mean 2.733
RMS 2.193
χ² / ndf 76.85 / 95
Prob 0.9135
Strength 49.76 ± 2.67
Mean 3.671 ± 0.013
Sigma 0.2208 ± 0.0152
ExpCon 5.088 ± 0.172
ExpSlope -0.3877 ± 0.0395
Counts
Pulse Area (V*us)
CdGEM9Con12Sec3
Histogram
Entries 20001
Mean 2.449
RMS 2.269
χ² / ndf 77.26 / 75
Prob 0.4063
Strength 55.57 ± 1.41
Mean 3.997 ± 0.018
Sigma 0.5576 ± 0.0303
ExpCon -15.99 ± 2.97
ExpSlope 3.591 ± 0.590
Counts
Pulse Area (V*us)
CdGEM9Con11Sec4
Histogram
Entries 20001
Mean 2.853
RMS 2.343
χ² / ndf 71.33 / 85
Prob 0.8551
Strength 44.7 ± 2.5
Mean 3.96 ± 0.02
Sigma 0.3259 ± 0.0269
ExpCon 4.469 ± 0.301
ExpSlope -0.2777 ± 0.0638
Counts
Pulse Area (V*us)
CdGEM9Con12Sec4
Histogram
Entries 20001
Mean 2.433
RMS 2.192
χ² / ndf 226.9 / 75
Prob 3.533e-17
Strength 7.987 ± 42.426
Mean 2.243 ± 1.414
Sigma -0.05199 ± 1.41421
ExpCon 4.338 ± 0.017
ExpSlope -0.1434 ± 0.0044
Counts
Pulse Area (V*us)
CdGEM9Con11Sec5
Histogram
Entries 20001
Mean 2.506
RMS 2.013
χ² / ndf 114.4 / 110
Prob 0.3675
Strength 46.45 ± 3.55
Mean 3.284 ± 0.020
Sigma 0.2828 ± 0.0296
ExpCon 4.659 ± 0.309
ExpSlope -0.2964 ± 0.0681
Counts
Pulse Area (V*us)
CdGEM9Con12Sec5
Histogram
Entries 20001
Mean 2.282
RMS 1.878
χ² / ndf 105.2 / 95
Prob 0.2222
Strength 44.84 ± 4.98
Mean 3.122 ± 0.029
Sigma 0.2793 ± 0.0344
ExpCon 5.084 ± 0.430
ExpSlope -0.4257 ± 0.1017
Counts
Pulse Area (V*us)

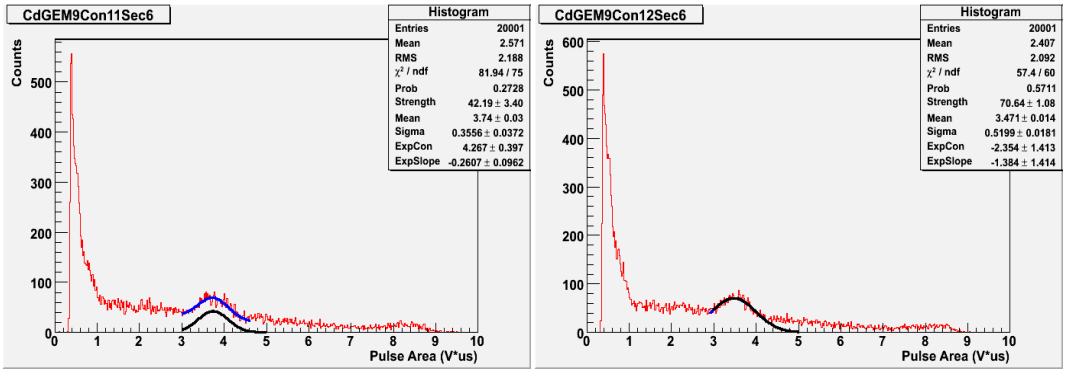

Histograms for the fifth and sixth columns of data used to make the normalized uniformity map for the Y readout of GEM 9 in figure 3.22.

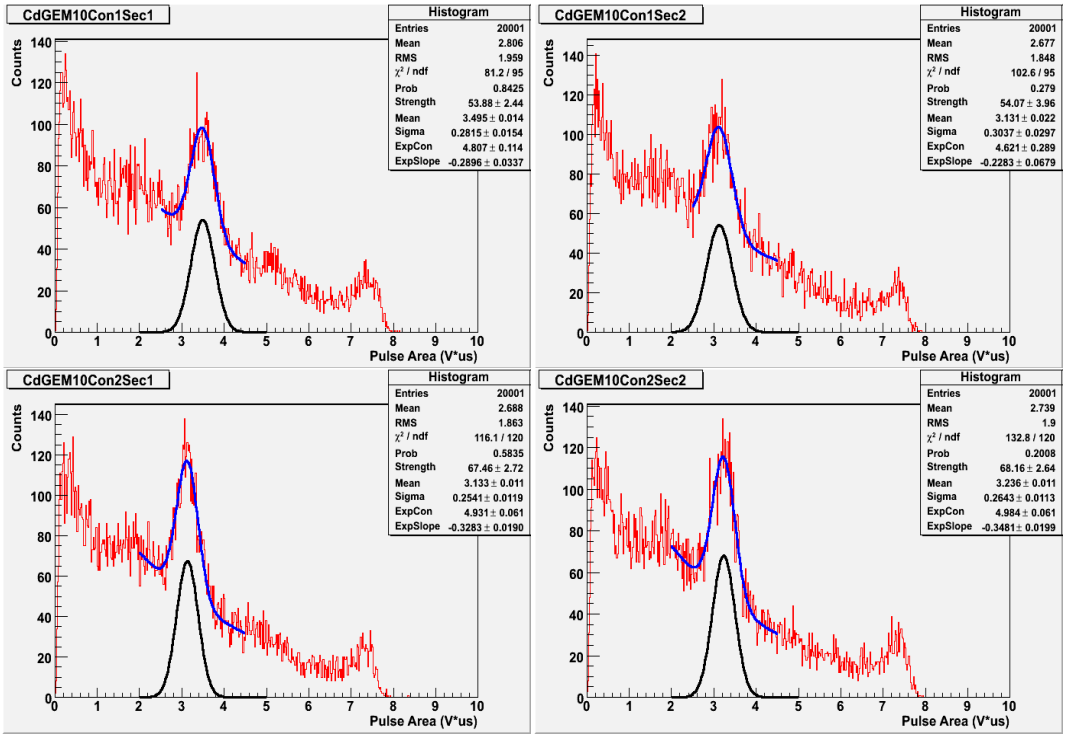

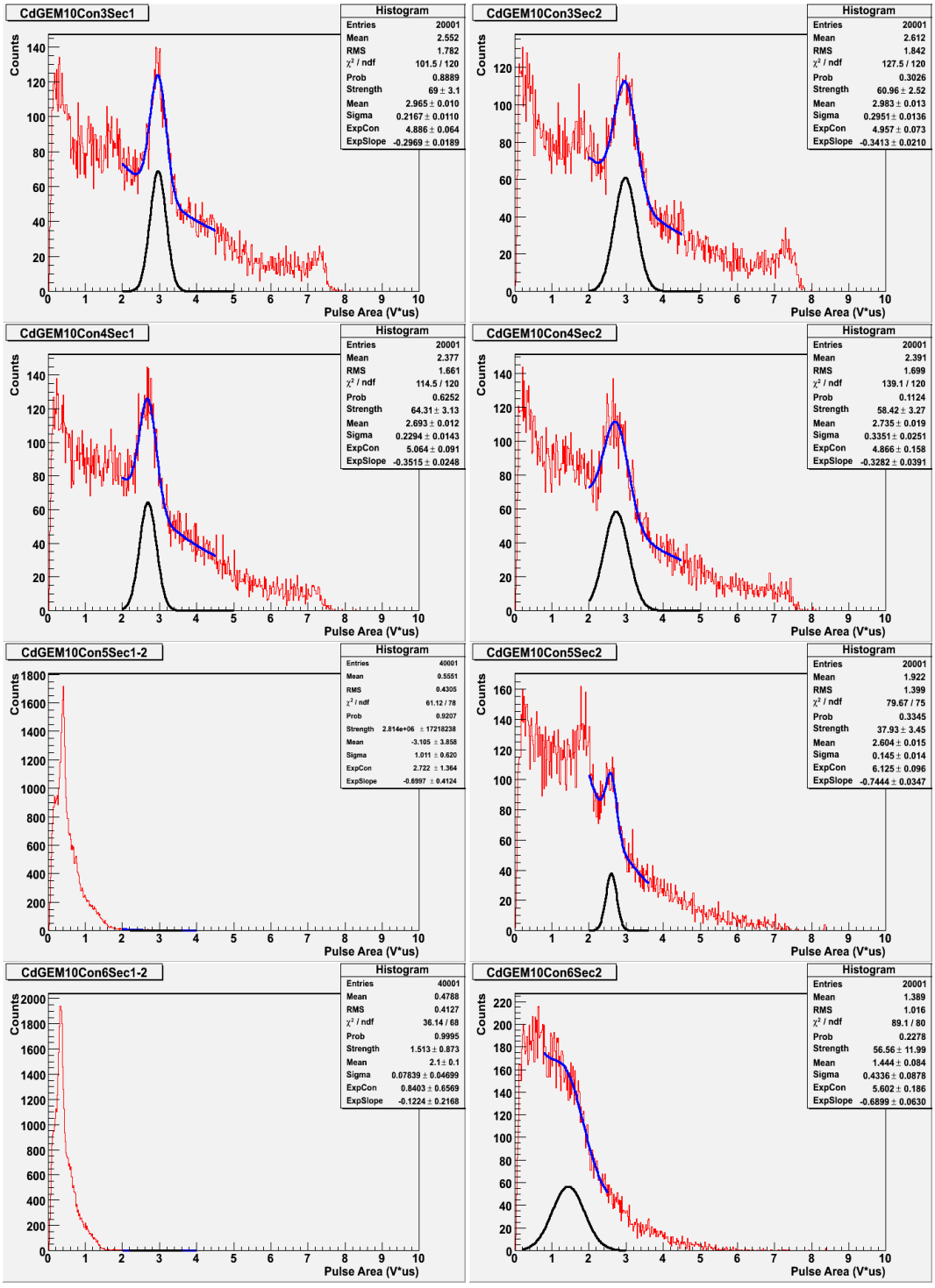

Histograms for the first and second columns of data used to make the normalized uniformity map for the X readout of GEM 10 in figure 3.24.

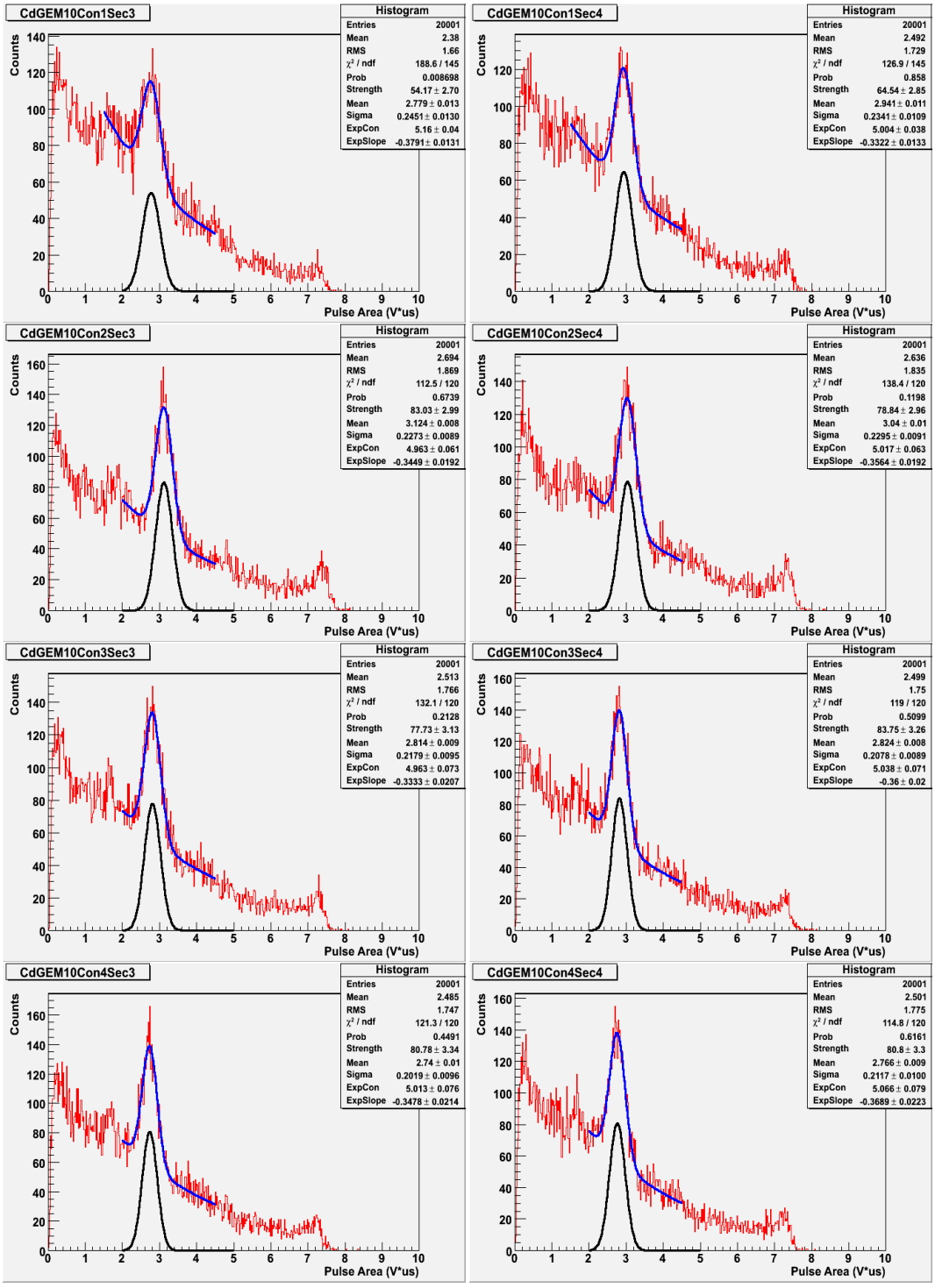
CdGEM10Con1Sec3
Histogram
Entries 20001
Mean 2.38
RMS 1.66
χ² / ndf 188.6 / 145
Prob 0.008698
Strength 54.17 ± 2.70
Mean 2.779 ± 0.013
Sigma 0.2451 ± 0.0130
ExpCon 5.16 ± 0.04
ExpSlope -0.3791 ± 0.0131
CdGEM10Con1Sec4
Histogram
Entries 20001
Mean 2.492
RMS 1.729
χ² / ndf 126.9 / 145
Prob 0.858
Strength 64.54 ± 2.85
Mean 2.941 ± 0.011
Sigma 0.2341 ± 0.0109
ExpCon 5.004 ± 0.038
ExpSlope -0.3322 ± 0.0133
CdGEM10Con2Sec3
Histogram
Entries 20001
Mean 2.694
RMS 1.869
χ² / ndf 112.5 / 120
Prob 0.6739
Strength 83.03 ± 2.99
Mean 3.124 ± 0.008
Sigma 0.2273 ± 0.0089
ExpCon 4.963 ± 0.061
ExpSlope -0.3449 ± 0.0192
CdGEM10Con2Sec4
Histogram
Entries 20001
Mean 2.636
RMS 1.835
χ² / ndf 138.4 / 120
Prob 0.1198
Strength 78.84 ± 2.96
Mean 3.04 ± 0.01
Sigma 0.2295 ± 0.0091
ExpCon 5.017 ± 0.063
ExpSlope -0.3564 ± 0.0192
CdGEM10Con3Sec3
Histogram
Entries 20001
Mean 2.513
RMS 1.766
χ² / ndf 132.1 / 120
Prob 0.2128
Strength 77.73 ± 3.13
Mean 2.814 ± 0.009
Sigma 0.2179 ± 0.0095
ExpCon 4.963 ± 0.073
ExpSlope -0.3333 ± 0.0207
CdGEM10Con3Sec4
Histogram
Entries 20001
Mean 2.499
RMS 1.75
χ² / ndf 119 / 120
Prob 0.5099
Strength 83.75 ± 3.26
Mean 2.824 ± 0.008
Sigma 0.2078 ± 0.0089
ExpCon 5.038 ± 0.071
ExpSlope -0.36 ± 0.02
CdGEM10Con4Sec3
Histogram
Entries 20001
Mean 2.485
RMS 1.747
χ² / ndf 121.3 / 120
Prob 0.4491
Strength 80.78 ± 3.34
Mean 2.74 ± 0.01
Sigma 0.2019 ± 0.0096
ExpCon 5.013 ± 0.076
ExpSlope -0.3478 ± 0.0214
CdGEM10Con4Sec4
Histogram
Entries 20001
Mean 2.501
RMS 1.775
χ² / ndf 114.8 / 120
Prob 0.6161
Strength 80.8 ± 3.3
Mean 2.766 ± 0.009
Sigma 0.2117 ± 0.0100
ExpCon 5.066 ± 0.079
ExpSlope -0.3689 ± 0.0223
Counts
Pulse Area (V*us)

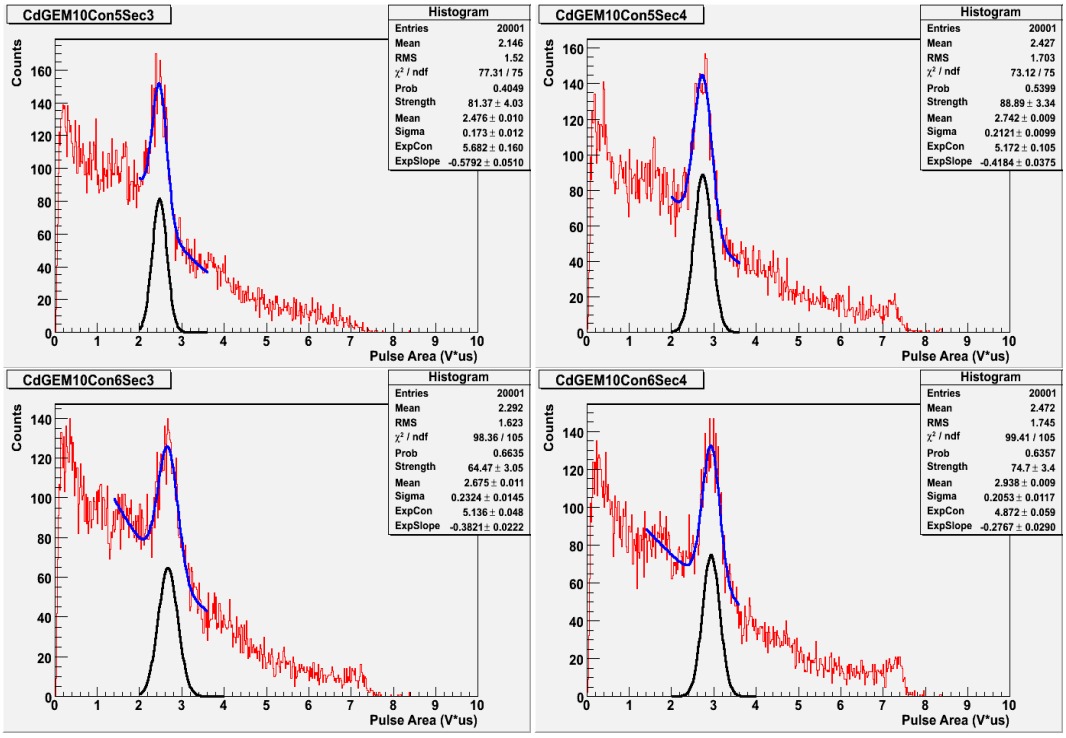

Histograms for the third and fourth columns of data used to make the normalized uniformity map for the X readout of GEM 10 in figure 3.24.

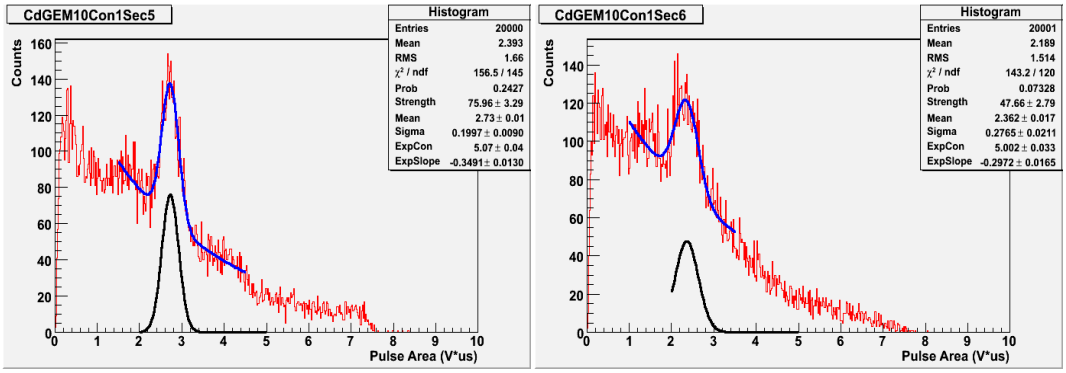

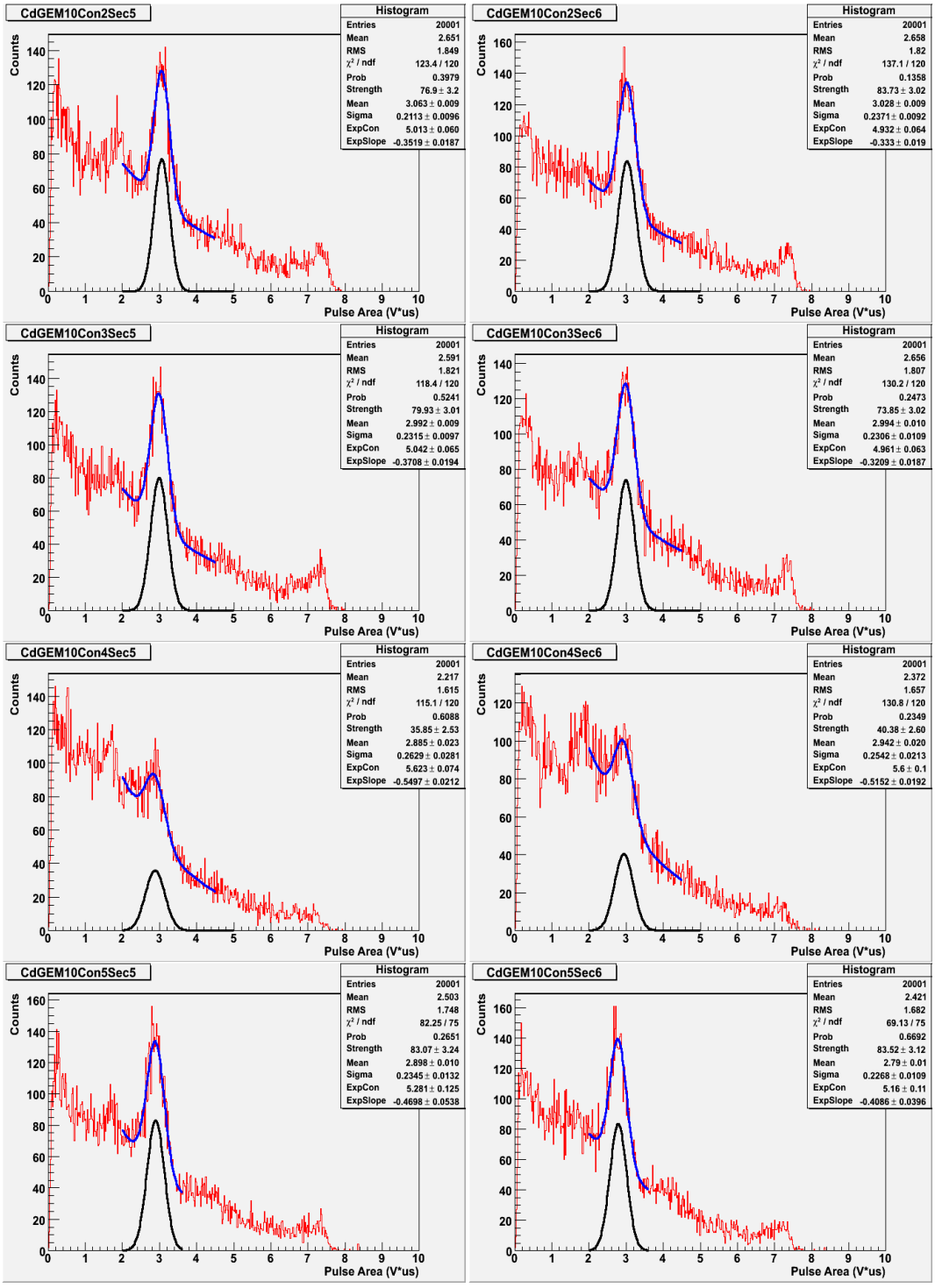
CdGEM10Con2Sec5
Histogram
Entries 20001
Mean 2.651
RMS 1.849
χ² / ndf 123.4 / 120
Prob 0.3979
Strength 76.9 ± 3.2
Mean 3.063 ± 0.009
Sigma 0.2113 ± 0.0096
ExpCon 5.013 ± 0.060
ExpSlope -0.3519 ± 0.0187
Counts
Pulse Area (V*us)
CdGEM10Con2Sec6
Histogram
Entries 20001
Mean 2.658
RMS 1.82
χ² / ndf 137.1 / 120
Prob 0.1358
Strength 83.73 ± 3.02
Mean 3.028 ± 0.009
Sigma 0.2371 ± 0.0092
ExpCon 4.932 ± 0.064
ExpSlope -0.333 ± 0.019
Counts
Pulse Area (V*us)
CdGEM10Con3Sec5
Histogram
Entries 20001
Mean 2.591
RMS 1.821
χ² / ndf 118.4 / 120
Prob 0.5241
Strength 79.93 ± 3.01
Mean 2.992 ± 0.009
Sigma 0.2315 ± 0.0097
ExpCon 5.042 ± 0.065
ExpSlope -0.3708 ± 0.0194
Counts
Pulse Area (V*us)
CdGEM10Con3Sec6
Histogram
Entries 20001
Mean 2.656
RMS 1.807
χ² / ndf 130.2 / 120
Prob 0.2473
Strength 73.85 ± 3.02
Mean 2.994 ± 0.010
Sigma 0.2306 ± 0.0109
ExpCon 4.961 ± 0.063
ExpSlope -0.3209 ± 0.0187
Counts
Pulse Area (V*us)
CdGEM10Con4Sec5
Histogram
Entries 20001
Mean 2.217
RMS 1.615
χ² / ndf 115.1 / 120
Prob 0.6088
Strength 35.85 ± 2.53
Mean 2.885 ± 0.023
Sigma 0.2629 ± 0.0281
ExpCon 5.623 ± 0.074
ExpSlope -0.5497 ± 0.0212
Counts
Pulse Area (V*us)
CdGEM10Con4Sec6
Histogram
Entries 20001
Mean 2.372
RMS 1.657
χ² / ndf 130.8 / 120
Prob 0.2349
Strength 40.38 ± 2.60
Mean 2.942 ± 0.020
Sigma 0.2542 ± 0.0213
ExpCon 5.6 ± 0.1
ExpSlope -0.5152 ± 0.0192
Counts
Pulse Area (V*us)
CdGEM10Con5Sec5
Histogram
Entries 20001
Mean 2.503
RMS 1.748
χ² / ndf 82.25 / 75
Prob 0.2651
Strength 83.07 ± 3.24
Mean 2.898 ± 0.010
Sigma 0.2345 ± 0.0132
ExpCon 5.281 ± 0.125
ExpSlope -0.4698 ± 0.0538
Counts
Pulse Area (V*us)
CdGEM10Con5Sec6
Histogram
Entries 20001
Mean 2.421
RMS 1.682
χ² / ndf 69.13 / 75
Prob 0.6692
Strength 83.52 ± 3.12
Mean 2.79 ± 0.01
Sigma 0.2268 ± 0.0109
ExpCon 5.16 ± 0.11
ExpSlope -0.4086 ± 0.0396
Counts
Pulse Area (V*us)

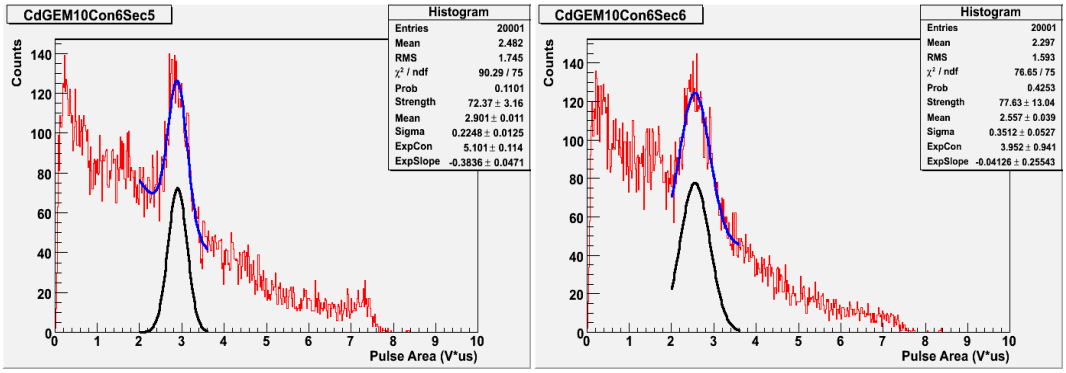

Histograms for the fifth and sixth columns of data used to make the normalized uniformity map for the X readout of GEM 10 in figure 3.24.

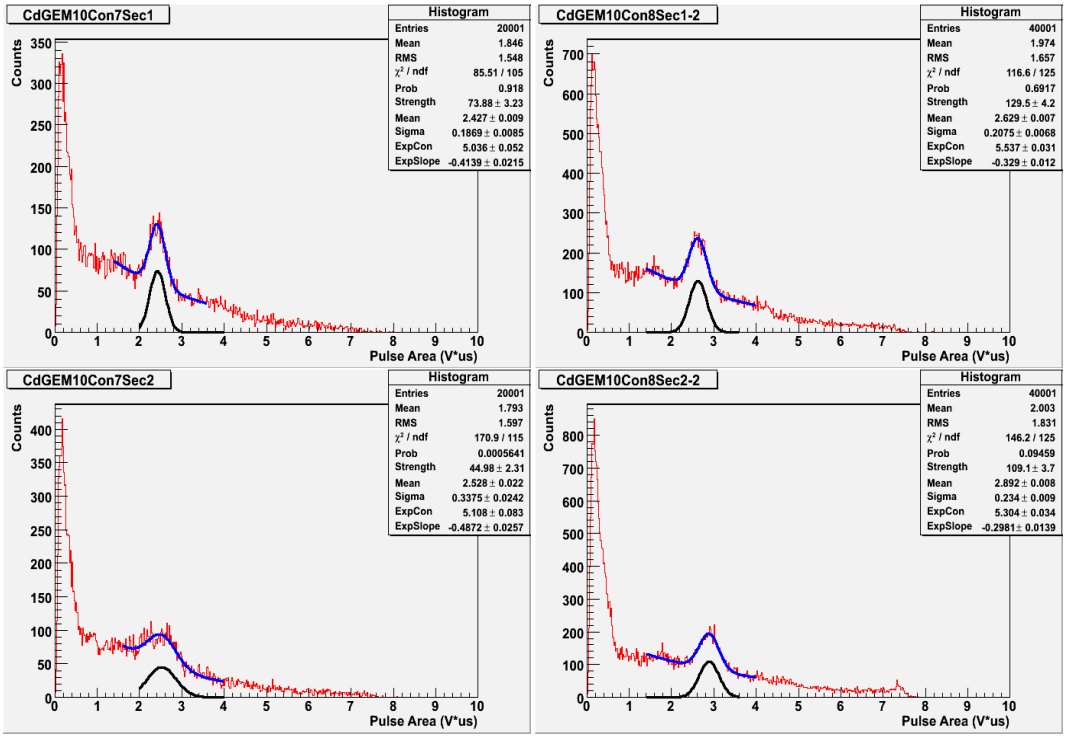

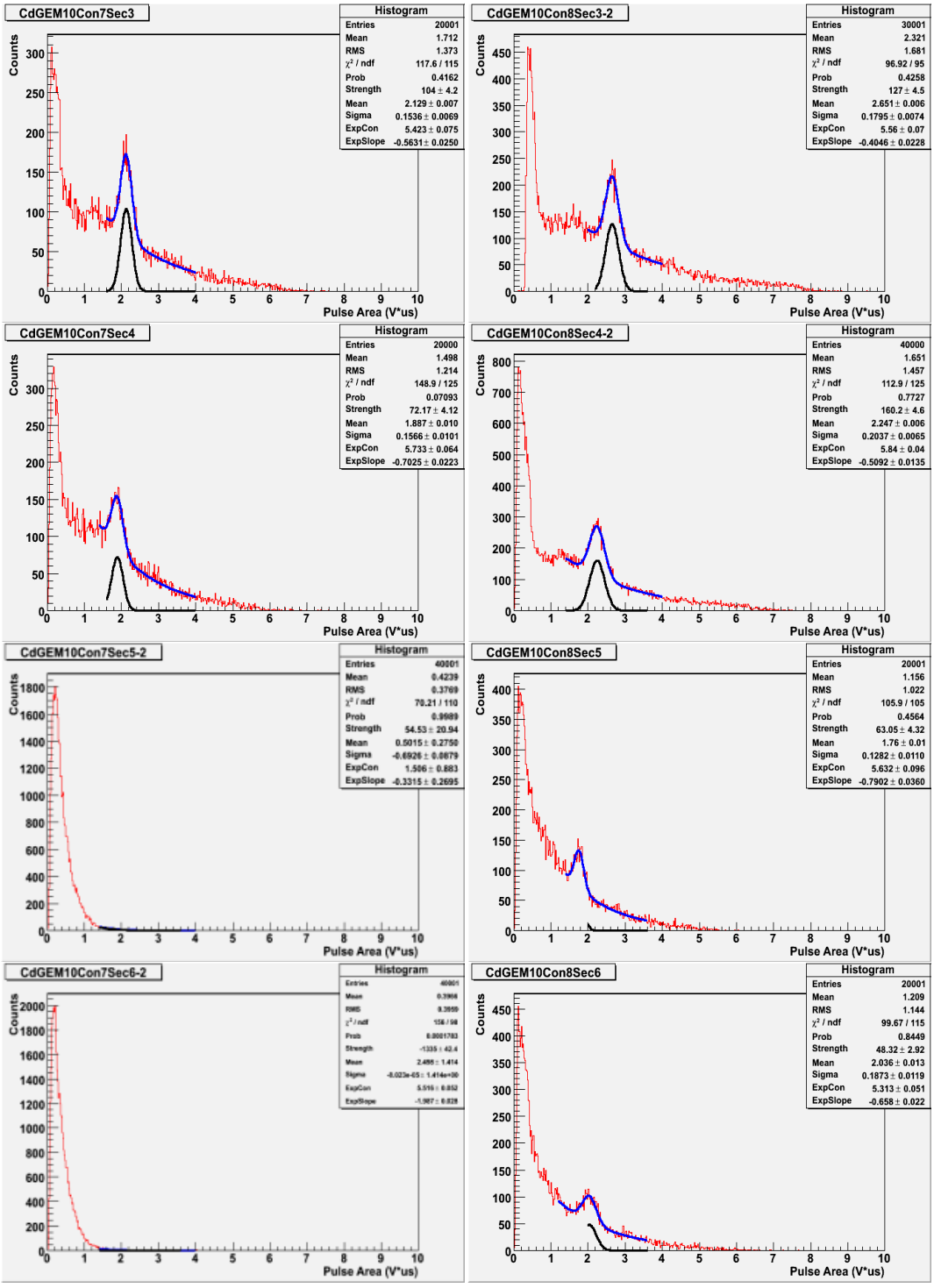

Histograms for the first and second columns of data used to make the normalized uniformity map for the Y readout of GEM10 in figure 3.25.

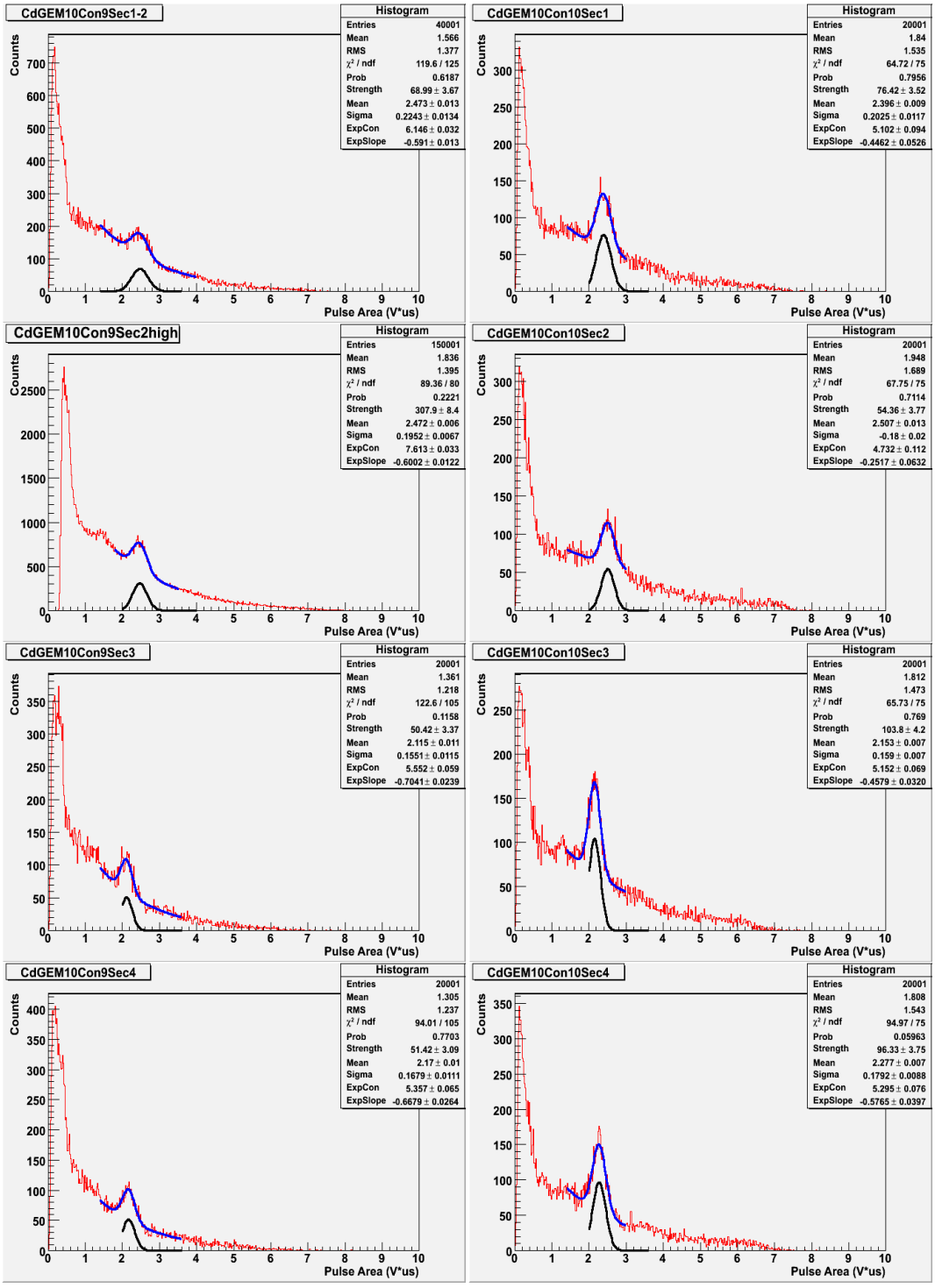
CdGEM10Con9Sec1-2
Histogram
Entries 40001
Mean 1.566
RMS 1.377
χ² / ndf 119.6 / 125
Prob 0.6187
Strength 68.99 ± 3.67
Mean 2.473 ± 0.013
Sigma 0.2243 ± 0.0134
ExpCon 6.146 ± 0.032
ExpSlope -0.591 ± 0.013
Counts
Pulse Area (V*us)
CdGEM10Con10Sec1
Histogram
Entries 20001
Mean 1.84
RMS 1.535
χ² / ndf 64.72 / 75
Prob 0.7956
Strength 76.42 ± 3.52
Mean 2.396 ± 0.009
Sigma 0.2025 ± 0.0117
ExpCon 5.102 ± 0.094
ExpSlope -0.4462 ± 0.0526
Counts
Pulse Area (V*us)
CdGEM10Con9Sec2high
Histogram
Entries 150001
Mean 1.836
RMS 1.395
χ² / ndf 89.36 / 80
Prob 0.2221
Strength 307.9 ± 8.4
Mean 2.472 ± 0.006
Sigma 0.1952 ± 0.0067
ExpCon 7.613 ± 0.033
ExpSlope -0.6002 ± 0.0122
Counts
Pulse Area (V*us)
CdGEM10Con10Sec2
Histogram
Entries 20001
Mean 1.948
RMS 1.689
χ² / ndf 67.75 / 75
Prob 0.7114
Strength 54.36 ± 3.77
Mean 2.507 ± 0.013
Sigma -0.18 ± 0.02
ExpCon 4.732 ± 0.112
ExpSlope -0.2517 ± 0.0632
Counts
Pulse Area (V*us)
CdGEM10Con9Sec3
Histogram
Entries 20001
Mean 1.361
RMS 1.218
χ² / ndf 122.6 / 105
Prob 0.1158
Strength 50.42 ± 3.37
Mean 2.115 ± 0.011
Sigma 0.1551 ± 0.0115
ExpCon 5.552 ± 0.059
ExpSlope -0.7041 ± 0.0239
Counts
Pulse Area (V*us)
CdGEM10Con10Sec3
Histogram
Entries 20001
Mean 1.812
RMS 1.473
χ² / ndf 65.73 / 75
Prob 0.769
Strength 103.8 ± 4.2
Mean 2.153 ± 0.007
Sigma 0.159 ± 0.007
ExpCon 5.152 ± 0.069
ExpSlope -0.4579 ± 0.0320
Counts
Pulse Area (V*us)
CdGEM10Con9Sec4
Histogram
Entries 20001
Mean 1.305
RMS 1.237
χ² / ndf 94.01 / 105
Prob 0.7703
Strength 51.42 ± 3.09
Mean 2.17 ± 0.01
Sigma 0.1679 ± 0.0111
ExpCon 5.357 ± 0.065
ExpSlope -0.6679 ± 0.0264
Counts
Pulse Area (V*us)
CdGEM10Con10Sec4
Histogram
Entries 20001
Mean 1.808
RMS 1.543
χ² / ndf 94.97 / 75
Prob 0.05963
Strength 96.33 ± 3.75
Mean 2.277 ± 0.007
Sigma 0.1792 ± 0.0088
ExpCon 5.295 ± 0.076
ExpSlope -0.5765 ± 0.0397
Counts
Pulse Area (V*us)

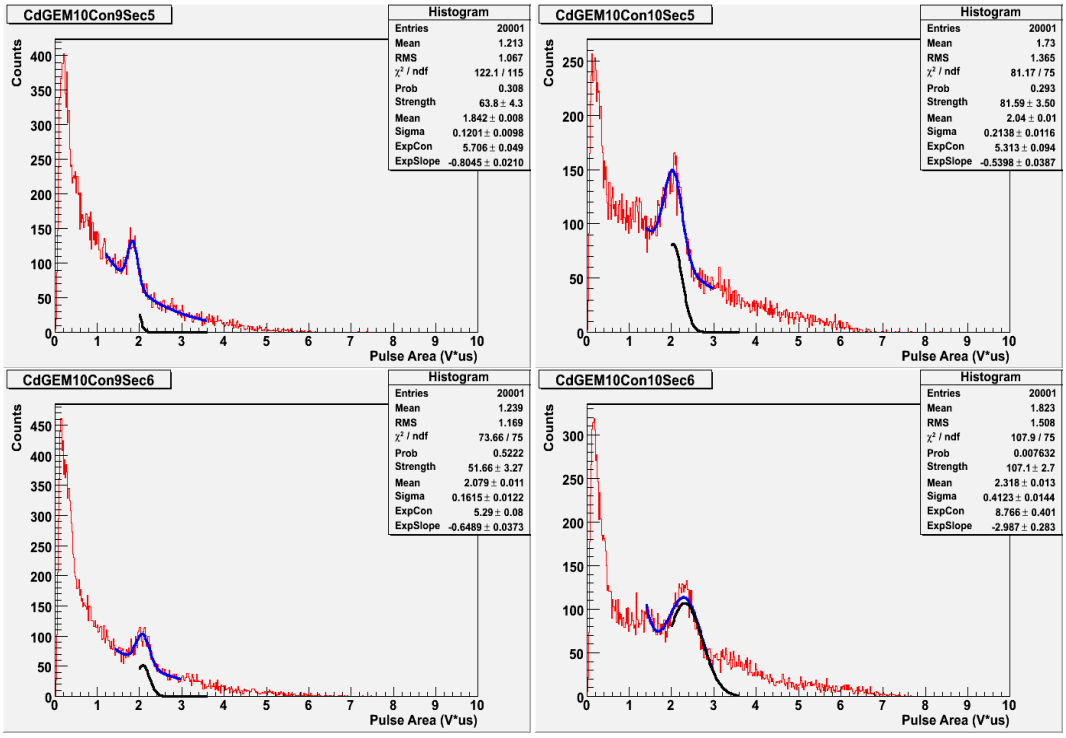

Histograms for the third and fourth columns of data used to make the normalized uniformity map for the Y readout of GEM10 in figure 3.25.

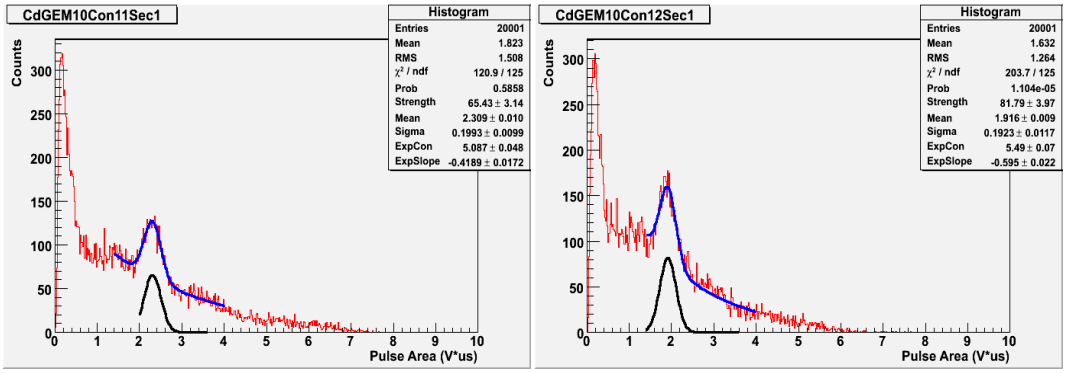

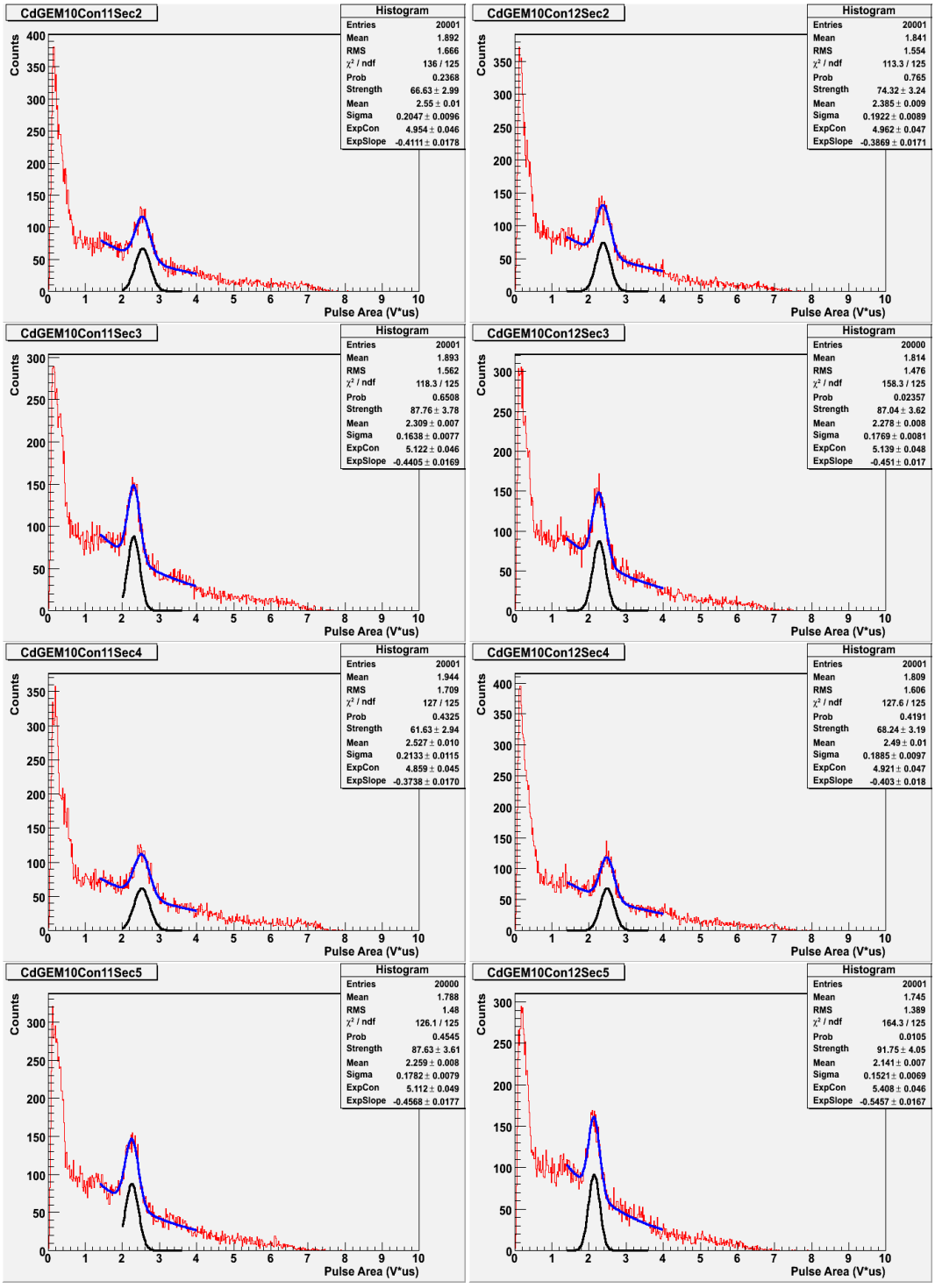
CdGEM10Con11Sec2
Histogram
Entries 20001
Mean 1.892
RMS 1.666
χ² / ndf 136 / 125
Prob 0.2368
Strength 66.63 ± 2.99
Mean 2.55 ± 0.01
Sigma 0.2047 ± 0.0096
ExpCon 4.954 ± 0.046
ExpSlope -0.4111 ± 0.0178
CdGEM10Con12Sec2
Histogram
Entries 20001
Mean 1.841
RMS 1.554
χ² / ndf 113.3 / 125
Prob 0.765
Strength 74.32 ± 3.24
Mean 2.385 ± 0.009
Sigma 0.1922 ± 0.0089
ExpCon 4.962 ± 0.047
ExpSlope -0.3869 ± 0.0171
CdGEM10Con11Sec3
Histogram
Entries 20001
Mean 1.893
RMS 1.562
χ² / ndf 118.3 / 125
Prob 0.6508
Strength 87.76 ± 3.78
Mean 2.309 ± 0.007
Sigma 0.1638 ± 0.0077
ExpCon 5.122 ± 0.046
ExpSlope -0.4405 ± 0.0169
CdGEM10Con12Sec3
Histogram
Entries 20000
Mean 1.814
RMS 1.476
χ² / ndf 158.3 / 125
Prob 0.02357
Strength 87.04 ± 3.62
Mean 2.278 ± 0.008
Sigma 0.1769 ± 0.0081
ExpCon 5.139 ± 0.048
ExpSlope -0.451 ± 0.017
CdGEM10Con11Sec4
Histogram
Entries 20001
Mean 1.944
RMS 1.709
χ² / ndf 127 / 125
Prob 0.4325
Strength 61.63 ± 2.94
Mean 2.527 ± 0.010
Sigma 0.2133 ± 0.0115
ExpCon 4.859 ± 0.045
ExpSlope -0.3738 ± 0.0170
CdGEM10Con12Sec4
Histogram
Entries 20001
Mean 1.809
RMS 1.606
χ² / ndf 127.6 / 125
Prob 0.4191
Strength 68.24 ± 3.19
Mean 2.49 ± 0.01
Sigma 0.1885 ± 0.0097
ExpCon 4.921 ± 0.047
ExpSlope -0.403 ± 0.018
CdGEM10Con11Sec5
Histogram
Entries 20000
Mean 1.788
RMS 1.48
χ² / ndf 126.1 / 125
Prob 0.4545
Strength 87.63 ± 3.61
Mean 2.259 ± 0.008
Sigma 0.1782 ± 0.0079
ExpCon 5.112 ± 0.049
ExpSlope -0.4568 ± 0.0177
CdGEM10Con12Sec5
Histogram
Entries 20001
Mean 1.745
RMS 1.389
χ² / ndf 164.3 / 125
Prob 0.0105
Strength 91.75 ± 4.05
Mean 2.141 ± 0.007
Sigma 0.1521 ± 0.0069
ExpCon 5.408 ± 0.046
ExpSlope -0.5457 ± 0.0167
Counts
Pulse Area (V*us)

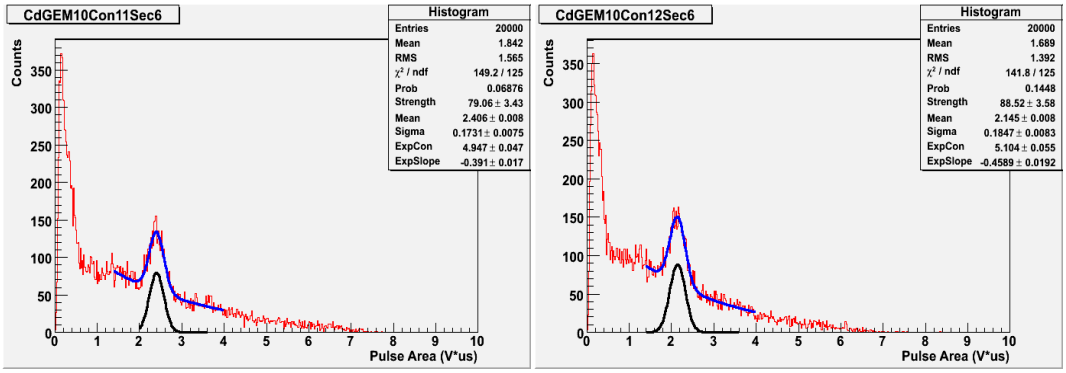

Histograms for the fifth and sixth columns of data used to make the normalized uniformity map for the Y readout of GEM10 in figure 3.25.